Sensors for mechanical stress based on inverse magnetostrictive CoFeB/MgO/CoFeB tunnel junctions

Niklas Dohmeier
Department of Physics
University of Bielefeld

This dissertation is submitted for the degree of
Doctor rerum naturalium

2019

- Ralph Ruthe, Bielefelder Witzbildzeichner

Acknowledgements

Mein wichtigster Dank gilt meinem Doktorvater Prof. Dr. Günter Reiss. Dafür, dass ich meine Dissertation in seiner Arbeitsgruppe erarbeiten durfte, aber auch für seine fachliche, als auch menschliche Unterstützung während meiner Promotion. Ein großer Dank gilt Dr. Karsten Rott. Sowohl für seine fachliche Unterstützung zum Thema TMR Stacks, bei der Unterstützung der Lithographie und dafür, dass dank ihm unsere Anlagen zuverlässig waren.

Unseren Kooperationspartnern der Christian-Albrechts-Universität zu Kiel, expliziet Dr. Ali Tavassolizadeh und Dr. Dirk Meyners gilt mein Dank für die vielen fruchtbaren fachlichen Gespräche und spannenden Einblicke vor Ort in die Weiterverarbeitung der TMR Sensoren.

Ich danke ebenfalls Dr. Christian Lang. Wir haben die meiste Zeit unseren Diplomstudiums zusammen gearbeitet, in der Promotion und danch auch den Kontakt nicht verloren, worüber ich sehr froh bin.

Auch meinen Kollegen von D2 gilt großer Dank für die immer freundschaftliche Zusammenarbeit. Die Arbeitsgruppe von D2 zeichnet sich durch eine hohe Hilfsbereitschaft und Kollegialität aus. Im Besonderen sind hier zu nennen: Dr. Lars Helmich, Timo Oberbiermann, Luca Marnitz, Andreas Becker, Philipp Zilske, Marianne Dunz, Dr. Martin Gottschalk, Dr Jungwo Koo und Dr. Christian Sterwerf.

Für einen reibungslosen Ablauf in allen verwaltungstechnischen und organisatorischen Bereichen haben Frau Aggi Windmann und Frau Elke Siedlaczek gesorgt, dafür gilt ihnen ein großer Dank.

Zum Abschluss will ich noch meiner Familie für ihre ständige Unterstützung während meines gesamten Studiums danken. Auf meine Mutter Anneliese, Vater Klaus, Bruder Hendrik und auch auf meine Tante Rita und Onkel Manfred konnte ich mich immer verlassen. Ebenso verlassen konnte ich mich immer auf meine Partnerin Sylvia Müller in den letzten sechseinhalb Jahren. Ihr stetige Unterstützung und Aufmunterung in schweren Zeiten hat mir sehr geholfen.

"Wenn ich weiter sehen konnte, so deshalb, weil ich auf den Schultern von Riesen stand." - Isaac Newton

Contents

Declaration

I hereby declare that I wrote this dissertation by myself and to the best of my knowledge and belief, used none but the indicated sources. I also declare that this dissertation or parts of it have never been submitted for any degree to any university or institute.

Date: .... Signature: ....

Niklas Dohmeier

Reviewers:

Prof. Dr. Günter Reiss

Prof. Dr. Thomas Huser

Motivation

Smart watches can detect an irregular heart beat that might evolve into an atrial fibrillation or if we fall and call an ambulance in case of an injury with a high accuracy, cars are able to prevent crashes and save lives.

Sensors are a key technology for the upcoming challenges in automatization like the control of a smart power grid embracing renewable energies, self driving cars or body near sensors monitoring our health. This is why new concepts of highly integrable, power efficient and high sensitive sensors have to be found.

CoFeB/MgO/CoFeB tunnel junctions are the ideal candidates for this type of sensor. They can be easily prepared by sputter deposition at room temperature with an ex situ post annealing process. Therefore they can be produced on large diameter substrates, resulting in a high production volume. Consequently, tunnel junction based sensors are used in *hard disk drives* (HDD) and *magnetoresistive random-access memory* (MRAM) [28, 52, 67, 83, 111].

A magnetic tunnel junction consists of two ferromagnetic layers, separated by a thin insulator. Due to the tunnel effect the electrical resistance is a function of the angle between the magnetizations (α) of the two electrodes. It can be described by the resistance at 0° (R_P), 90° ($\mathrm{R}_\perp$) and 180° (R_{AP}):

$$R(\alpha) = \frac{R_\perp}{1 + \frac{R_{AP} - R_P}{R_{AP} + R_P} \cdot \cos(\alpha)}$$

When applying strain to a magnetic material the inverse effect of magentostriction will induce a magnetic anisotropy, leading to a change in the direction of the magnetization. Compressive stress leads to an anisotropy parallel to the stress direction whereas the anisotropy caused by tensile stress is perpendicular. This is how a MTJ can convert applied mechanical stress into a change of electrical resistance.

One possible application for such sensors is in an *atomic force microscopy* (AFM). The current read-out system of an AFM is based on a laser that is focussed on the backside of the cantilever. The laser is reflected to a four segment photodetector [16]. The bending of the cantilever is detected by the movement of the laser spot on the photo diode. Depending on the distance between the tip of the AFM and the surface, the force can be attractive or repulsive [97]. When scanning with the tip over the sample, the surface can be reconstructed from these information.

A magnetic tunnel junction can be a replacement for this optical read-out system with various benefits. The optical system requires a lot of space and a complex adjustment. In contrast to that the *tunnel magneto resistance* (TMR) based system requires only a resistance measurement, opening up new opportunities to observe biological processes in real time.

Current CoFeB/MgO/CoFeB tunnel junctions sensors require an external magnetic field to serve as a sensor for an AFM [110]. A picture of such a device in shown in Fig. 1, together with a comparison of strain/read-out curve of the optical system and a magnetic tunnel junction. An external magnetic field is required because a collinear magnetized magnetic tunnel junction cannot differentiate between tensile and compressive stress. Without loss of generality it can be assumed that in absence of an external magnetic field the two electrodes are magnetized parallel. In this state the electric resistance is minimal. Either compressive or tensile stress will result in an increased resistance. Starting from an antiparallel state the resistance can only decrease.

This is why the external magnetic field will induce a non collinear unstrained state. The direction of the magnetization of the free layer is well defined by the external magnetic field and the different influence of tensile and compressive stress can now be distinguished. Detecting the bending of a cantilever would only need the cantilever itself. The detection system of an *atomic force microscope* (AFM) could be the size of finger nail. Since a resistance measurement is easy to run, the simplification of this measurement technique can open up this technology for other professions.

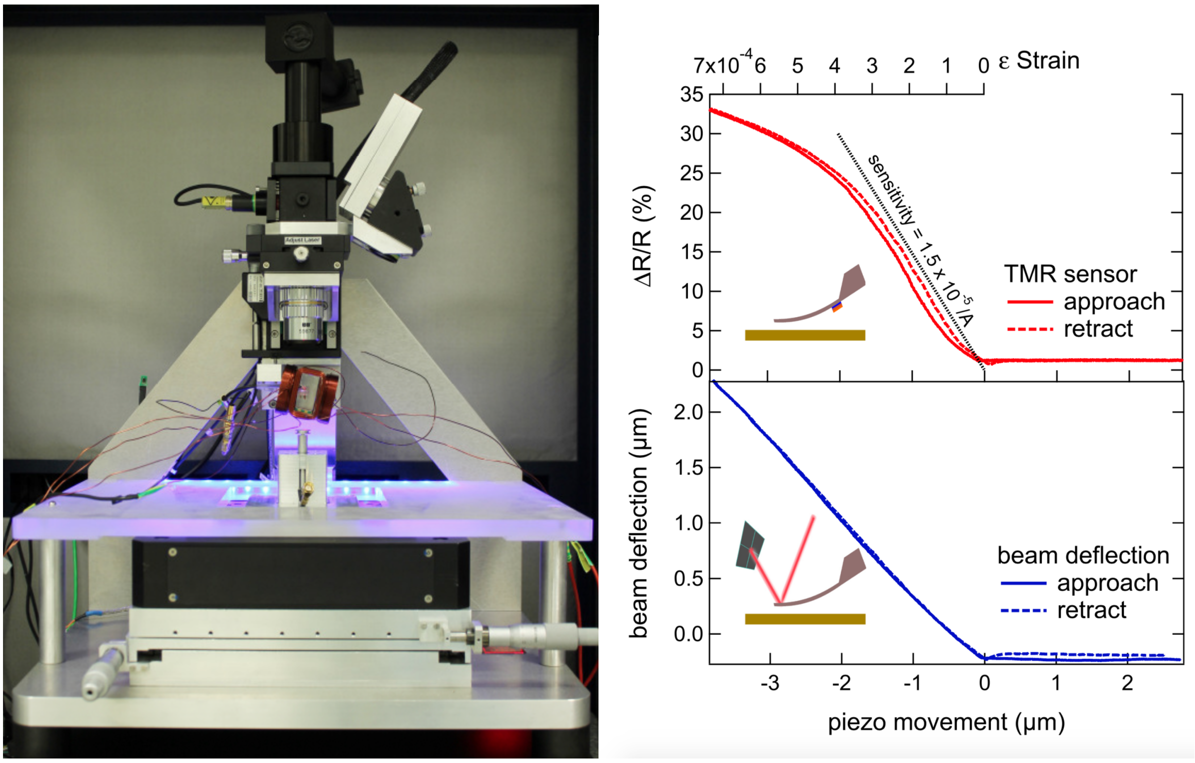

Figure 1 – **Left**: AFM equipped with a a self sensing TMR based read out system. On top an optical read out is installed as well for comparison. An electromagnet is currently needed to realize a non collinear magnetic state of the tunnel junction. **Right**: Comparison of a force/distance curve of the optical (bottom) and TMR based (top) read out system.

Abstract

The goal of this work is to design, characterize and produce TMR based sensors for mechanical stress in the absence of an external magnetic field. This goal is realized by pinning both electrodes in different directions.

The pinning is based on the natural antiferromagnet $\mathrm{Mn_{83}Ir_{17}}$. The characteristics of this antiferromagnet in terms of exchange bias and blocking temperature are investigated. Since pinning the top electrode is not possible by $\mathrm{Mn_{83}Ir_{17}}$ without an in-situ annealing step, a pinning with an artificial antiferromagnet is also studied.

The exchange bias induced by $\mathrm{Mn_{83}Ir_{17}}$ to a 5 nm $\mathrm{Co_{40}Fe_{40}B_{20}}$ layer is limited to approximately 350 Oe. The top pinning with an artificial antiferromagnet has a maximum pinning strength of 400 Oe and bottom pinning of almost 2000 Oe. Possible origins of the differences are figured out by transmission electron microscopy pictures of thin lamellas, fabricated by a focussed ion beam.

The primary focus of this work is research on non collinear magnetized, double pinned tunnel junctions. It is realized by different blocking temperatures and consecutive field cooling steps at different temperatures. The top pinning of the first sensor is based on a 7.5 nm $\mathrm{Mn_{83}Ir_{17}}$ whereas the bottom pinning is realized by a 20 nm $\mathrm{Mn_{83}Ir_{18}}$ layer. By a series of field cooling steps at increasing temperature, the heat treatment for the highest sensitivity with respect to an external magnetic field is found at 260 °C. In a four point bending apparatus the capability of distinguishing between tensile and compressive stress is proven. The gauge factors $\left(GF = \frac{\Delta R/R}{\Delta \varepsilon}\right)$ are $GF_{tensile} = 115 \pm 4$ and $GF_{comp} = -132 \pm 3$. These junctions have the ability to distinguish between tensile and compressive stress. At this pinning configuration, increasing the amplitude limited.

This is why an improved system with two artificial antiferromagnets is introduced. The pinning strength of the sensing layer is reduced from 200 Oe (natural antiferromagnet) to 80 Oe (artificial antiferromagnet). The thicknesses of the artificial antiferromagnets is kept the same. As a consequence, the optimum thermal treatment is the same compared to the prior system. The gauge factors increased to $GF_{tensile} = -280 \pm 4$ and $GF_{comp} = 390 \pm 3$.

To achieve a pinning strength of 80 Oe in a top pinning artificial antiferromagnet, different

thicknesses can be chosen. This is a result of the oscillating behavior of the interlayer exchange coupling.

Looking into the future of mass production, the reproducibility is also investigated on. A 2 nm thick ruthenium interlayer has a high reproducibility. The variation of bias of three consecutive samples is below 10 %. The combination of the knowledge on interlayer exchange coupling and magneto-optic Kerr measurements result in new techniques to measure the homogeneity of a deposition process on an angstrom scale on wafer level.

Chapter 1

Fundamentals

1.1 Collective magnetism

Collective magnetism in solids is based on the spin of the electrons. The spin is an intrinsic characteristic which behaves like an angular momentum. It has two possible orientations in an external magnetic field, they are mostly entitled *spin up* and *spin down*. The magnetism of materials is based on the interaction of the spins, the interaction with the orbital momentum and how they align. The Hamiltonian which describes the interaction of two neighboring spins (indicated with i and j) can be formulated as [22]:

$$\mathscr{H} = -2J\overrightarrow{S}_i \cdot \overrightarrow{S}_j \tag{1.1}$$

with the exchange constant J. A negative (positive) exchange constant leads to an antiferromagnetic (ferromagnetic) coupling, resulting in antiparallel (parallel) ordering. The exchange constant can be calculated from the exchange integral of overlapping spatial wave functions and Coulomb interaction (See Fig. 1.1)

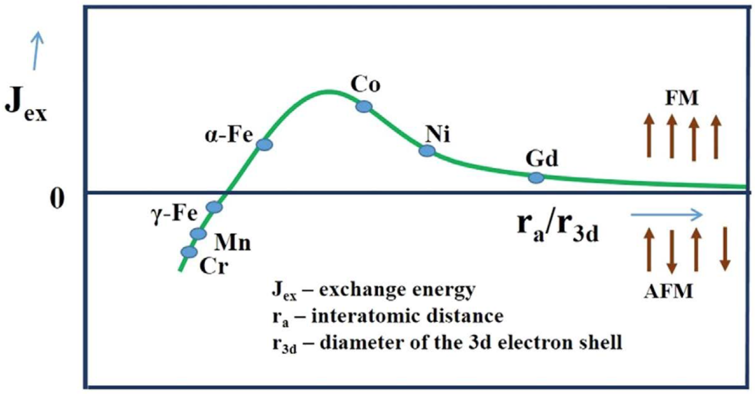

Figure 1.1 – Sketch of the Bethe-Slater curve. The exchange interaction is dependent on the ratio of the interatomic distance and diameter of the 3d electron shell. Taken from [20].

The magnetization of a material is the magnetic dipole moment per volume. The resulting magnetization (M) in an external magnetic field (H) is described by the magnetization or $M(H)$ curve. The spontaneous magnetization is a remarkable effect of ferromagnetism. The spins align parallel in the absence of an external magnetic field when below the *Curie temperature* (T_C).

In ferromagnetic materials such as iron or cobalt the spontaneous magnetization is related with *hysteresis*. The response of a ferromagnetic material is not linear or reversible. A typical magnetization or hysteresis curve of a ferromagnetic material is shown in Fig. 1.2.

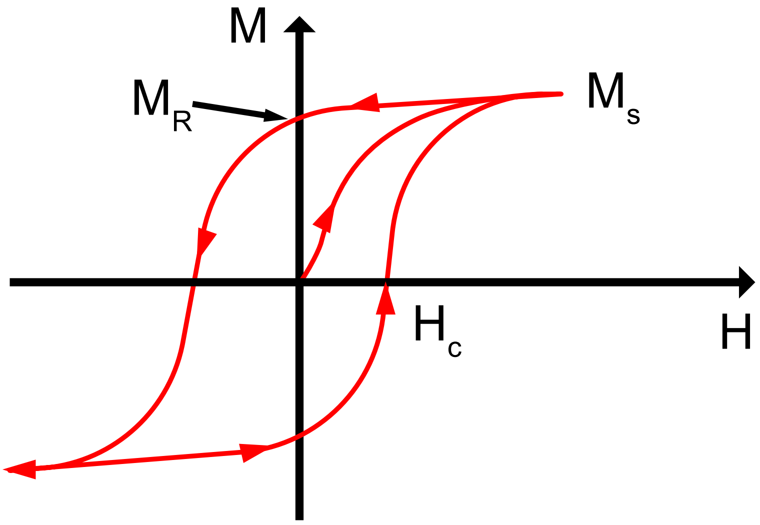

Figure 1.2 – Typical hysteresis curve of a ferromagnetic material. Starting from an initial magnetization curve into saturation. When decreasing the magnetic field, a magnetization remains until the coercive field is reached.

Starting from a non magnetized state the magnetic field (H) is increased and the microscopic magnetic domains align with the external magnetic field. At a magnetization of $M = M_S$ the ferromagnet is saturated. When the external magnetic field is decreased the magnetization does not follow its initial path. The remaining magnetization at zero field is called *remanence* (M_R). The required magnetic field to reach zero magnetization again is called *coercivity* (H_c). Materials with a high coercivity are called magnetically hard.
The parallel alignment of the individual spins is not the only nor the most common configuration found in different materials. The lattice structure of an antiferromagnetic material can be divided into two sub-lattices. The spins in the two sub-lattices align antiparallel, resulting in no net magnetic moment. The spins do not necessarily align in collinear sub-lattices. Different configurations are known such as MnSi or Mn_3Au with a helical or spiral spin structure [22]. The antiferromagnetic ordering is lost above the *Néel temperature* (T_N). Antiferromagnetic materials are important for exchange bias, which is explained Chap. 1.3.

1.2 Micromagnetism

The Landau-Lifshitz-Gilbert equation is a common way to describe the domain structure and magnetization dynamic ($\overrightarrow{M}(\overrightarrow{r},t)$) of a system:

$$\frac{d\overrightarrow{M}}{dt} = -\frac{\gamma_0}{1+\alpha_0^2} \cdot \left[\overrightarrow{M} \times \overrightarrow{H}_{eff}\right] - \frac{\gamma_0}{M_s} \cdot \frac{\alpha_0}{1+\alpha_0^2} \cdot \left[\overrightarrow{M} \times \left[\overrightarrow{M} \times \overrightarrow{H}_{eff}\right]\right] \tag{1.2}$$

γ_0**:** gyromagnetic ratio of the electron

α_0 : Gilbert damping factor

$\overrightarrow{H}_{eff}$**:** effective magnetic field

The effective magnetic field can be expressed by the negative derivative of the total energy density with respect to the magnetization:

$$\overrightarrow{H}_{eff} = -\frac{1}{\mu_0 M_s} \frac{\partial E}{\partial \overrightarrow{M}(r)} \tag{1.3}$$

In the problems simulated in this work, the energy density is a sum of four different terms:

$$E = E_{ex} + E_d + E_z + E_u \tag{1.4}$$

Exchange E_{ex}: The exchange energy is the reason of the spontaneous ferromagnetic ordering (see Chap. 1.1). In a volume (V) the exchange density can be expressed ass:

$$E_{ex} = \frac{A}{V} \int d^3r \left(\nabla \overrightarrow{M} / M_s \right)^2 \tag{1.5}$$

with the saturation magnetization (M$_s$) and the exchange stiffness ($A = {}^{4JS^2}/_{a}$). The exchange stiffness is dependent on the lattice constant for the bcc structure a and the two spin exchange integral J. A second important parameter is the exchange length:

$$l_{ex} = \sqrt{\frac{A}{\mu_0 M_s^2}} \tag{1.6}$$

This value defines the shortest range on which the magnetization can be twisted. Typical exchange length are: CoFeB ($4.7\,nm$), Co ($3,4\,$nm), Fe ($2.4\,$nm) [22, 119].

Demagnetizing E_d: The *demagnetizing energy* describes the energy of a magnetic material in its own demagnetizing field ($\overrightarrow{H}_d$):

$$E_d = -\frac{\mu_0}{2} \int d^3r \overrightarrow{M} \cdot \overrightarrow{H}_d \tag{1.7}$$

with the demagnetizing field:

$$\overrightarrow{H}_d = N_d \cdot \overrightarrow{M} \tag{1.8}$$

with the shape dependent demagnetizing tensor (N_d). The field is induced by the magnetization of the specium and its shape anisotropy.

Zeeman E_z: The Zeeman energy is caused by an external magnetic field (H):

$$E_z = -\mu_0 HM \cos(\theta) \tag{1.9}$$

with the angle (θ) between the magnetization and external magnetic field. This energy term is minimal when the magnetization aligns with the magnetic field.

Magnetocrystalline E_u: The magnetocrystalline energy is correlated to the lattice structure of a ferromagnetic material. In contrast to the spin, to orbital moment is coupled to the lattice. This results in an interaction, based on spin-orbit interaction, of the spins with the lattice structure. The magnetization prefers to align with certain crystallographic direction, they are called *easy axis*.

The magnetocrystalline energy can be, in the simple case of only one easy axis, expressed as:

$$E_u = K \sin^2(\theta) \tag{1.10}$$

with the anisotropy constant (K) and angle between the magnetization and easy axis (θ)

1.3 Magnetic pinning

For many applications it is important to reduce the influence of an external magnetic field on the magnetization direction of a magnetic layer. This can be realized by a so called *pinning,* meaning that a magnetic coupling is induced in a ferromagnetic layer. In this chapter, two different pinning methods of a ferromagnetic thin layer are discussed. The first part will review an exchange bias via a natural antiferromagnet. In this work $Mn_{83}Ir_{17}$ will serve as a natural antiferromagnet. The second part will focus on the concept of *interlayer exchange coupling* (IEC).

Exchange bias

Exchange bias (EB) is an effect, which occurs when a ferromagnetic material comes in contact with an antiferromagnetic material and is cooled through the *Néel temperature* (T_N) or the blocking temperature (T_B) of the *antiferromagnet* (AFM) with the *Curie temperature* (T_C) of the ferromagnet being larger than T_N or T_B. An unidirectional exchange anisotropy is induced at the interface [88].

The first time this effect was observed was in 1956 by Meiklejohn and Bean while investigating cobalt particles which were embedded in their native (antiferromagnetic) oxide CoO [77]. This effect can be found in various systems like small particles, ferromagnetic films on a single antiferromagnetic crystal or in thin films [78, 88]. The exchange bias effect has also been observed in other systems which involve ferrimagnetic materials, but they will not be discussed here, since only ferromagnetic-antiferromagnetic thin film interfaces are part of this work.

Exchange bias in a simple picture

The interface coupling of an antiferromagnet with a ferromagnet can be observed when a cooling process from a temperature above T_N and below T_C is done in the presence of an external magnetic field ($T_N < T < T_C$ to $T < T_N$). This is called a *field cooling process*. The hysteresis loop of a ferromagnet without any pinning is axisymmetric to the magnetization axis. After the field cooling process this symmetry is lost. In general the loop is shifted in the opposite direction to the magnetic field which was applied. This shift is known as the *exchange bias* (H_{EB}) while the *coercivity* (H_C) is increased. Both of these effects will vanish if the temperature is risen to a value which is around the Néel temperature of the antiferromagnet.

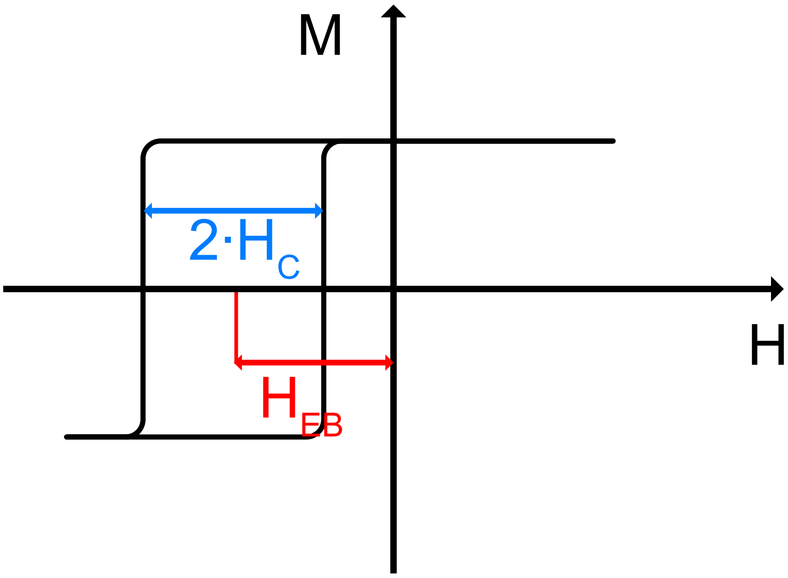

Figure 1.3 – Sketch of the Hysteresis loop $(M(H))$ which is exchange biased after a field cooling process. The exchange bias (H_{EB}) and coercivity (H_C) are indicated.

The energy per unit area can be expressed as:

$$E = -HM_{FM}t_{FM}\cos(\theta-\beta) + K_{FM}t_{FM}\sin^2(\beta) + K_{AFM}t_{AFM}\sin^2(\alpha) - J_{INT}\cos(\beta-\alpha) \quad (1.11)$$

with H being the external magnetic field, M_{FM} the saturation magnetization of the ferromagnetic layer, K_{FM} and K_{AFM} the anisotropy of the ferromagnet and the antiferromagnet with their corresponding thicknesses t_{FM} and t_{AFM} and J_{INT} the interface coupling constant. The corresponding angles are shown in Fig. 1.4.

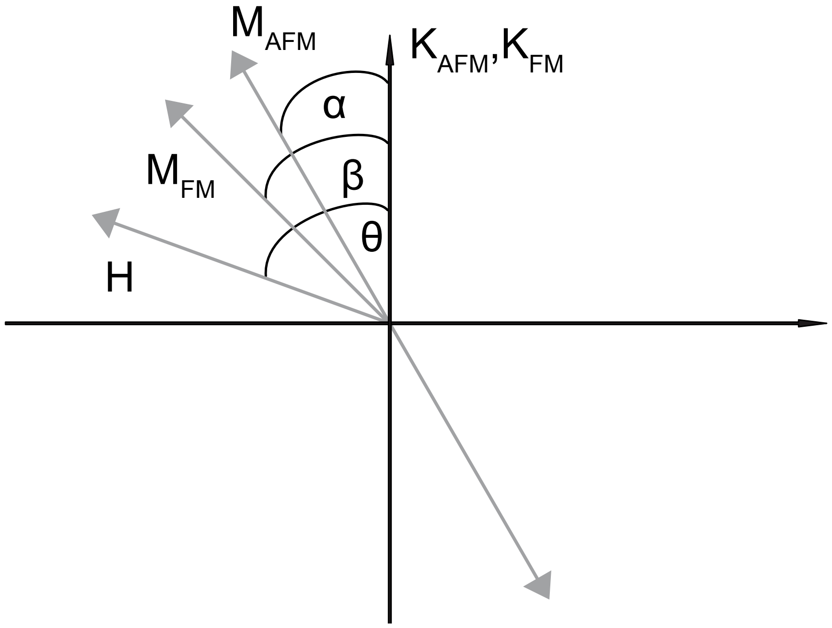

Figure 1.4 – Sketch of the relevant directions in an exchange bias system consisting of a ferromagnet and an antiferromagnet. The AFM sub-lattice magnetization has two directions and the anisotropy axis of both layers are assumed to be collinear.

The first term in Eq. 1.11 describes the influence of of an external magnetic field to the ferromagnetic layer. The second one accounts the ferromagnets anisotropy, the third the antiferromagnet's anisotropy and the last one the interface coupling.

In order to simplify this case the ferromagnets anisotropy will be neglected which is realistic in most experimental cases [88]. This why the energy can reduced to:

$$E = -HM_{FM}t_{FM}\cos(\alpha-\beta) + K_{AFM}t_{AFM}\sin^2(\alpha) - J_{INT}\cos(\beta-\alpha) \quad (1.12)$$

If an energy minimization is performed with α and β the loop shift can be expressed as:

$$H_E = \frac{J_{INT}}{M_{FM}t_{FM}} \quad (1.13)$$

$$K_{AFM}t_{AFM} \geq J_{INT} \quad (1.14)$$

which implies that the energy minimization leads to small "$\beta-\alpha$" angles so that the spins of the ferro- and antiferromagnet are about to rotate together. If this requirement is not met, the magnetization loop will not be shifted, because the spins of the antiferromagnet follow the ones of the ferromagnet.

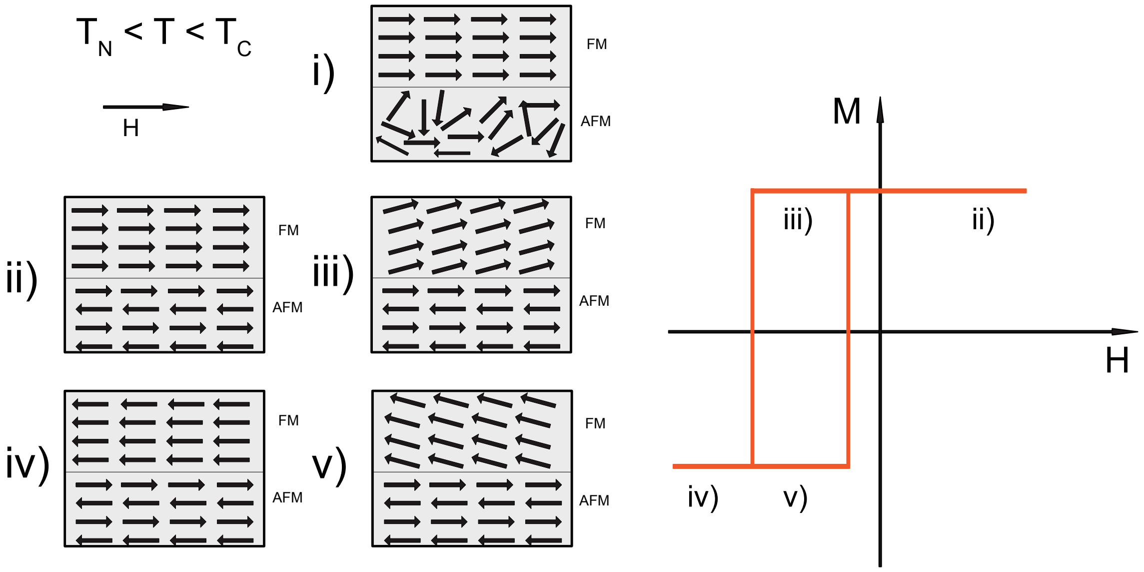

Figure 1.5 – Sketch of the spin configuration of an ferromagnet-antiferromagnet bilayer. Different stages during a hysteresis loop are shown. The arrows are only a simple representation, the actual spins may vary. Reproduced from Ref. [88].

Sign and ferromagnetic thickness dependence of exchange bias

Most of the time the exchange bias is antiparallel to the field cooling direction [88].

Due to the interfacial nature of the exchange bias effect, several experiments have been performed on the influence of the ferromagnetic layer thickness [63]:

$$H_{EB} \sim \frac{1}{t_{FM}} \tag{1.15}$$

This law applies until the ferromagnetic layer is not a complete film anymore, i.e. down to thicknesses of the ferromagnet of only around 1 nm.

Blocking temperature

The temperature at which the exchange bias is lost is called the *blocking temperature* (T_B). For single crystals and thick films of antiferromagnetic materials the blocking temperature tends to be equal to the Nèel temperature $(T_B \approx T_N)$. Contrary to this the blocking temperature of thin films is lower compared to the Nèel temperature $(T_B < T_N)$. The blocking temperature is not only a material parameter, but is determined by different parameters like the grain size, thickness, exact stoichiometry or different crystallographic phases of the antiferromagnetic thin film [36, 87].

$$T_B(D)/T_B(\infty) = 1 - (\xi/D)^{\delta} \tag{1.16}$$

with the bulk blocking temperature $T_B(\infty)$, the shift exponent $\delta = {}^{1}/{}_{2}\lambda$, which corresponds to the temperature-dependent antiferromagnetic moment $m_{AFM}(T) = m_{AFM}^{T=0}\left(1 - {}^{T}/{}_{T_N}\right)^{\lambda}$. The last parameter $\left(\xi = {}^{J_{INT}}/{}_{2ra \cdot K_{AFM}}\right)$ is dependent of the interface coupling exchange (J_{INT}), the magnetic anisotropy constant (K_{AFM}), the lattice constant (a) and grain size (r) of the antiferromagnetic layer [124, 125].

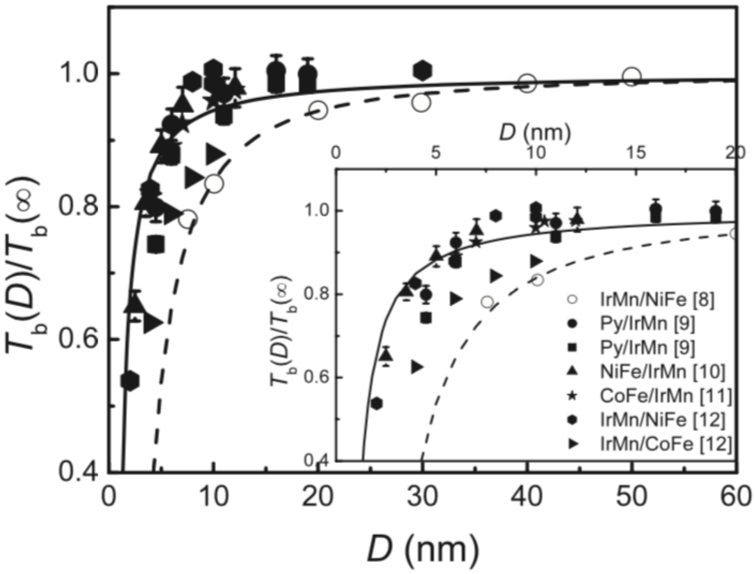

Figure 1.6 – Blocking temperature of different ferromagnet/antiferromagnet combinations with respect to the thickness of the antiferromagnetic layer [70]. Even for different antiferromagnetic materials the general trend of Eq. 1.16 is followed. The data is gathered from different sources. [6, 26, 36, 45, 125]

Training effects

It is often the case that the exchange bias H$_E$ is is non constant with respect to the number of hysteresis loops that the multilayer undergoes. During this training effect the exchange bias may decrease with an increasing number of hysteresis loops. In experiments the following relation can be observed [88]:

$$H_E - H_{e\infty} \propto {}^{1}/{}_{\sqrt{n}} \tag{1.17}$$

with n being the number of measurements and H_i the corresponding exchange bias values. The effect origins from reorientations of the antiferromagnetic domains during the magnetization reversal steps, which is why it is not observed in experiments in which the magnetization is only changed by a small angle and additionally it is more often observed in polycrystalline antiferromagnets and is small in single crystals.

1.4 Interlayer exchange coupling

Interlayer exchange coupling (IEC) is the phenomenon of a coupling between two ferromagnetic layers which are separated by a thin non- or antiferromagnetic layer [13]. This chapter gives a brief introduction on the basic concepts of understanding the origin and behavior of the coupling.

In the case of a nonmagnetic, metallic interlayer, the magnetic coupling is transferred by the electrons of the interlayer. When varying the thickness of the interlayer between the two ferromagnets, the coupling constant between the two ferromagnetic layers oscillates.

A very first observation of an antiferromagnetic coupling of two iron films, separated by a chromium spacer, was made by Grünberg et al. in 1986 [42]. The discovery of Parkin et al. gave an incentive to the research field as they discovered that the coupling strength in Fe/Cr/Fe and Co/Ru/Co oscillates as a function of interlayer thickness [91]. Later is was shown by Parkin that this effect is happening in almost any system which has a metal as a spacer [89].

The magnetic coupling energy per unit area can be written as:

$$E/A\,(\theta) = -J \cdot M_1 \cdot M_2 \cdot \cos(\theta) \tag{1.18}$$

with J being the interlayer-coupling constant and θ the angle between the two magnetizations (M_i). It is called bilinear coupling because the the energy per unit area is linear in both magnetizations. A positive (negative) coupling constant favors a parallel (antiparallel) alignment.

In this chapter the concept of interlayer exchange coupling will be explained. The model of a one dimensional potential well is very simple way to understand the basic ideas behind interlayer exchange coupling.

This model is made out of two barriers (A,B). They have the potentials V_A, V_B and widths L_A, L_B. Between these barriers exists a spacer which has the potential $V = 0$ and a width of D. The widths of the two barriers may be infinite. [117]

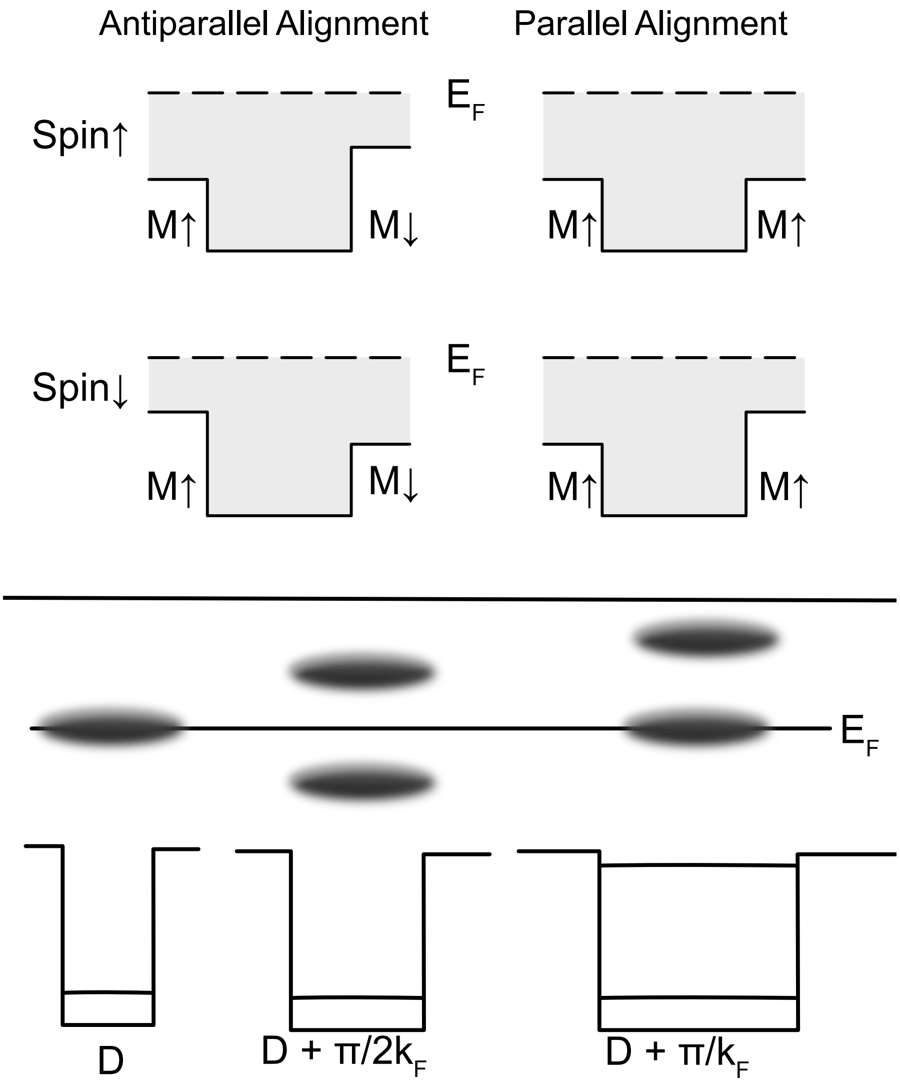

Figure 1.7 – **Top**: Sketches of quantum wells describing interlayer exchange coupling. The gray areas represent occupied states. The different potentials for spin up and spin down in parallel and antiparallel magnetization are shown. **Bottom**: Change of the resonance in the quantum well with increasing thickness. The lines illustrate the bound states in the quantum well and the ellipses the resonances. Reproduced from [107].

An electron is moving from left to right in the spacer with the wave-vector $(k^+ > 0)$. When reaching the barrier B it will be partially reflected with a complex amplitude $\left(|r_B|\, e^{i\phi_B}\right)$, leading to a wave-vector of k^-. At the barrier A the wave with an amplitude of $r_A = |r_a|\, e^{i\phi_A}$ is reflected again as seen in Fig. 1.8. The density of states is modified by the interference which occurs during these reflections. For one round trip the phase shift can be expressed with $q = k^{+} - k^{-}$ as:

$$\Delta\phi = qD + \phi_A + \phi_B \tag{1.19}$$

Constructive interference takes place when the follow condition is met:

$$\Delta\phi = 2\pi n \tag{1.20}$$

In the same manner, destructive interference takes places when:

$$\Delta\phi = (2n+1)\,\pi \tag{1.21}$$

The change in the density of states $(\Delta n\,(\varepsilon))$with respect to the interlayer thickness can expressed as:

$$\Delta n\,(\varepsilon) \propto \cos\left(qD + \phi_A + \phi_B\right) \tag{1.22}$$

It has to be taken into account that this change is also to proportional to the amplitude of the reflections (r_A, r_B), the width D of the interlayer and the density of states per unit energy. For interferences of higher order (due to several roundtrips in the spacer) the amplitude $|r_A r_B|$ has to be replaced with $|r_A r_B|^n$. Bringing together all of these considerations, the following equation is achieved:

$$\begin{aligned}
\Delta n\,(\varepsilon) &\propto \frac{2D}{\pi}\frac{dq}{d\varepsilon}\sum_{n=1}^{\infty}|r_A r_B|^n \cos\left(qD + \phi_A + \phi_B\right) && (1.23)\\
&= \frac{2}{\pi} Im \left(iD\frac{dq}{d\varepsilon}\sum_{n=1}^{\infty}\left(r_A r_B\right)^n e^{niqD}\right) && (1.24)\\
&= \frac{2}{\pi} Im \left(i\frac{dq}{d\varepsilon}\frac{r_A r_B e^{iqD}}{1 - r_A r_B e^{iqD}}\right) && (1.25)
\end{aligned}$$

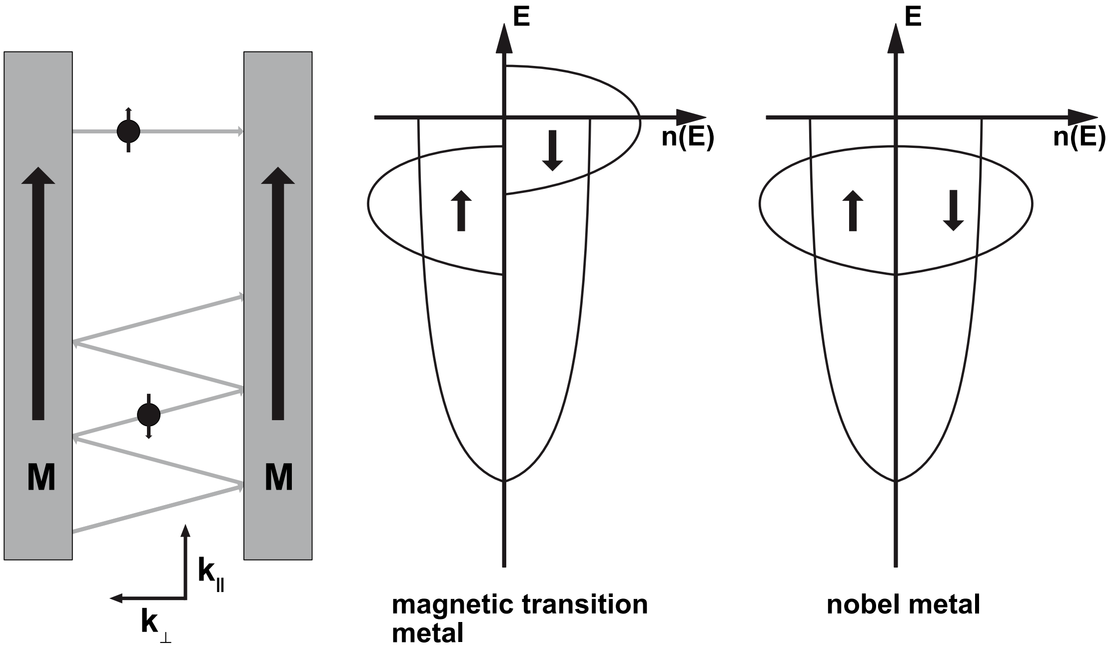

Figure 1.8 – **Left**: Reflection of the spin down electrons between the two ferromagnetic layers with a parallel magnetization. The spin up can transmit. **Right**: Sketch of the density of states of 3d magnetic metals and noble metals.

Because of the magnetic nature of the interfaces, spin-up and spin-down electrons scatter in a different manner. The only oscillations that do not cancel out are the ones at the Fermi energy [107]. This is why the fermi surface of the interlayer is of high relevance for interlayer exchange coupling. As a result in all models the critical spanning vectors of the fermi surface are of importance when calculating the period of the oscillation. Critical spanning vectors connect two sheets of the fermi surface towards the interface normal.

When going deeper into the theoretical description in a free-electron model, not only the periodicity of the coupling but also the coupling strength is taken into account.

The spin-dependent reflection results in a quantum confinement which results in quantum-well states. By changing the thickness of the interlayer, the energetic states in the quantum-well change as well. A strong spin-dependent reflection leads to a strong confinement which causes a strong coupling.

For the case of large spacer thickness, the coupling has the form:

$$J\left(D\right) = \Sigma_{\alpha} \frac{J^{\alpha}}{D^{2}} \sin\left(q_{\perp}^{\alpha} D + \Phi^{\alpha}\right) \tag{1.26}$$

With the different critical points α, the critical spanning vectors $q_{\perp}^{\alpha}$, the coupling strength J^{α} and the phase ϕ^{α}.

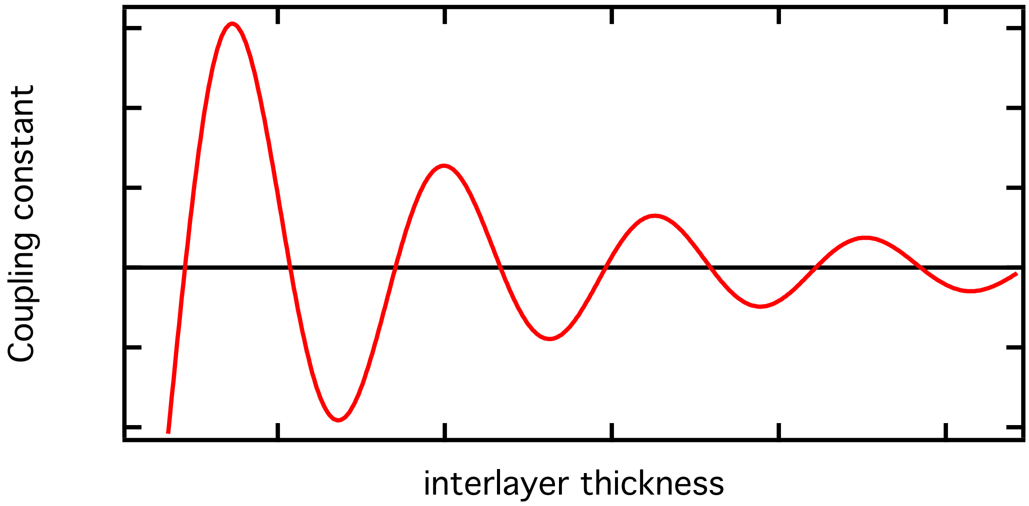

Figure 1.9 – Sketch of the oscillation of the interlayer exchange coupling constant with respect to the interlayer thickness.

For small thicknesses of the ferromagnetic layer a second oscillatory behavior is observed based on the same interference argument [11]. This effect is only mentioned but not explained since it plays only a role in much thinner ferromagnetic layers as used in this work ($t_{FM} \sim$ 1 nm).

1.5 Tunnel magneto resistance

According to quantum mechanics the probability for a particle to tunnel through a barrier of the height ϕ and width ω is given by the transmission coefficient (τ):

$$\tau = a \exp\left\{-b\omega\phi^{1/2}\right\} \tag{1.27}$$

with the constants a and b.

A tunnel junction consists of two ferromagnetic layers which are separated by a thin insulator. These electrodes are ferromagnetic materials with a high spin polarization. The insulator is called the *tunneling barrier* and its thickness is typically in the order of $1-3$ nm. The application of a bias voltage perpendicular to the sample decreases the resistance, as the potential of the barrier becomes asymmetric as seen in Fig. 1.10.

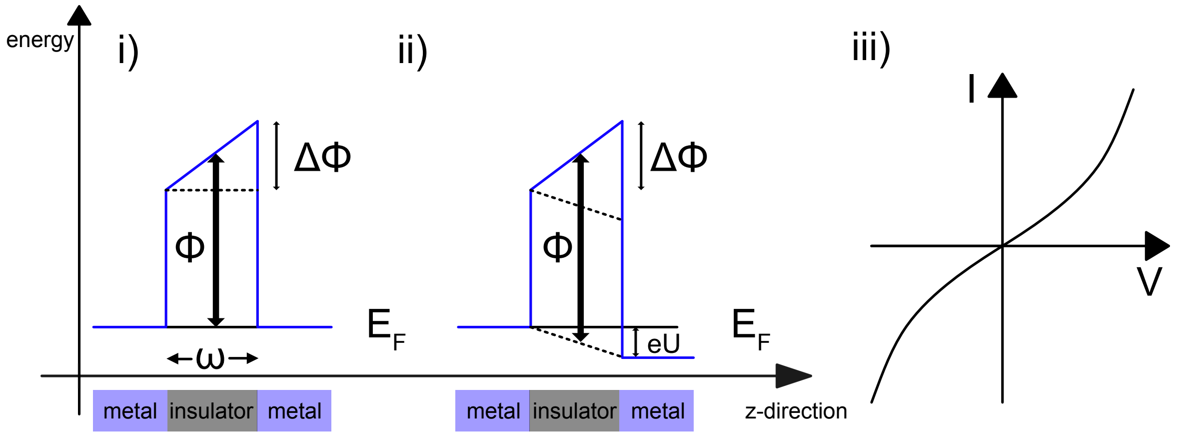

Figure 1.10 – i) and ii) potential landscape for a tunnel barrier between two ferromagnetic materials without (with) a voltage (U) applied. iii) Typical current voltage characteristic of a tunnel junction.

For low bias voltages the response of the junction is ohmic, but for higher voltages there is an additional U^3 term[10]:

$$I = G \cdot U + \gamma \cdot U^3 \tag{1.28}$$

For low voltages these parameters can be expressed as:

$$G = \left({}^{3e^2}\!/_{2\omega\hbar^2}\right)\sqrt{2me\phi}\cdot\exp\left(-\left(4\pi\omega/\hbar\right)\sqrt{2me\phi}\right) \tag{1.29}$$

$$\gamma = {}^{\pi m}\!/_{3\phi(e\omega/\hbar)^2} \tag{1.30}$$

with the electron charge (e), mass (m) and height (ϕ) and width (ω) of the tunneling barrier. The resistance of this trilayer depends on the angle between the magnetizations of the two ferromagnets.

In order to understand what happens when applying an external magnetic field, with no loss of generality, it can be assumed that one ferromagnetic layer (FM1) has a smaller coercivity than the other (FM2). When increasing the external magnetic field, the field strength will reach the coercivity of one of the ferromagnetic layers (FM1), the magnetization of this layer will align with the direction of the magnetic field. Depending on the direction of the magnetization of the second ferromagnet (FM2), the resistance will increase or decrease. If the field is increased to the value of the coercivity of FM2 its magnetization will align as well and there is another resistance change. This behavior and its impact on the resistance is shown in Fig. 1.11 for a spin-valve and pseudo spin-vale structure. In a spin-valve structure one ferromagnetic layer is pinned (e.g. through exchange bias induced by an antiferromagnet) and the other is a free layer. In a pseudo spin-valve both layers are free layer with different coercivities.

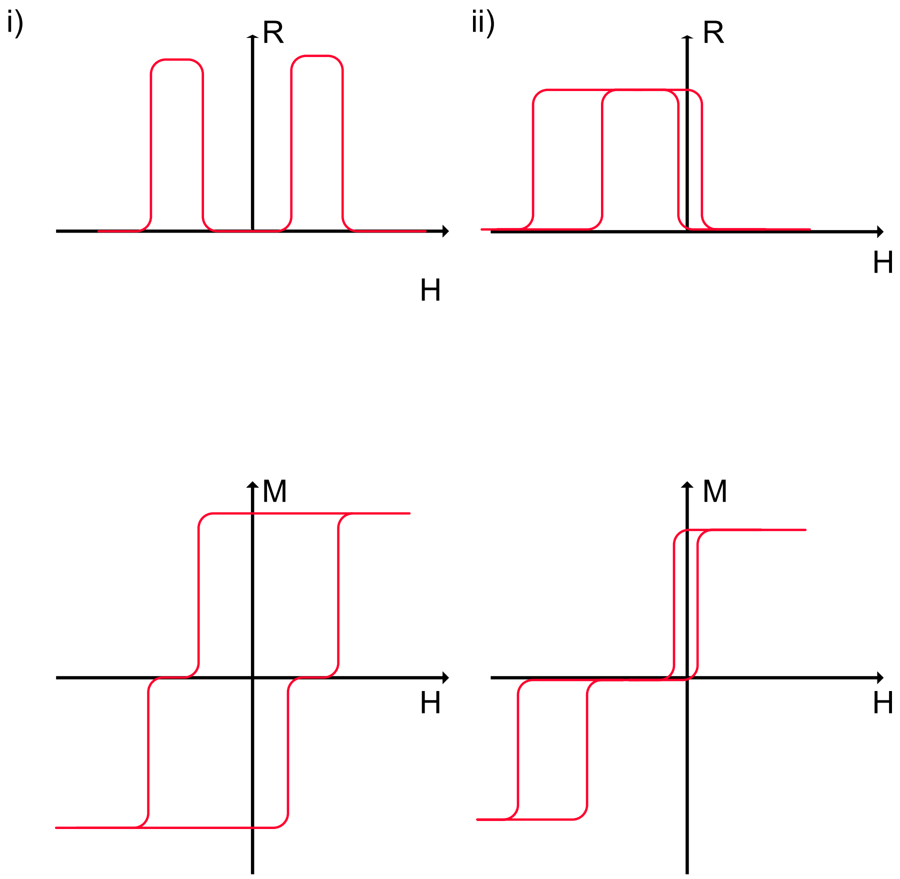

Figure 1.11 – Magnetization and magnetoresistance curves of spin valves and pseudo spin-valves. i) Symmetric magnetoresistance curve which is caused by different coercivities of the ferromagnetic layers. ii) One ferromagnetic layer is pinned by an antiferromagnet in an exchange biased spin-valve.

A description was made by Jullière in 1975 [62]. This model proposes *spin dependent tunneling* (SDT) as reason of this effect. This effect was already known and described by inequality of spin up and spin down electrons [80].

Jullière attributed the tunnel magnetoresistance (TMR) by the spin polarization P_1 and P_2 of the ferromagnetic layers at the Fermi level:

$$TMR = \frac{2P_1P_2}{1+P_1P_2} \tag{1.31}$$

In the case of identical electrodes this formula simplifies to:

$$TMR = \frac{2P^2}{1+P^2} \tag{1.32}$$

One assumption for this result is that the transmission probability is proportional to the product of the initial and final state density of states (N$_i$) of the two ferromagnets. This follows in the conductance (G):

$$G_P \propto N_{1\uparrow}N_{2\uparrow} + N_{1\downarrow}N_{2\downarrow} \tag{1.33}$$

$$G_{AP} \propto N_{1\uparrow}N_{2\downarrow} + N_{1\downarrow}N_{2\uparrow} \tag{1.34}$$

By defining the magnetoresistance as $MR = {}^{G_P - G_{AP}}\!/_{G_{AP}}$ and the polarization via the density of states at the Fermi level $P = {}^{N_\uparrow - N_\downarrow}\!/_{N_\uparrow - N_\downarrow}$, the result will be the formula of Jullière eq. 1.31.

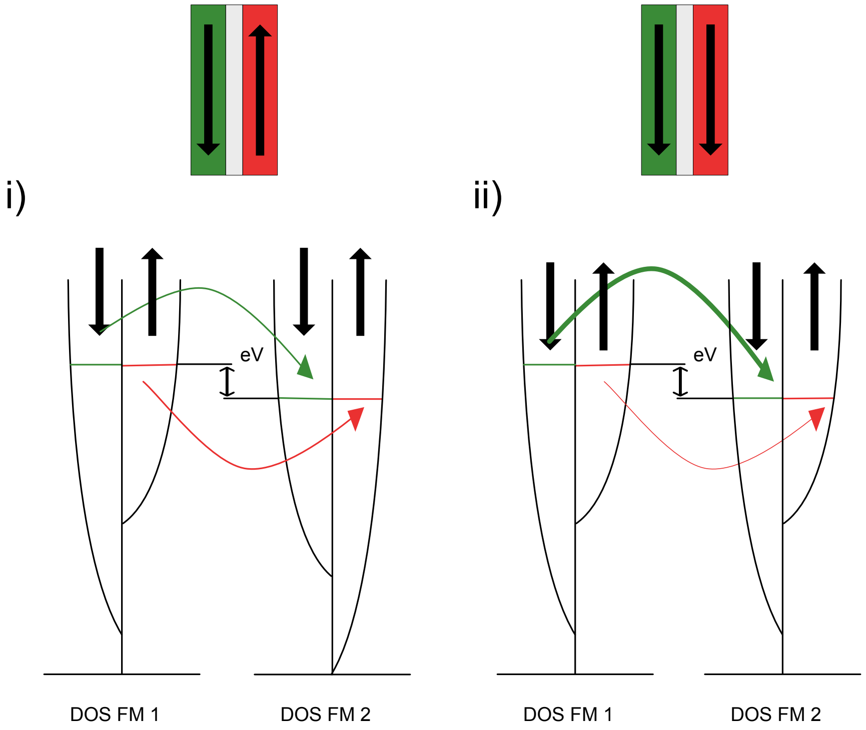

Figure 1.12 – Tunneling scheme for the two non redundant collinear magnetization directions in a tunnel junction, antiparallel (i) and parallel (ii). The tunnel current is pictured by the thickness of the arrows, indicating that in the parallel state a much higher current can be achieved.

Even though this formula is commonly used to calculate the P values, some has to keep in mind that it is only an approximation. More important for the coherent tunneling is the convolution of the Fermi surfaces of the both electrodes in contrast to the density of states at the Fermi level. With S being the cross sectional area of the Fermi surfaces the conductance in the different parallel and antiparallel state are $G_P \propto S_\uparrow + S_\downarrow$and $G_{AP} \propto 2S_\downarrow$, which leads to:

$$\frac{\Delta G}{G} = \frac{S_\uparrow - S_\downarrow}{2S_\downarrow} \tag{1.35}$$

Other parameters, like metal-insulator bonding, carrier mobility and band symmetry, also impact on the TMR amplitude. In addition to that, the bias voltage which is applied also impacts the effect size. Higher voltages generate more phonons and magnons which induce spin flips, leading to a lower TMR amplitude. For crystalline barriers (like MgO in this work) the spin filtering effects due to different symmetries of wave functions have a huge impact on the TMR ratio. This effect will be discussed in more depth in Chap. 1.6.

Non collinear magnetization

When investigating the magnetoresistance of magnetic tunnel junctions, only the parallel and antiparallel configurations of the magnetizations of the two electrodes are taken into account. As an opposite to that non collinear configurations can be examined as well. Different external influences may lead to this state, e.g. an external magnetic field, shape anisotropy or mechanical stress that induces an anisotropy. Early descriptions of the angular dependence of the magnetoresistance were made by Slonczewski and Jaffrès [58, 102]. The resistance can be described by a cosine relationship:

$$R(\alpha) = \frac{R_\perp}{1 + \frac{R_{AP}-R_P}{R_{AP}+R_P} \cdot \cos(\alpha)} \tag{1.36}$$

With the resistance at at an angle of 0° (R$_P$), 90° (R$_\perp$) and 180° (R$_{AP}$) between the magnetizations.

Every angle between the two magnetizations is related to a certain resistance. An angular dependent resistance measurement is shown in Fig. 1.13.

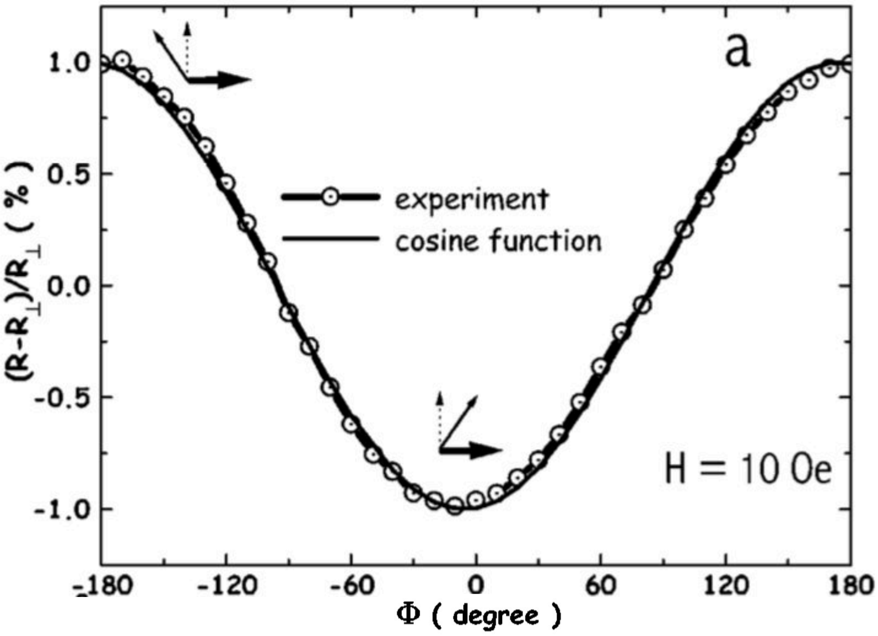

Figure 1.13 – Angular dependence of the resistance of a Co/Al_2O_3/Co/CoO/Au junction. An external field of 10 Oe was applied and rotated, indicating the cosine like behavior of the resistance. Image taken from Jaffrès et al. [58].

1.6 CoFeB/MgO/CoFeB tunnel junctions

For a long period of time the best performing magnetic tunnel junctions did use an aluminum based tunnel barrier. A TMR effect of 70 % at room temperature was achieved [82, 83, 117]. This TMR ratio can be easily explained by the model of Jullière.

Coherent tunneling, which can be found in Fe (001) / MgO (001) / Fe (001) single crystal, can lead to much higher TMR ratios [14, 30, 56]. The tunneling probability through a crystalline barrier is highly dependent to the conservation of the coherence during the tunneling process. The electronic states of the conduction electrons that have a wave function that is totally symmetrical respecting the normal axis of the barrier have a much higher tunneling probability.

In order to understand an important mechanism in the tunneling process through crystalline MgO, the different symmetries of the wave functions have to be taken into account. These symmetries are labeled as Δ_X symmetries. The wave functions of these bands are compatible to atomic orbitals. For example the compatible orbitals to the Δ_5 band are p_x, p_y, d_{xz} and d_{yz}. The Δ_1 symmetry is compatible to s, p, and $d_{3z^2-r^2}$ states.

In the case that the symmetry at the interface between barrier and ferromagnetic layer is

maintained, the wave function of different Δ_X will decay in the barrier at different rates. For MgO barriers, the Δ_1 symmetry decays at the lowest rate. In order to transfer this symmetry filter into a spin filter, an electrode has to be found which has a high spin polarization at the Fermi energy for this symmetry.
The Δ_1, $\Delta_{2'}$ and Δ_5 bands have a high density of states for the spin majority and for the Δ_2, $\Delta_{2'}$ and Δ_5 for the minority. The difference in the Δ_1 origins from a shift in the *d* band. Epitaxial grown Fe (001) / MgO (001) / Fe (001) tunnel junctions have high TMR ratios, but it is hard to use them in application because of the need of a high crystal quality. With the same line of argument, the in FeCo (001) / MgO (001) / $(Fe_{70}Co_{70})_{80}B_{20}$ system enabled to push the TMR from 188 % to 220 %[103].

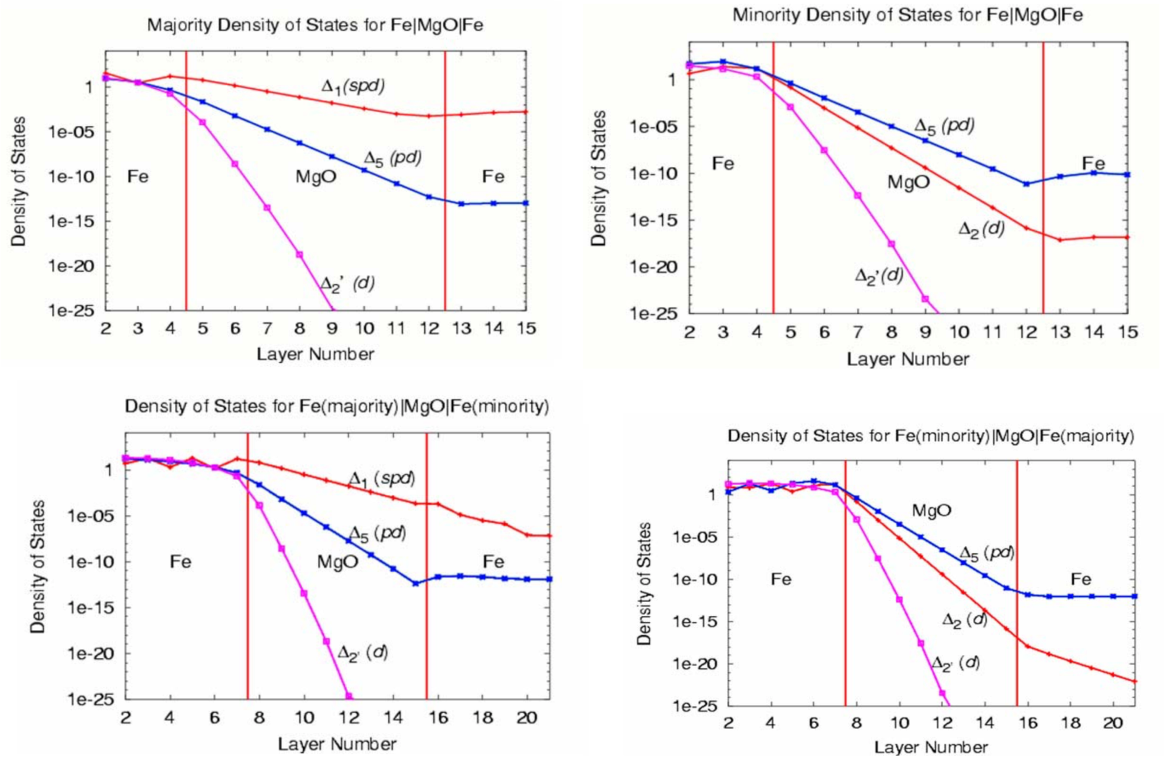

Figure 1.14 – Absolute square of the wave function of different symmetries. **Top**: Tunneling for parallel magnetization. **Bottom**: Wave functions for the different antiparallel states. Taken from [14].

An easier way to prepare current state-of-the-art systems is based on CoFeB / MgO / CoFeB tunnel junctions [47]. In application it is often necessary to induced a magnetic pinning to one of the electrodes. Tunnel junctions that require a single crystalline substrate are not suitable for this purpose whereas CoFeB is prepared as an amorphous layer during sputter deposition. In contrast to the theoretical considerations that the epitaxial grown electrodes are required, the MgO which is sandwiched between the two amorphous CoFeB layers grows in the (001) rock salt structure. It is preferred for tunneling, which is indicating that this crystal structure is energetically preferred [64]. Another advantage of an amorphous electrode is the reduction in lattice mismatch. Because of this the quality of the barrier can be improved which results in higher TMR values.

In order to get high TMR ratios above 600 %, typically a post annealing process is performed [55]. After the deposition process the TMR rate is about $15-30\,\%$. Starting at an annealing temperature of 360 °C the TMR value increases drastically. A further increase of the temperature affects the TMR ratio only at a very low level until it decreases after 450 °C, as seen in Fig. 1.15.

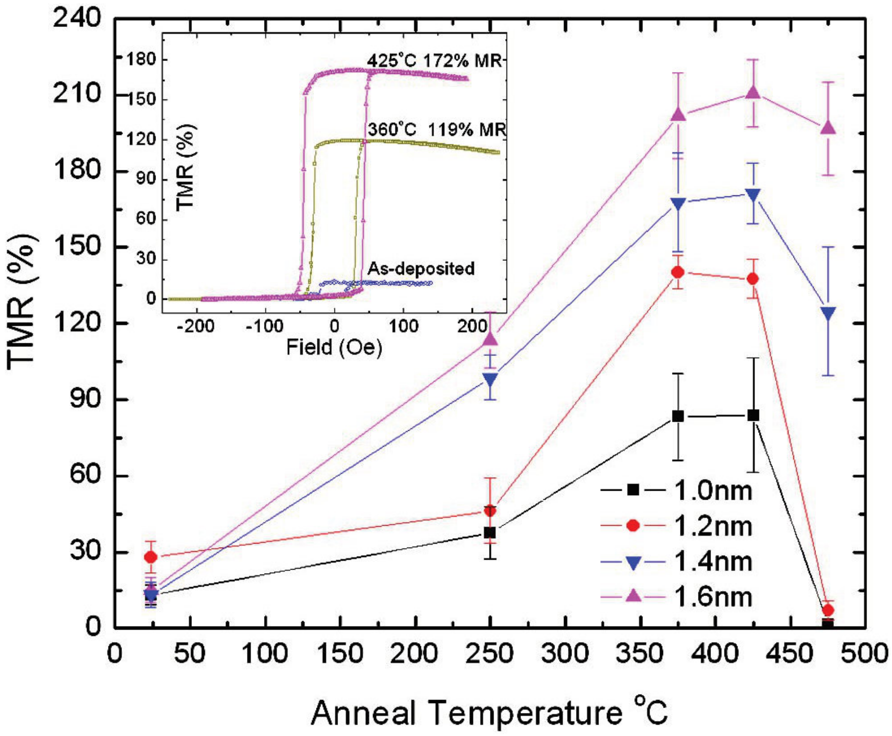

Figure 1.15 – TMR ratio depending of the annealing temperature for different MgO barrier thicknesses. The optimum value is in the range of 375 °C to 425 °C [100].

During the annealing process crystalline, bcc CoFe is formed at the interface. The MgO acts as a seed for the crystallization at the barrier-electrode interface while the interface is sharpened as well. A possible explanation of the drop in the TMR ratio at high temperatures is the diffusion of Ta, Ru, or Mn into the barrier or electrodes [46, 55, 71].

Of particular interest is the diffusion of boron in magnetic tunnel junctions. Boron is known to diffuse not into the barrier of a magnetic tunnel junction but away from the barrier-electrode interface [66, 69, 121]. This is crucial for the CoFe crystallization but the boron might disturb other layers e.g. in antiferromagnets which are used for pinning the electrodes. These antiferromagnetic materials are very sensitive to disruption of the crystal structure or composition. This is why in pseudo spin valve structures, a tantalum layer is used as a diffusion sink for boron which cannot be used in spin valve structures.

1.7 Magneto-optic Kerr effect

Measuring the *magneto-optic Kerr effect* (MOKE) is a powerful tool to investigate on the magnetic properties of a material. This work does not focus on exploring all the details of MOKE like quadratic effects. MOKE is used as a tool to measure the magnetic anisotropies and exchange interactions. The MOKE setup is described in Chap. 2.5.

Basic description of the origin of MOKE

The magneto-optic Kerr effect describes the phenomenon that linearly polarized light changes its polarization direction (θ_K) and ellipticity (ε_K) during reflection on a magnetized sample (see Fig. 1.16).

Linearly polarized light can be pictured as two waves with circular polarizations and different helicities. In the following way the rotation of the polarization can be interpreted as a phase shift between these two waves. The shift is generated by different velocities of the different helicities, it is called circular birefringence. If the cause of this effect is a magnetic field, this effect is more precisely defined as magnetic circular birefringence. The rotation of the polarization direction is described by the Kerr-angle:

$$\theta_K = \theta^r - \theta^i \tag{1.37}$$

The angles $\theta^{r/i}$ of the incident (i) and reflected (r) light are referring to a fixed reference angle. The second observation to be explained is the induced ellipticity. Not only the phase between the two waves is changing, but the amplitude as well. The difference in the absorption coefficients creates this circular dichroism. The Kerr-ellipticity (ε_K) expresses the ratio of the half-axis of the electromagnetic waves as display in Fig. 1.16.

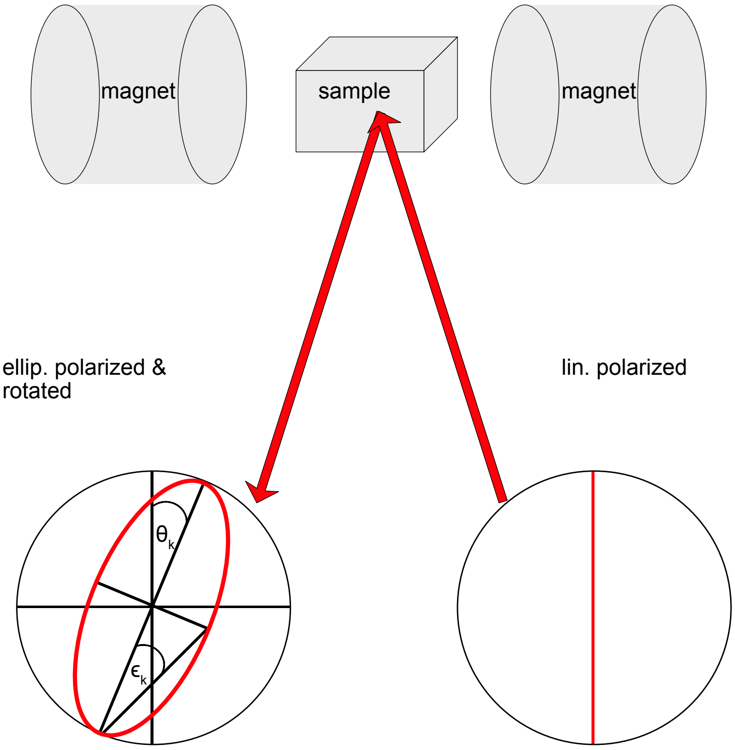

Figure 1.16 – Basic principle of MOKE. Linear polarized light is reflected on a sample which is magnetized by a magnetic field. The polarization of the light is changed during the reflection. The polarization is rotated by the angle θ_K. After the reflection the light is elliptic as well with a Kerr ellipticity angle of ε_K

Different MOKE geometries

In general MOKE is not only depended on the magnitude of the magnetization $|\overrightarrow{M}|$ but also on the relative angle between the incidence plane of the light and the surface of the sample. The three dimensional magnetization vector can expressed in three orthogonal components. The three basic geometries are shown in Fig. 1.17. In this work LMOKE is measured, but the other effects are mentioned for the sake of completeness.

Longitudinal moke

The longitudinal MOKE (LMOKE) is generated of the magnetization component which is parallel to the direction of the incoming light. It influences Kerr rotation and Kerr ellipticity. The intensity is not affected. The magnitude of the LMOKE depends on the incidence angle. On normal incidence the effect will vanish while it is high for a grazing angle.

Polar moke

The polar MOKE (PMOKE) is connected to the magnetization component which is perpendicular to the sample plane. It changes the polarization, but not the intensity of the light. In contrast to LMOKE, the signal from PMOKE is at a maximum for normal incidence of the light.

Transversal moke

Transversal MOKE (TMOKE) is a consequence of the magnetization component which is perpendicular to the incidence plane of light and in the sample plane at the same time. It changes only the intensity of the light while no Kerr rotation or ellipticity is generated. Comparable to LMOKE, it vanishes in the normal incidence geometry.

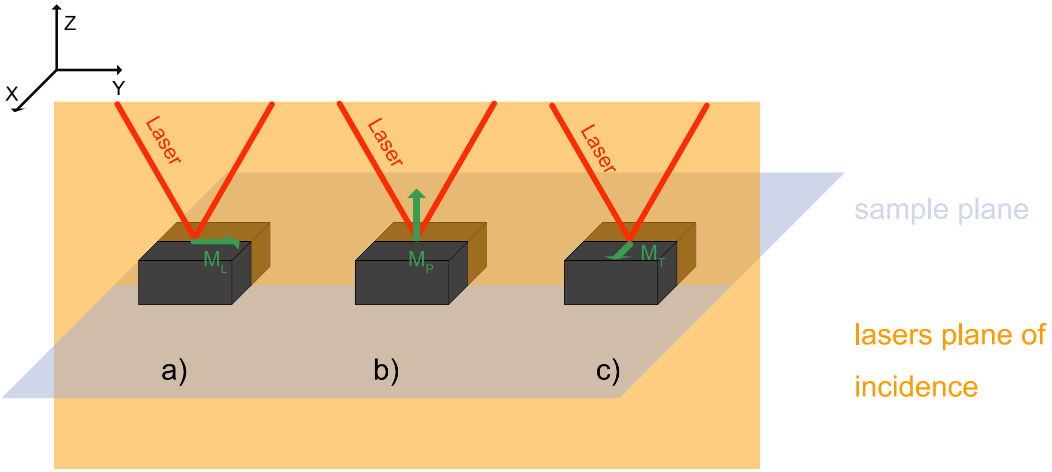

Figure 1.17 – The three common MOKE geometries. a) LMOKE b) PMOKE c)TMOKE. The incidence angle of the light is shown with respect to the sample surface.

1.8 Magnetostriction

Almost all ferromagnetic materials change their dimension when magnetized. This effect is called called “magnetostriction” (λ) and the change of the shape results in an induced strain (ε). Two different effects have to be distinguished, spontaneous and field induced. Both effects describe a relative change (ΔL) in length along the magnetization direction:

$$\lambda = {}^{\Delta L}/_{L} \tag{1.38}$$

The change in length can be positive or negative. When a ferromagnetic material is cooled down through the Curie temperature (T_C) magnetic domains are formed. This formation results in an isotropic, non volume conserving, spontaneous magnetostriction.

The origin of magnetostriction (spontaneous and field induced) is based on atomic scale magnetism with a limited length scale of angstroms.

The spin-orbit coupling in a ferromagnetic material will cause a change in the orbits when the magnetic domains are changed by an external magnetic field. These electron orbits are not only coupled to the spins but also to the crystal lattice. As a consequence the lattice is deformed.

Magnetostriction was discovered by Joule in 1842 [61]. He did show that nickel and iron perform an anisotropic change of their length, depending on an external magnetic field. The saturation magnetostriction (symbolized as λ_s) is the relative change of the length of the examined object ($\lambda_s = {}^{\Delta L}/_{L}$). As an example the saturation magnetostriction of iron is $\lambda_s = -7 \cdot 10^{-6}$. This means that a specimen will contract by 7 ppm when it is fully magnetized. Since the volume is conserved in this process, it will expand in the perpendicular direction:

$$\lambda_{\|} + 2 \cdot \lambda_{\perp} = 0 \tag{1.39}$$

The linear magnetostriction is depended on relation between crystal axes and the direction of magnetization.

A rectangular magnetic object as shown in Fig. 1.18 is in a non magnetized state. The domain walls are divided by their angle with respect to the magnetization direction in 180 °and non-180 ° walls.

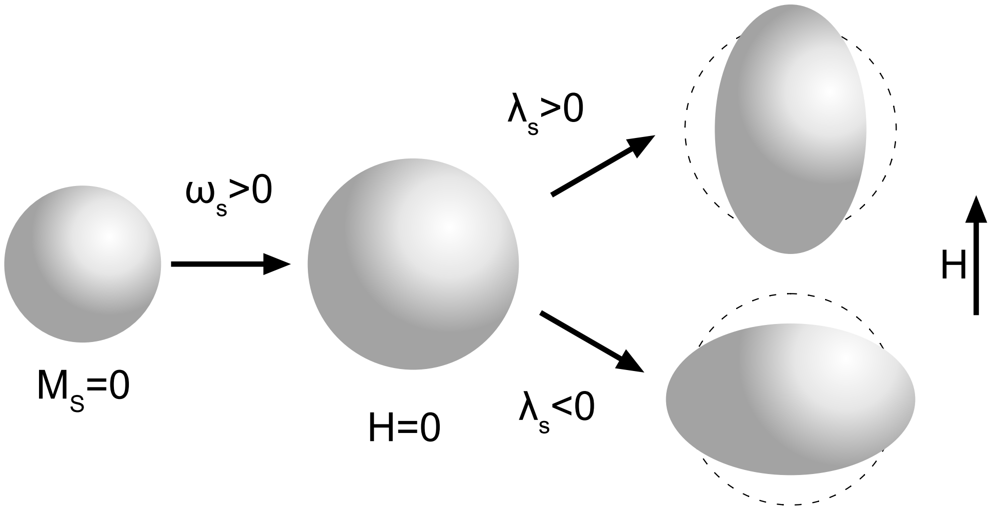

Figure 1.18 – Influence of spontaneous volume and linear magnetostriction on the shape of a particle.

Since the effect of magnetostriction correlates with strain (second order tensor ε_{ij}) and the magnetization which is a first order tensor M_k it results in a third order tensor. In the case of a polycrystalline or amorphous material it is possible to describe magnetostriction with a single parameter. Looking at cubic iron the two necessary parameters are [76][22]:

$$\lambda_{100} = 15 \cdot 10^{-6}$$
$$\lambda_{111} = -21 \cdot 10^{-6}$$

$$\lambda_s = {}^2\!/_5\,\lambda_{100} + {}^3\!/_5\,\lambda_{111} \tag{1.40}$$

Resulting in the isotropic average of $-7 \cdot 10^{-6}$. Large magnetostriction can be found in rare-earth alloys such as $SmFe_2$ ($-1258\,\mathrm{ppm}$) or $TbFe_2$ ($+2000\,\mathrm{ppm}$) [41]. Across the magnetostrictive materials the group of CoFe and CoFeB based alloys are of special interest due to the fact they are used as electrodes in tunnel junctions as well because of their high TMR amplitude. The composition $Co_{43}Fe_{43}B_{14}$ has the highest magnetostriction with $\lambda_s = 120\,\mathrm{ppm}$ [73].

The inverse effect can be used for stress sensors based on magnetic materials. It is known as *Villari* effect or inverse magnetostriction [116]. A material with a positive magnetostriction will elongate during its magnetization. Tensile stress, elongating a specimen, results in an anisotropy parallel to the stress direction. Compressive stress leads to an anisotropy perpendicular to the stress. Due to this effect a non magnetized specimen will change its domain structure but not magnetize. This effect is display in Fig.1.19. A magnetized sample will change the direction of its magnetization due to the induced anisotropy (the anisotropy is displayed in orange in Fig. 1.19). When applying tensile stress, the magnetization aligns with the stress axis. In the case of compressive stress, the magnetization rotates into a perpendicular direction of the stress.

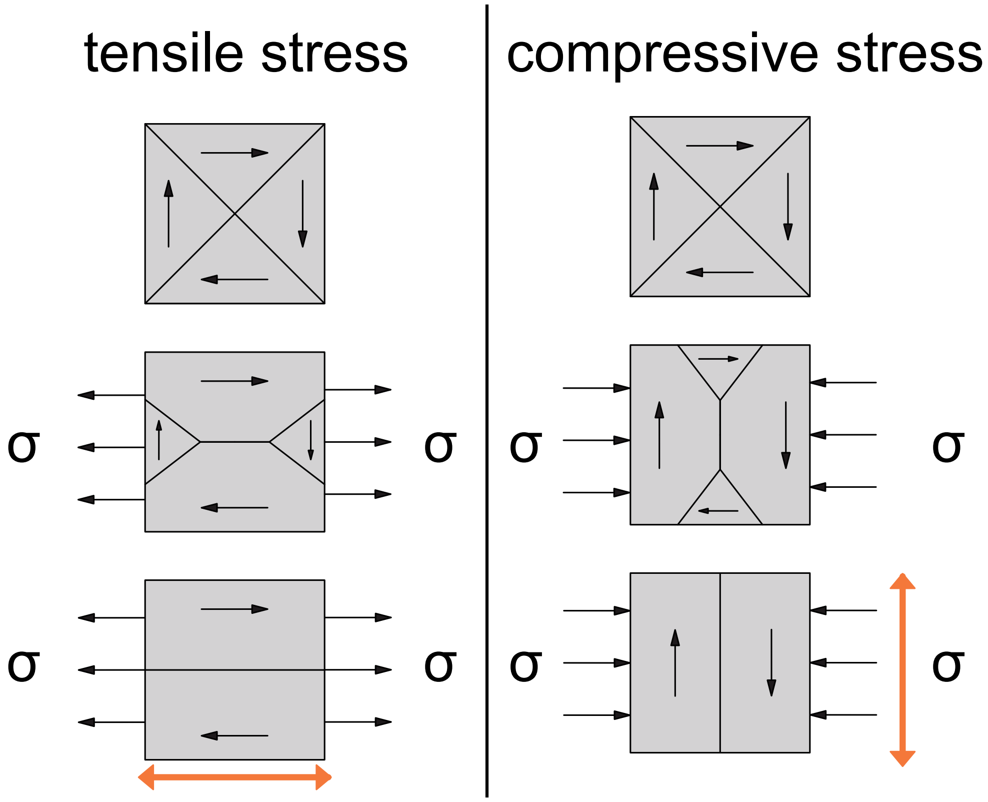

Figure 1.19 – Sketch of the change of the domain structure due to the influence of tensile (left) and compressive (right) stress. The specimen is unmagnetized, ferromagnetic specimen and has a positive magnetostriction ($\lambda > 0$). In orange displayed is the induced magnetic anisotropy, resulting in an easy axis. Reproduced from [24].

Chapter 2

Experimental Techniques

This chapter focuses on two main topics. At first a description of the experimental techniques which have been used to prepare and investigate the magnetic thin films.

The process starts with the deposition of the different layers via dc- and rf-magnetron sputtering. In a combined ex-situ annealing and field cooling process, the pinning direction of the antiferromagnets, a crystallization of several layers is defined. Information about the magnetic coupling strength are gathered via magneto-optical Kerr measurements. For electric and magnetostrictive measurements tunnel elements are patterned with a size of $56.25\,\mu\text{m}^2$ to $506\,\mu\text{m}^2$(circular and rectangular shape). This patterning via UV lithography and ion etching is divided in several steps. They are described in Chap. 2.3. For measuring the crystal structure of different layers of a complete TMR stack, thin lamellas are prepared by a *focussed ion beam* (FIB). These lamellas are studied by *transmission electron microscopy* (TEM).

In the second part of this work the concepts of creating cross pinned *magnetic tunnel junctions* (MTJ) are explained. Three different parts of the TMR stack are explained: The buffer, tunnel junction and artificial antiferromagnet.

Different effects like exchange bias, interlayer exchange coupling and the blocking temperature dependence of a natural antiferromagnet are explained separately in the first part of this work (Fundamentals). It is explained how these effects are connected to prepare cross pinned TMR sensor.

2.1 Sputter deposition

All thin-film samples prepared and investigated are made by magnetron sputtering deposition. This chapter explains this technique in different stages. Starting from the plasma generation to dc-sputtering. For increased efficiency a magnetic field is introduced. At the end two different variants are explained: rf- and reactive sputtering.

Plasma generation

Sputter deposition is a plasma based *physical vapor deposition* process (PVD). A plasma (in thin-film production most of the time argon is used as a sputtering gas) consists of a mixture of electrons, gaseous neutral and ionized atoms. In a plasma the share of ionized atoms is only a small fraction. For example at a pressure of 80 mbar the degree of ionization of argon is in the order of 5×10^{-6} [101]. This mixture of argon ions and free electrons cannot exist for a long time period. This is why free electrons have be constantly generated by an external power source. A dc power source or microwave radiation are two possibilities.

An electric field which will accelerate electrons contained in the gas and emitted from the cathode. These first electrons can be generated by natural radioactivity, background radiation or statistical thermal emission from the cathode. These electrons are accelerated by the electric field and after a certain threshold energy, new ions can be generated by collisions with gas atoms. The value of this threshold is a function of gas pressure and ionization potential. These additional electrons generate a higher degree of ionization, leading to the so called “gas breakdown”. The plasma is generated and because of the recombination the characteristic radiation, that is emitted by the plasma can be observed.

Sputtering

Sputter deposition is one practical application of the plasma generation, described above. In this procedure the ions which are generated in the plasma, are accelerated on a target disk. By this “bombardment” atoms of the target material are removed from the surface. The cathode is “sputtered”. In most cases the term “cathode” is used for the housing of the “target”, which consists of the material desired to be deposited. The number of atoms ejected from the target per ion is called the “sputtering yield”. The most important dependencies of the sputtering yield are energy, mass and incident angle between the ions of the sputtering gas and the target material. The collision of the ions with the target transfers generally kinetic energy with different results:

1. heating up the surface
2. rearranging atoms, resulting in defects
3. ion implantation
4. material ejection from the target
5. ion scattering

6. emission of X-rays

For sputter deposition point 4 is necessary, the bullet points two to four are important for ion etching, which is part of the patterning process to obtain devices. (see Chap. 2.3)

Magnetron sputtering

There are several disadvantages of this simple sputter deposition technique, for example a low sputtering yield, high energy consumption and as a consequence a generation of undesired X-rays. One way of addressing these problems is by introducing a magnetic field perpendicular to the electric one. The secondary electrons are not lost at the anode but bend away. Thus the use of a magnetic field will increase the probability of collisions and as a result ionization.

The direction of the magnetic field (either generated by a permanent or electro magnets) is parallel to the cathode surface. The resulting force applied to an electron is a superposition of the electric and magnetic force $\left(\overrightarrow{F} = e \cdot \overrightarrow{E} + e \cdot \overrightarrow{v} \times \overrightarrow{B}\right)$. A description of the set of coupled differential equations can be found here [101].

The next paragraph describes the trajectory of an electron during sputter deposition. The following coordinate system is used: y-axis normal to the surface of the cathode and the x-axis perpendicular to the magnetic field.

After emerging from the cathode, the electrons have almost no velocity in any direction. The electric field accelerates them in y-direction. Because of the magnetic force, a velocity component parallel to the x-direction is induced. This velocity results (again due to the magnetic force) in an acceleration in negative y-direction. This bending results in a non linear travel path of the electrons to the anode. The electrons go back to the cathode with an increased velocity (compared to its emission) and repeat the steps. The electrons stay near the cathode until they collide with a gas molecule. The extension of this travel path increases the ion generation efficiency, making magnetron sputtering an efficient way of preparing thin films.

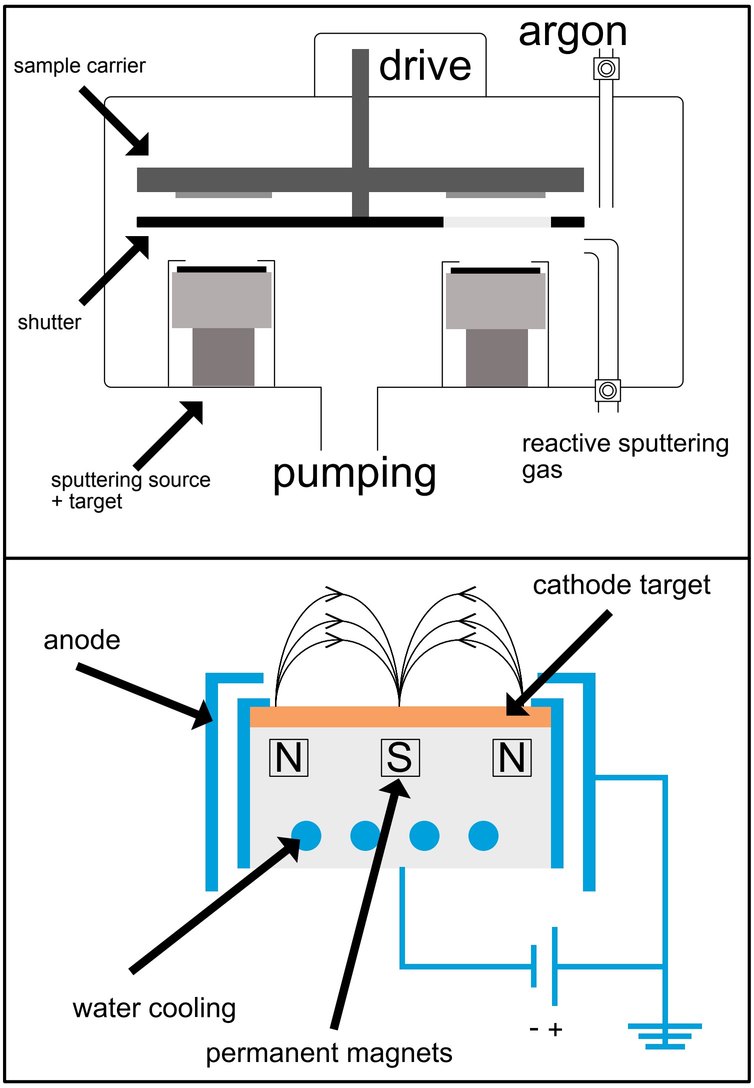

Figure 2.1 – **Top**: Sketch of the inside of the sputtering device comparable with the *Leybold Systems CLAB 600 ClusterTool* work. Two sources being displayed. **Bottom**: Sketch of a single magnetron sputtering source.

High frequency sputtering

Insulating targets (in this work MgO of the tunneling barrier and Ta_2O_5 of the poisoned target) cannot be sputtered using a dc-source because the ions bombarding the surface of the target would stay in place and start charging it. When applying rf power to the target, positive ions and negative ions both hit the target. An rf-field provides enough energy for the electrons to keep the plasma due to collisions. The mass of the electrons is lower in comparison to the ions, resulting in a higher mobility. This is why more electrons reach the target resulting in a positive charge, attracting the ions for sputtering the target. The typical frequencies used ranges from 0.5 to 30 MHz. The most used one is 13.56 MHz [22].

Reactive sputtering

DC magnetron sputtering is an effective way of depositing metallic films. In contrast to that composites or insulating thin films can be prepared by reactive sputtering. In this case the gas in the sputtering chamber is a mixture of the noble gas used for the sputtering and a reactive gas. The plasma itself becomes a chemical active medium. The plasma of the reactive gas and the atoms of the sputtered target bind into composites. The target undergoes the same chemical bindings which is called “poisoning”. This is an undesired aspect in the sputtering process and results in the requirement of a radio frequency source because the surface of the target is insulating. In this work tantalum oxide (Ta_2O_5) is used during the patterning of the TMR junctions.

LEYBOLD sputtering

The samples used in this project are prepared in a *Leybold Systems CLAB 600 ClusterTool* sputtering system. This sputtering device is equipped with seven sputtering sources. Five of these sources are 4” DC magnetron sputter sources, one is 4” RF and one 2” DC. The base pressure is $2 \cdot 10^{-7}$ mbar. During the sputtering process no heat treatment is performed. The sputtering conditions and parameters are shown in table 2.1.

material	mode	power / W	diameter / in	rate / nm/s
$Mn_{83}Ir_{17}$	DC	115	4	0.535
MgO	RF	115	4	0.0156
Ta	DC	65	3	0.185
$Co_{70}Fe_{30}$	DC	115	4	0.262
Ru	DC	115 / 30	4	0.313/0.0756
$Co_{40}Fe_{40}B_{20}$	DC	115	4	0.218

Table 2.1 – *Leybold Systems CLAB 600 ClusterTool* sputtering parameters used for deposition. The sputtering rates may vary depending on the target used and its age.

After installing the sputtering targets, a pre sputtering is performed to remove a possible oxidation layer and clean the targets. The pre sputtering time of the DC targets is 45 min, the RF target for 90 min. The reason of the longer time is the much smaller sputtering rate, compared to the DC targets. The purity of the MgO target is of extraordinary importance to produce high quality tunneling barriers. The sputtering rates of one element/alloy vary depending on the target used and the time.

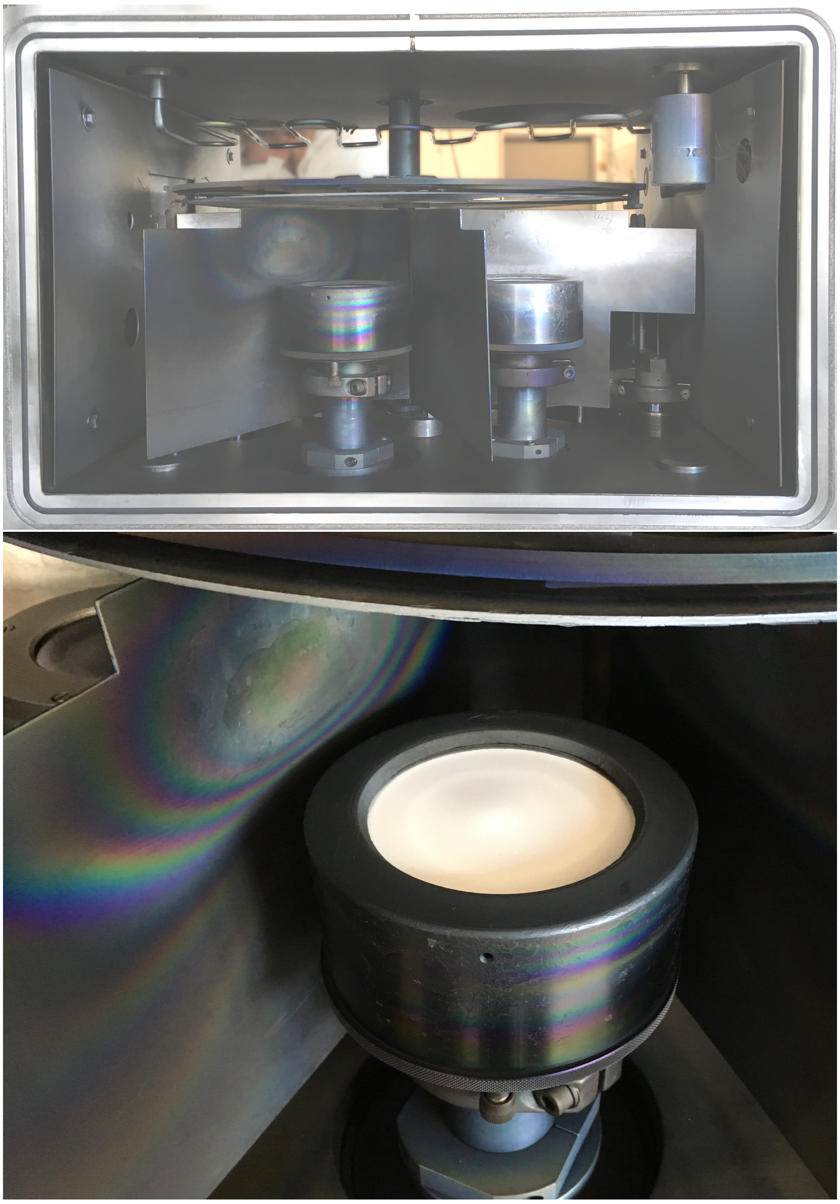

Figure 2.2 – **Top:** Side view of the opened Leybold sputtering chamber. Two sputtering sources can be observed. Above the targets the sample carrier and shutter are attached. **Bottom:** Close-up view of one of the sputtering sources (RF) with an MgO target installed. On the left shielding to the next source an interference pattern of sputtered MgO can be observed. The shape of the pattern reflects the plasma shape, indicating a high reversal point of the magnetic field which results in high quality MgO layers.

The sputtering rates are determined by creating samples with a thickness of approximately 30 nm. On these samples *X-ray reflectivity* (XRR) measurements are performed in order to determine the exact thickness [92]. The technique of XRR is described in Chap. 2.6. The sputtering rate is calculated from the determined thickness and sputtering time.

When exposed to atmosphere, some of the materials will oxidize. Because of this a 2 nm ruthenium layer is sputtered on top in order to avoid oxidation and get exact results for the specimen thickness.

2.2 Field annealing

After the sputter deposition of the different layers, the samples are treated by an ex situ field annealing process. This annealing process accomplished different objectives: First the crystallization of the layers of the tunnel junction and second activating the exchange bias through a field cooling process.

The setup for the field annealing process was constructed at the *University of Bielefeld* by the group of *Thin Films & Physics of Nanostructures*. A copper block can be heated by a heating coil up to 550 °C. The samples are attached to it via tungsten clamps, assuring a good thermal contact. The useable area of the copper block is approximately $30 \times 30\,\text{mm}^2$. This is the limit in terms of maximum sample size. To minimize the oxidation of the specimen during the annealing process, the chamber can be evacuated to a pressure of $1.8 \cdot 10^{-8}$ mbar. The temperature is measured via a thermocouple in the copper block and not directly on the sample. This is why the measured temperature may slightly deviate from the sample temperature. The relative change of temperature during a heating series is reliable, while the absolute value may vary. During the annealing process it is possible to apply an external magnetic field with a permanent magnet (field strength of 5500 Oe) in order to induce a field cooling and activate the exchange bias. The angle between the sample and external magnetic field is defined by the orientation of the samples on the copper block. A rotation during the annealing is not possible.

Figure 2.3 – Setup for annealing and pinning. The copper block in the front has a useable dimension of approximately $30 \times 30\,\mathrm{mm}^2$. The samples are fixed with metal clamps for a good thermal coupling. The chamber is evacuated to $1 \cdot 10^{-8}\,\mathrm{mbar}$. The external magnetic field has a field strength of 5500 Oe.

2.3 Patterning of TMR stacks

For measurements of the electric resistance it is necessary to pattern the two-dimensional layer system into elements of a well defined geometry. There are different ways of performing the patterning which are distinguished by the choice of the photo resist that is used and how it is exposed. Common ways are via electrons (e-beam lithography), lasers or UV light. These approaches have different advantages and drawbacks which are mostly correlated to minimum attainable structure width and time that is consumed during the exposure. For this work UV lithography is used because the average structure width is in the range of $10 - 50\,\mu\mathrm{m}$ and it allows a high throughput in TMR stack production. The different steps are shown in Fig. 2.4. More details are given below.

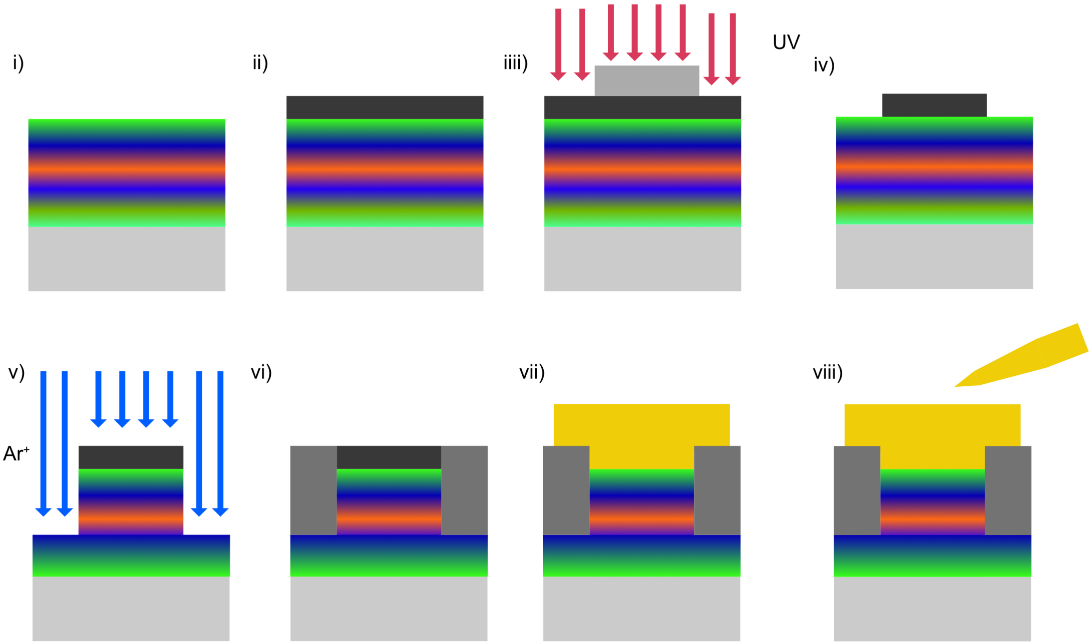

Figure 2.4 – Sketch of the different stages of the patterning process. i) After the sputtering process the complete substrate is covered with the layer system. ii) Photoresist is applied via a spincoater to achieve a well defined resist thickness iii) Exposure to light under a mask. iv) Positive resist is developed and removed v) Ion etching to remove non coated layers. vi) sputtering of insulator Ta_2O_5 to prevent short-circuits while during electric measurements. vii) Gold contact pads from a second lithography step for physical protection and more comfortable electric contacts. viii) contacting via gold needles on top and bottom for electric measurements.

Photoresist

The first step of patterning is applying the photoresist on the sample by spin coating. The thickness of the resist is given by the rotation speed and time. There are two categories of resist: positive and negative. Since in this work positive resist is used and in volume production the usage of positive resist is dominant, the description is focussed on positive resist.

A 1 µm thick layer of resist is achieved by spincoating for 60 s at a rotation speed of 4000 rpm. The resist consists of a large amount of dissolver, resulting in a relatively soft consistency. Therefore a thermal treatment on a hot plate for 4 min at 100 °C is conducted.

The mask has a size of $1 \times 1\,\mathrm{cm}^2$. TMR junctions[1] of a size of $7.5 \times 7.5\,\mu\mathrm{m}^2$ (343), $12.5 \times 12.5\,\mu\mathrm{m}^2$ (196) and $22.5 \times 22.5\,\mu\mathrm{m}^2$ (196) are made. The mask is directly put onto the resist (contact exposure). There are several advantages and disadvantages of contact exposure. The setups are cheap and complete wafer can be exposed at a time. The direct contact mode leads to a contamination of the mask over time. Particles remain on the mask and can be transferred

---

[1] Numbers in parentheses are the amount of tunnel junctions

to the resist. Defects and scratches in the resist lead to a high defect density, reducing the sample yield. For patterning the TMR junctions the positive resist $AR-P\,5350$ (Manufacturer: Allresist) is used.

A short process flow for applying the photoresist is described below:

- spin coating for 60 s at a rotational speed of 4000 rpm, leading to a thickness of approx. 1 µm
- annealing at 100 °C for 4 min
- exposure with UV light
- development in $AR\,300-35$ (1 : 2 with water) for 60 s

Ion etching

The second step is removing the non coated areas by ion etching. The tool for the etching is performed at a tool build at the *University of Bielefeld* in the group of *Thin Films & Physics of Nanostructures* . At an argon pressure of $2.4 \cdot 10^{-5}$ mbar several layers of the specimen are removed under an angle of 30 ° while rotating to avoid shadowing effects. During the complete process a quadrupole mass spectrometer detects, which layers are currently removed. A typical mass spectrum of a TMR stack with two artificial antiferromagnets during an etching process is shown in Fig. 2.5.

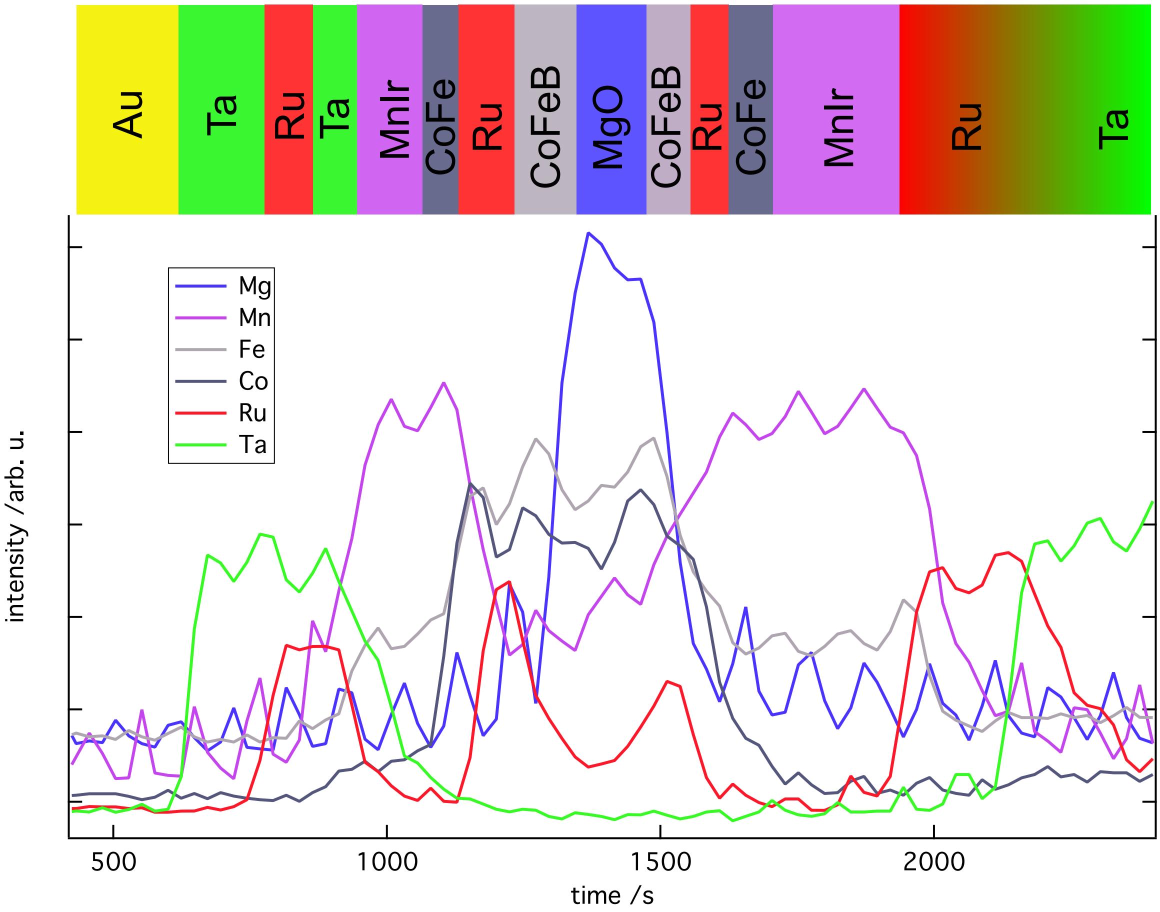

Figure 2.5 – Typical secondary ion mass spectrum during the ion etching process of a double pinned TMR stack. Six different masses are detected, corresponding to the most important elements of the TMR stack.

The sample shown in the mass spectrometry measurement does not have contact pads with a bigger surface area for easier contacting. Before the lithography tantalum (10 nm) and gold (80 nm) have been sputtered on the specimen. Contacting the individual TMR element is more sophisticated but only one lithography step is required. This is why no signal can be observed in the first 550 s during the ion etching. In this time the gold layer is removed. The two upper tantalum layers cannot be distinguished even with the two nanometer thick ruthenium layer in between. The detection of mass spectrometer gives a clear signal of the current layer as seen on the two ruthenium interlayers of the artificial antiferromagnets at a time of 1200 s and 1500 s. They have a thickness of 2.0 nm and 0.9 nm with a clear difference in the signal. The etching is stopped at the 10 nm-tantalum layer above the 30 nm-ruthenium which is the bottom electric contact.

The variation of the etching rate, which can be observed the thicker layers as the 20 nm-$Mn_{83}Ir_{17}$ of the bottom artificial antiferromagnet can be explained by the rotation of the sample during the etching process. If the mass spectrometer is not perfectly aligned to the center of the sample the detection rate varies with the rotation of the sample.

Insulator and contact pads

In theory it is now possible to perform resistive measurements on the individual TMR junctions. In reality this is not the case since a short-circuit is likely during the contacting. This is why after the ion etching and before the lift off further sputtering steps are performed.

The first one is filling up the gaps between the different TMR stacks with insulating Ta_2O_5. It is deposited by reactive RF sputtering in an argon/oxygen atmosphere. With a sputtering rate of 1 nm/s after two hours a thick insulating layer is fabricated to prevent any short-circuits. The lift off is done in an ultrasonic bath in N-Methyl-2-pyrrolidone (NMP). Tantalum (10 nm)/Gold (80 nm) pads for an easier contact with gold needles and a higher resistance during the mechanical contact and a size of approximately 3000 μm^2 can be prepared in a second lithography step.

2.4 Electric measurements on TMR stacks

The setup for TMR measurements is shown in Fig. 2.6. The samples are placed on a plastic block (2) in order to have electric isolation, the sample is positioned in the height of the iron cores of the electromagnet (1) which provides a magnetic field up to 3300 Oe along one axis. The magnetic field is measured with a Bell 6010 Gauss-/Teslameter (5). The electric contact is realized via gold needles which can be mounted (3) to four (4) 3-axis micrometer stages. The stages lead to a transimpedance amplifier. The amplifier converts the current through the tunnel junction into a voltage with different amplifications (up to 10^6). Two different measurement modes of TMR and I/V are performed with this setup.

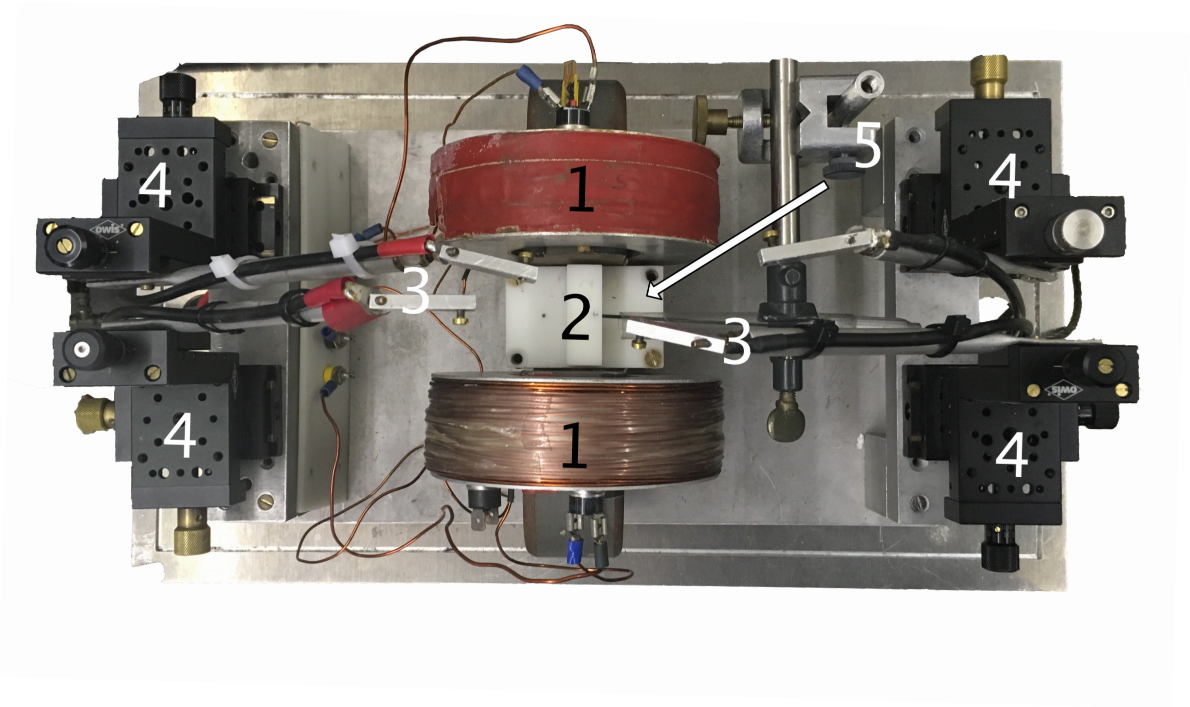

Figure 2.6 – Setup for the electric transport measurements. 1) magnetic coils providing up to 3300 Oe. 2) sample position 3) Hall probe 4) Four non magnetic 3 axis micrometer stage with pickup for gold needles. The four needles are connected to a transimpedance amplifier. Currents are measured with a Keithley 2000 multimeter after the amplifier, the field by a 5) Bell 6010 Gauss-/Teslameter

TMR

A constant bias voltage in the range of $10-20\,\mathrm{mV}$ is applied to the sample. The external magnetic field is controlled by the electromagnet . The electric resistance has an exponential dependence with respect to the barrier thickness of a TMR junction [47]. This is why it is important that the amplification of the converter has suitable sensitivity of measuring ranges.

I/V

This mode is a pure electric resistance measurement without any magnetic field involved. Due to the non-ohmic-behavior of a tunnel junction, the current is not directly proportional to the applied voltage. From the I/V curve (or $\partial I/\partial V$) it is possible to extract information about the tunneling barrier [10].

2.5 MOKE setup

The MOKE measurements were performed by a setup built at the *University of Bielefeld* in the group of *Thin Films & Physics of Nanostructures*.

The light is provided by a laser diode (wavelength $\lambda = 650\,\mathrm{nm}$). After a first linear polarizer the light is reflected on a sample which is in between two pole shoes of an electromagnet. The magnet provides a magnetic field strength up to 20 000 Oe, depending on the pole shoe distance. The minimum distance is given by the sample holder of 20 mm. The maximum distance of the pole shoes is 45 mm which is also the restriction of the samples size. At this position of the magnet, the highest field which can be achieved is approximately 11 000 Oe.

The focus of the laser is adjusted to be between the sample and detector, as a result the data collected is an average over an area of approximately $0.8\,\mathrm{mm}^2$.

After the reflection under an angle of 13° with respect to the samples surface normal, the light passes a second linear polarizer which is rotated by 90° and is detected by a photodiode before the signal is read out by a Keithley 2000 multimeter. A lowpass filter removes most of the low frequency noise.

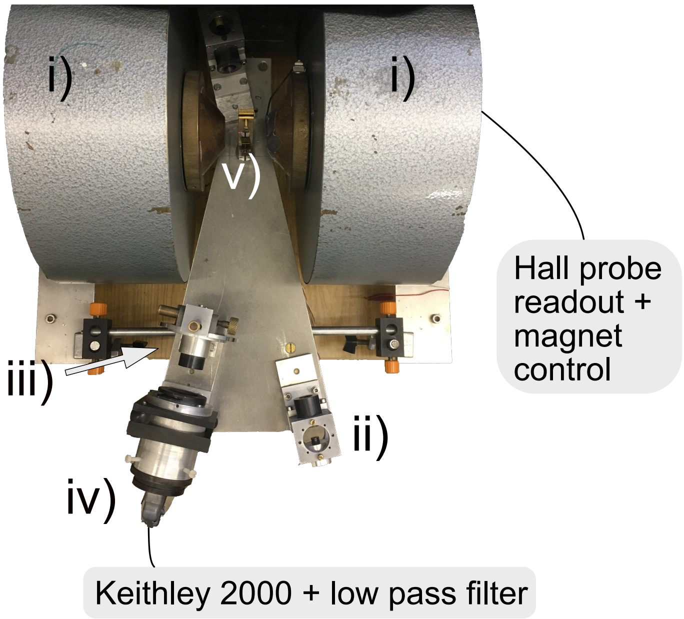

Figure 2.7 – Setup for the MOKE measurements. i) The electromagnet providing at magnetic field up to 20 kOe ii) laser diode ($650\,nm$) with a linear polarizer iii) second polarizer iv) photo diode detector with a band pass filter for the laser wavelength. The diode is read out by a $Keithley$ 2000 with an external low pass filter.

2.6 XRD / XRR

The properties of the prepared thin films depend, among other things, on its thickness and the crystallographic orientation. X-ray diffractometry and X-ray reflectometry have been used to study these structures. The advantages of these methods are non-destructiveness of the samples and reproducibility of the measurements.

Both techniques are performed in the same *Philips X'pert Pro MPD* diffractometer. The tool is equipped with a copper anode, providing X-rays of a wavelength of $\lambda = 1.54\,\text{Å}$. Since these methods are a not very extensive used in this work, the presentation of the basics is not very detailed and reduced to a basic level. A deeper description can be found elsewhere [104, 106].

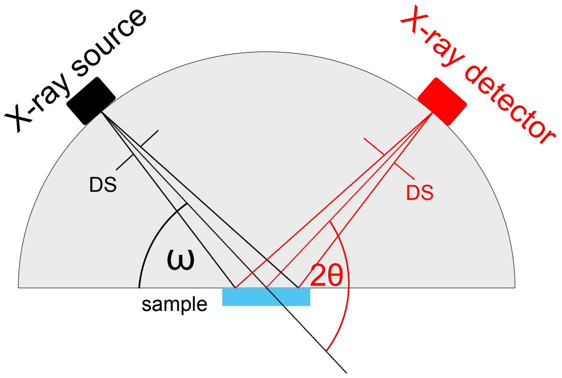

Figure 2.8 – Sketch of the Philips X'pert Pro MPD diffractometer in the Bragg Brentano geometry. Shown in black the incident x-Rays and the reflected ones in red.

XRD

XRD measurements are interference experiments. The specimen is irradiated with X-rays and these perform interference when they are reflected at different crystal planes. The intensity of the reflected X-rays is measured with respect to the incidence angle. If the relation $\omega = \theta$ (see Fig. 2.8) is met, the Bragg equation explains when a maximum in the interference pattern can be observed:

$$n\lambda = 2d_{hkl}sin(\theta) \tag{2.1}$$

n is an integer number, d_{hkl} the inter planar spacing in the direction $[hkl]$ with the Miller indeces (hkl) and λ the wavelength of the incidence X-rays.

During an XRD measurement the sample is illuminated with X-rays while the X-ray source and detector are moving in the Bragg Bentano geometry ($\omega = \theta$, see Fig. 2.8). The automatic divergence slit (DS) and anti-scatter slit (ASS) assure that always a constant area is irradiated which leads to a high signal to noise ratio.

XRR

XRR is a tool to measure the thickness of a thin film with a thickness in the range of $3-300\,\text{nm}$. Information on the roughness and density can be extracted as well. The sample is irradiated under a small angle ($0^\circ < \theta < 5^\circ$). If the angle is bigger than the critical angle, interference will take place and produce so called Kiessig fringes. This critical angle is associated with the square root of the density of the material.

The thickness can be derived from the periodicity of the oscillation:

$$d \propto \frac{\lambda}{2} \frac{1}{\theta_{m+1} - \theta_m} \tag{2.2}$$

A typical XRR measurement is shown in Fig. 2.9. The data of the green curve contains the information of two layers. The deposited $Co_{40}Fe_{40}B_{20}$ layer of a thicknees of approximately 30 nm and a second thinner layer. This second layer is formed by oxidation. It is modelled by a 6 nm thick oxide (Fe_2O_3).

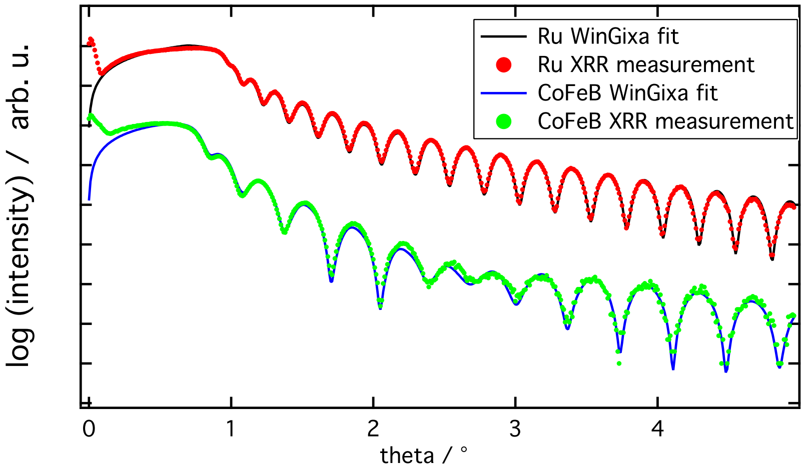

Figure 2.9 – Two XRR measurements with their corresponding fits based on a Parrat algorithm. Ru and $Co_{40}Fe_{40}B_{20}$ have been investigated in oder to determine the film thickness. The $Co_{40}Fe_{40}B_{20}$ sample does contain more than one layer. An oxide (Fe_2O_3) is also taken into account.

A Fourier transformation gives a first estimate of the thickness. A following fit to the measured data with a *Parratt* algorithm is used to obtain detailed information about the sample.

2.7 Transmission electron microscopy

X-ray diffraction analysis gives information on the crystal structure of a large area.

In a system as complex as a double pinned magnetic tunnel junction with repeating materials and alloys, a simple XRD measurement is not sufficient to investigate on the crystal structure of single layers. The required spatial resolution below the nanometer scale is given by a *transmission electron microscope* (TEM). The diffraction pattern of a specific layer gives information on the crystallographic order, lattice parameters or the orientation of single grains [123].

In this work a JEM 2200 FS microscope manufactured by JEOL is used. It accelerates electrons to a kinetic energy of $80-200\,\mathrm{keV}$ from a ZrO/W(100) Schottky emitter. Electrons with such a high energy can transmit through thin samples. A $4k \times 4k$ CMOS camera detects the electrons after scattering events in the sample. The spatial resolution is up to $0.23\,\mathrm{nm}$ at $200\,\mathrm{keV}$.

For this measuring technique thin specimen are required for electron transmission. The target thickness of the sample (in this case called a *lamella* or *cross section*) is on the order of $20\,\mathrm{nm}$. A thicker sample would reduce the resolution of the TEM measurement while a thinner would have a small thermal budget, leading to a bending of the heated sample. The lamellas are cut out of a planar sample by a focussed ion beam (FIB).

The device used is a combination of a scanning electron microscope and a focussed ion beam. A detailed description of the device is given in the PhD thesis of *Dr. Martin Gottschalk* [40]. The setup is comparable to an electron microscope based on gallium ions which can be accelerated on a surface and it is possible to manipulate a specimen with a resolution of $4\,\mathrm{nm}$. A typical FIB prepared lamella has a width of $10\,\mu\mathrm{m}$ and a height of $3-4\,\mu\mathrm{m}$. Two SEM pictures of a mounted lamella of a double pinned TMR junction are shown in Fig. 2.10. The preparation of the FIB lamella is done by *M. Gottschalk*. The TEM measurements are performed by *I. Ennen* and *D. Rahmermann*. The Fourier transformation of the different areas of the TEM picture gives insight on the crystal structure.

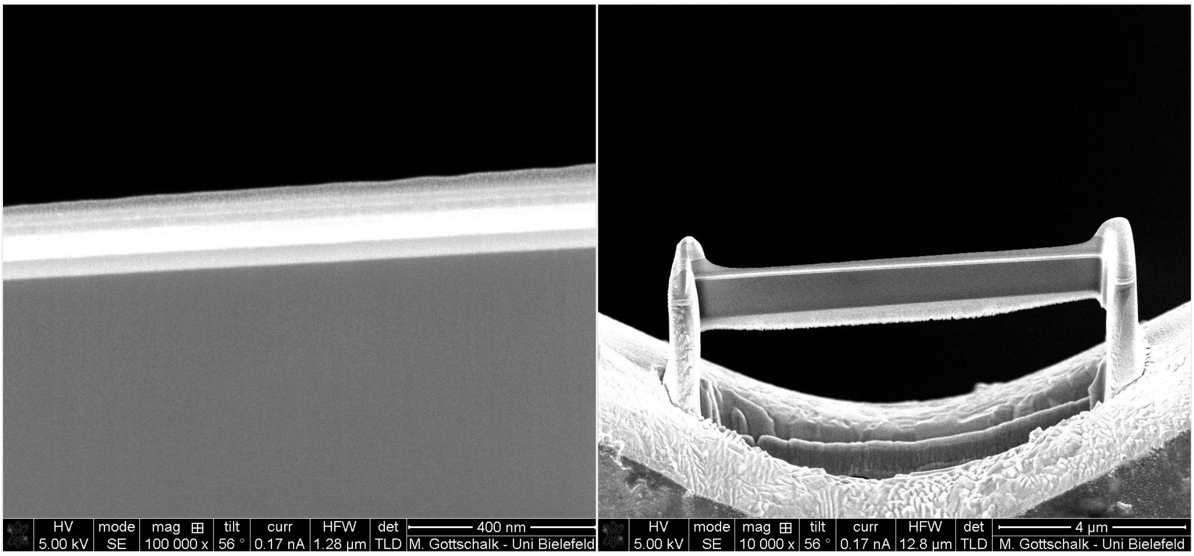

Figure 2.10 – **Left**: Different layers of the TMR junction can be observed. The rough, tapering layer on top is protective platinum, deposited during the lamella preparation. **Right**: Mounted lamella of a double pinned TMR junction prepared for TEM measurements.

2.8 Inverse magnetostrictive measurements

All measurements under mechanical stress have been performed at *Institute for Materials Science, Christian-Albrechts-Universität zu Kiel.* In Kiel a device was constructed which has the possibility to provide an external magnetic field for standard field loops while applying mechanical stress to the specimen.

The samples are placed inside a Bruker electromagnet and the external magnetic field is swept in steps of 5 Oe. The bias voltage applied to the sample is kept at constant 10 mV. The current is converted into a resistance. A four-point bending apparatus is used to apply uniaxial stress to the sample. The stress is controlled by linear actuators. Depending on the sign of the stress, two of the four macor contact points push the silicon wafer. Magnetoresistive measurements are performed under a certain stress or magnetostrictive measurements under a certain external magnetic field. A sketch of the setup is shown in Fig. 2.11

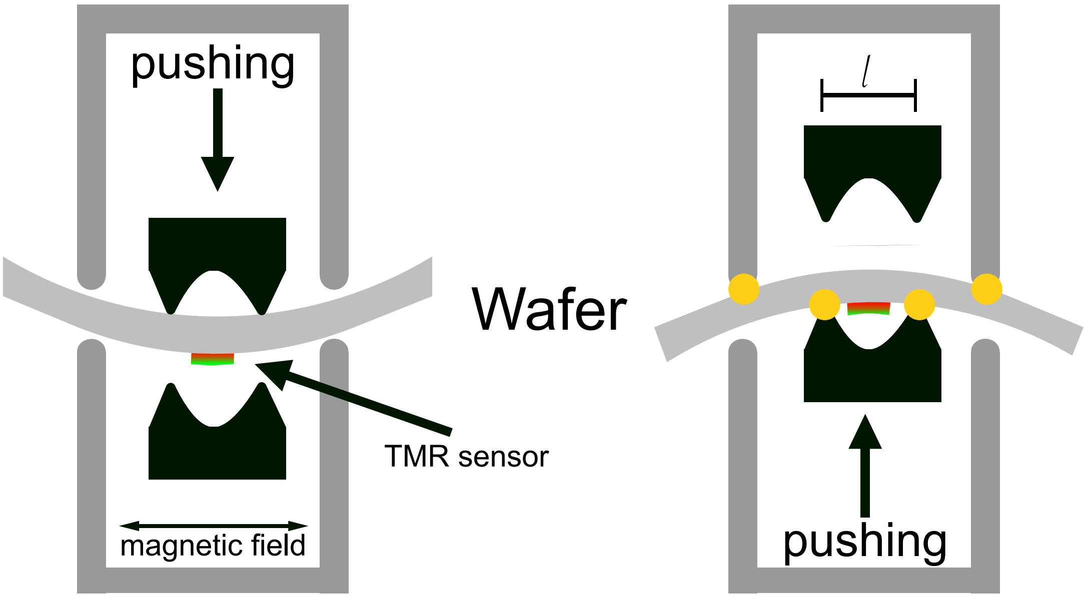

Figure 2.11 – Sketch of the four point bending apparatus used for the strain measurements. The pusher block moves the macor ceramics and can enforce tensile or compressive stress on the TMR sensor.

The origin of the stress is the bending of the silicon. It can be calculated by [109]:

$$\varepsilon = \frac{9t}{2S^2}\left(\Delta z + {}^{t}\!/_{2}\right) \approx 7.64 \times 10^{-3}\Delta z \tag{2.3}$$

The parameters are given by the geometry of the system: $t = 550\,\mu\mathrm{m}$ (thickness of the wafer), $S = 18\,\mathrm{mm}$ (distance outer mechanical contact points) and Δz (pusher block displacement). The maximum displacement is $100\,\mu\mathrm{m}$ resulting in a stress of $0.76 \cdot 10^{-3}$.

2.9 Layers of the TMR stack

Two different variants of double pinned TMR stacks are examined in this work. The layers of the two configurations of a double pinned TMR stack are shown in Fig. 2.12. They are made out of up to 15 different layers with different purposes. This chapter focuses on explaining these functions.

These stacks can be separated in five different parts. It starts with the buffer consisting of the first four layers on the silicon substrate. It is mostly designed by the results of *V. Drewello* in his diploma thesis [29]. The purpose is providing an electric lead as a bottom contact and a suitable crystal structure for the antiferromagnet which is pinning the bottom electrode. The second part of a TMR stack is the pinning of the bottom electrode. This is the main distinctive feature of the two TMR stacks. One is pinned via a natural antiferromagnet whereas on the second one the bottom pinning is by an artificial antiferromagnet. The third component is the tunnel junction consisting of two ferromagnetic $Co_{40}Fe_{40}B_{20}$ layers separated by a thin insulating MgO barrier. After the pinning of the upper electrode with an artificial antiferromagnet the stack is completed by a capping layer preventing oxidation. The pinning of the top electrode has to be realized by an artificial antiferromagnet since $Mn_{83}Ir_{17}$ does not grow in the desired crystal structure for exchange bias.

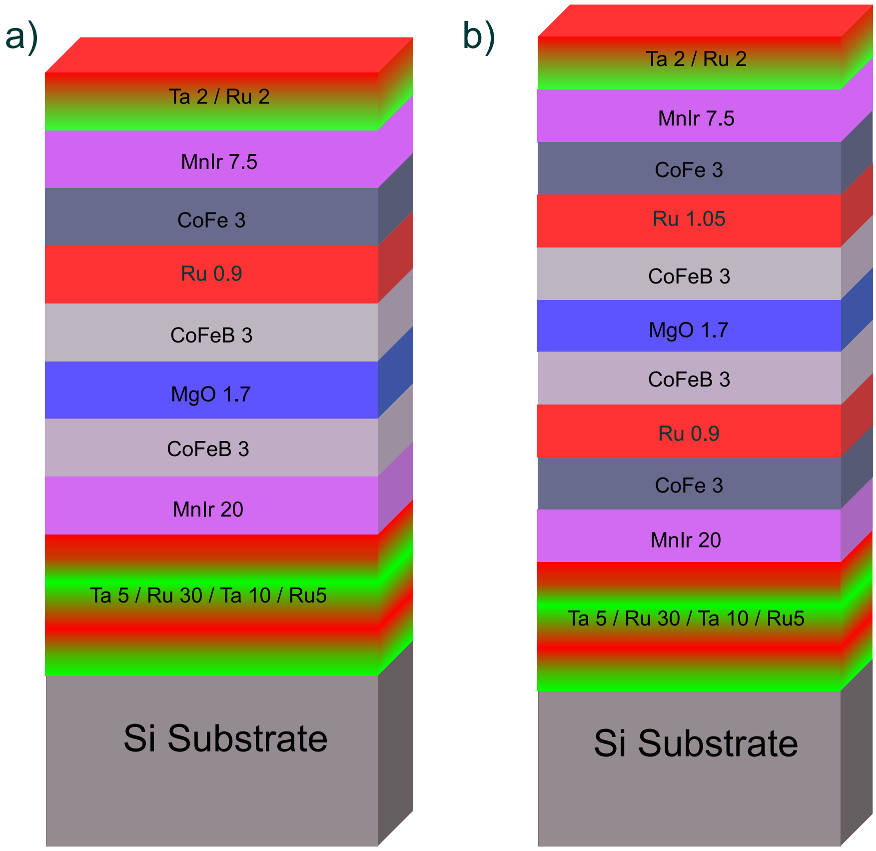

Figure 2.12 – Layers of the two configurations of the double pinned TMR stacks. The difference is the realization of the pinning on the two electrodes. a) Bottom: Natural antiferromagnet $Mn_{83}Ir_{17}$ (20 nm) Top: Artificial antiferromagnet with a natural antiferromagnet $Mn_{83}Ir_{17}$ (7.5 nm) and a Ru interlayer of 0.9 nm. b) Two artificial antiferromagnets: Bottom $Mn_{83}Ir_{17}$ 20 nm and 0.9 nm Ru Top: 7.5 nm $Mn_{83}Ir_{17}$ and 1.05 nm Ru.

Buffer

The substrate is (100) oriented silicon wafer with a $50\,\mathrm{nm}$ thermal oxide layer and a total thickness of $525 \pm 20\,\mu m$ (Manufacturer: Siegert Wafer). Before preparing the functional layers of the TMR stack, an underlayer buffer is deposited. The buffer has different purposes.

First, it has to provide the bottom electric contact for the two point resistance measurements. Second it has to provide a crystal structure and roughness which is suitable for growing antiferromagnetic materials and tunnel junctions on top.

Tunnel barriers of magnetic tunnel junctions have a typical thickness of $1-2\,\mathrm{nm}$. With increasing roughness, the probability of pinholes in the barrier increase rapidly which would act as short-circuits.

The crystal structure of the antiferromagnets has a strong influence on their magnetic properties. This crystallographic structure is influence by the underlaying layers. Different materials are suitable buffers for $Mn_{83}Ir_{17}$, in this case ruthenium is used for this purpose. The layers of the buffer are (thicknesses given in nm):

$$Ta5/Ru30/Ta10/Ru5$$

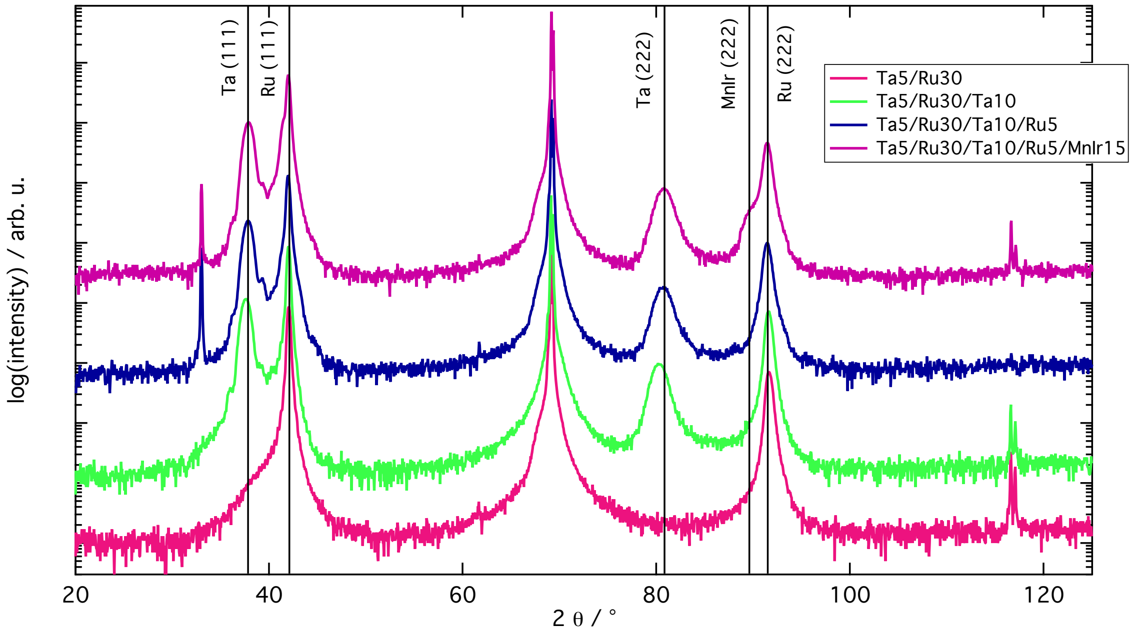

Figure 2.13 – XRD measurements of different samples with an increasing number of layers of the buffer used for the TMR stacks. All samples have been sputtered at room temperature and no additional heat treatment after the sputtering process was performed. The lowest ruthenium layer is the first one growing in the (111) direction which is important for the $Mn_{83}Ir_{17}$ on top in order to induce an exchange bias.

In future descriptions of layer orders, the term “Buffer” will be used as an abbreviation for these four layers. XRD measurements of different stages of the buffer are displayed in Fig. 2.13. The measurement with 5 nm of tantalum on the substrate is excluded since it does not show any peaks other than the substrate peak at a 2θ angle of 69.138 °. The first tantalum layer grows amorphous on the substrate but is a good underlayer for the ruthenium (30 nm) on top. As seen in the red curve of Fig. 2.13, the ruthenium (which also provides the bottom electric contact) grows in the desired (111) direction. The third layer deposited (tantalum, 10 nm, green curve) is (111) oriented. The main purpose of this tantalum layer is not providing the optimum crystal structure, but being a stopping layer for the ion etching process of the final TMR element in a later step. When comparing the measurement of the complete buffer (blue) and the buffer with the antiferromagnet $Mn_{83}Ir_{17}$ on top (purple) a new shoulder on the low angle side of the ruthenium (111) and (222) peak can be discovered. This XRD peak is associated with the [111] direction of the $Mn_{83}Ir_{17}$, which is necessary for exchange bias [35, 57].

Tunnel junction

The tunnel junction is the central element of a TMR stack. As described in Chap. 1.5 and 1.6 it consists of two magnetic layers ($Co_{40}Fe_{40}B_{20}$) separated by an insulator (MgO). Several parameters of the tunneling barrier can be extracted from the current-voltage characteristic. A typical measurement is shown in Fig. 2.14

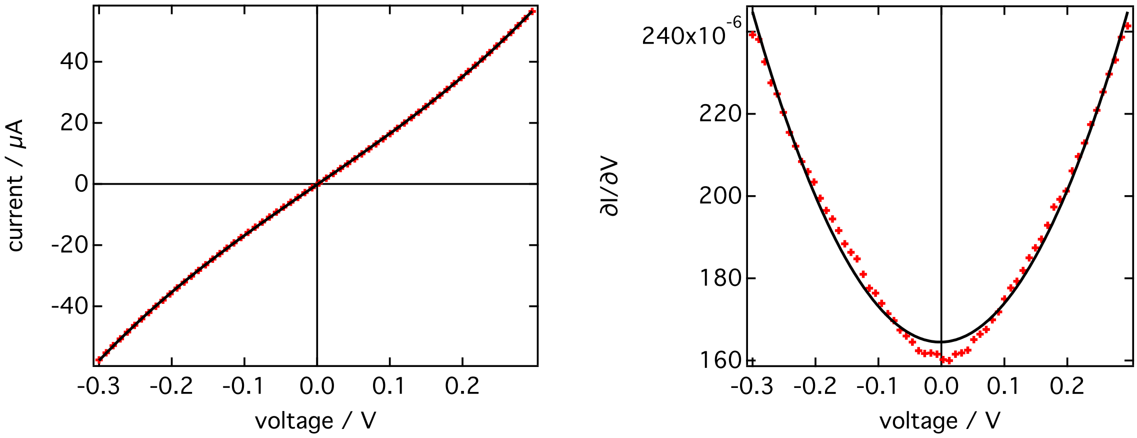

Figure 2.14 – **Left**: Current voltage characteristic of a TMR stack. The measured data (red) is in perfect accordance with the polynomial fit. **Right**: Derivative of the current with respect to the voltage. The parabola shape increases the recognizability for the human eye.

On the left side the directly measured I/V curve (red) is displayed. In addition a third degree polynomial fit (black) shows a good agreement with the measured data. On the right side the derivative of the current with respect to the voltage ($^{dI}/_{dV}$) is presented together with a parabolic fit.

In the case of a damaged tunneling barrier a linear relation in accordance with Ohms law between current and voltage would be expected. Consequently the derivative would be a constant. While on the left side the accordance with a fit of a polynomial to the power of three cannot be seen easily with the bare eye, on the right side a constant line would be shown if the barrier would be damaged. Without going into the details of the parameters of the current-voltage characteristic the parabolic shape of the derivative is a strong indicator of an intact barrier.

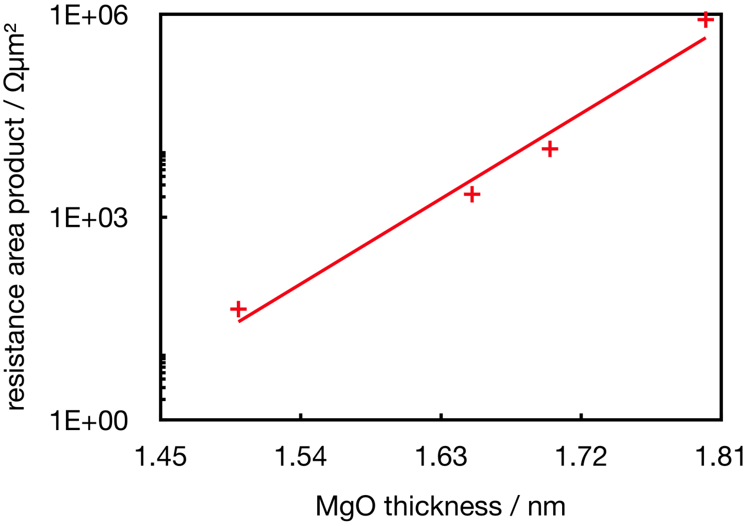

Figure 2.15 – Exponential dependency of the area resistance product of a tunnel junction with respect to the thickness of the tunneling barrier. The exponential fit (result in a straight line on an exponential axis) is only a guide for the eye.

The resistance of a tunnel junction is dominated by the thickness of the tunneling barrier . As seen in Eq. 1.27, the tunneling probability has an exponential relation with the barrier thickness [47]. As a result, the resistance of the tunnel junction has the same dependency. Fig. 2.15 illustrates this relationship. The parameters of the exponential fit are not used in this work but give a guide for the eye.

Artificial antiferromagnets

Pinning an electrode of a tunnel junction with a natural antiferromagnet has a limit in terms of exchange bias. These limits can be overcome by using an *artificial antiferromagnet* (AAFM) [53, 93]. For a pinning with an artificial antiferromagnet at least four layers are required.

A natural antiferromagnet ($Mn_{83}Ir_{17}$) is pinning a ferromagnetic layer ($Co_{70}Fe_{30}$). This combination is known for a high exchange bias and blocking temperature [36]. A thin layer of ruthenium is separating the $Co_{70}Fe_{30}$ layer from the second ferromagnetic layer ($Co_{40}Fe_{40}B_{20}$). An *interlayer exchange coupling* (IEC) between the two ferromagnetic layers is induced as described in Chap. 1.4. Ruthenium is used as a standard spacer material as it leads to a higher IEC compared to Cu [91].

The magnetic bias applied to the $Co_{40}Fe_{40}B_{20}$ layer is now defined by the interlayer coupling and not the exchange bias of the $Mn_{83}Ir_{17}$ layer. As seen in in Chap. 3.1.1, the exchange bias induced to a 5 nm $Co_{40}Fe_{40}B_{20}$ layer has a maximum value of approximately 400 Oe . The results of the investigation on the interlayer exchange coupling strength are shown in Chap. 3.3. The top ($Co_{40}Fe_{40}B_{20}$/Ru/$Co_{70}Fe_{30}$/$Mn_{83}Ir_{17}$) and bottom ($Mn_{83}Ir_{17}$/$Co_{70}Fe_{30}$/Ru/$Co_{40}Fe_{40}B_{20}$) electrode of a magnetic tunnel junction can be pinned with an artificial antiferromagnet.

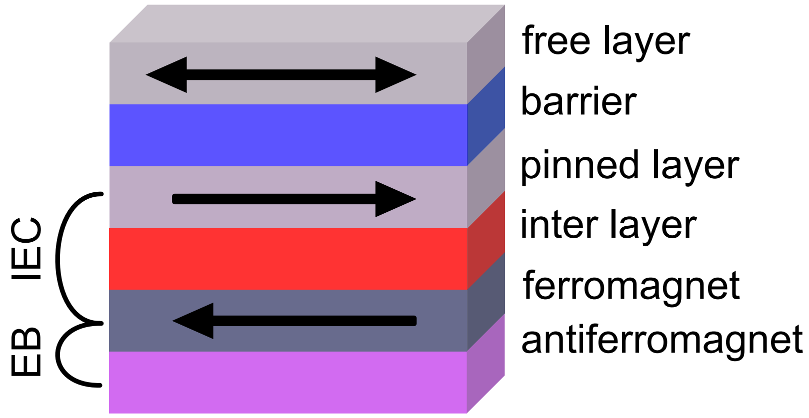

Figure 2.16 – Concept of pinning the bottom electrode of a tunnel junction with an artificial antiferromagnet. A ferromagnet ($Co_{70}Fe_{30}$) is pinned by a natural antiferromagnet ($Mn_{83}Ir_{17}$) via the exchange bias (EB). Through a thin interlayer an interlayer exchange bias (IEC) is induced, pinning an electrode ($Co_{40}Fe_{40}B_{20}$) of a tunnel junction.

2.10 Rotation of the exchange bias direction

In this work samples undergo several consecutive annealing steps in an external magnetic field in different directions. As described in Chap. 1.3 the blocking temperature of an antiferromagnetic layer depends, among other conditions, on its thickness. Thus, different blocking temperatures can be achieved by choosing different thicknesses of the antiferromagnetic layers.

After a first annealing step, as outlined in Chap. 2.2, both magnetizations of the electrodes are collinear. They are parallel or antiparallel aligned based on the sign of the exchange interaction. The direction of the magnetic field of the first annealing step is called direction A.

A second annealing step with the magnetic field direction rotated by 90 °, with respect to direction A in the sample plane has the goal to rotate the direction of the exchange bias of one of the electrodes. This direction is called direction B.

The temperature of the second annealing step has to be chosen to be high enough to rotate the pinning direction of the ferromagnetic layer pinned with the thin antiferromagnet, but not to influence the pinning direction of the second electrode. The concept of this process is shown in Fig. 2.17. The results of the blocking temperature investigations are described in Chap. 3.1.2.

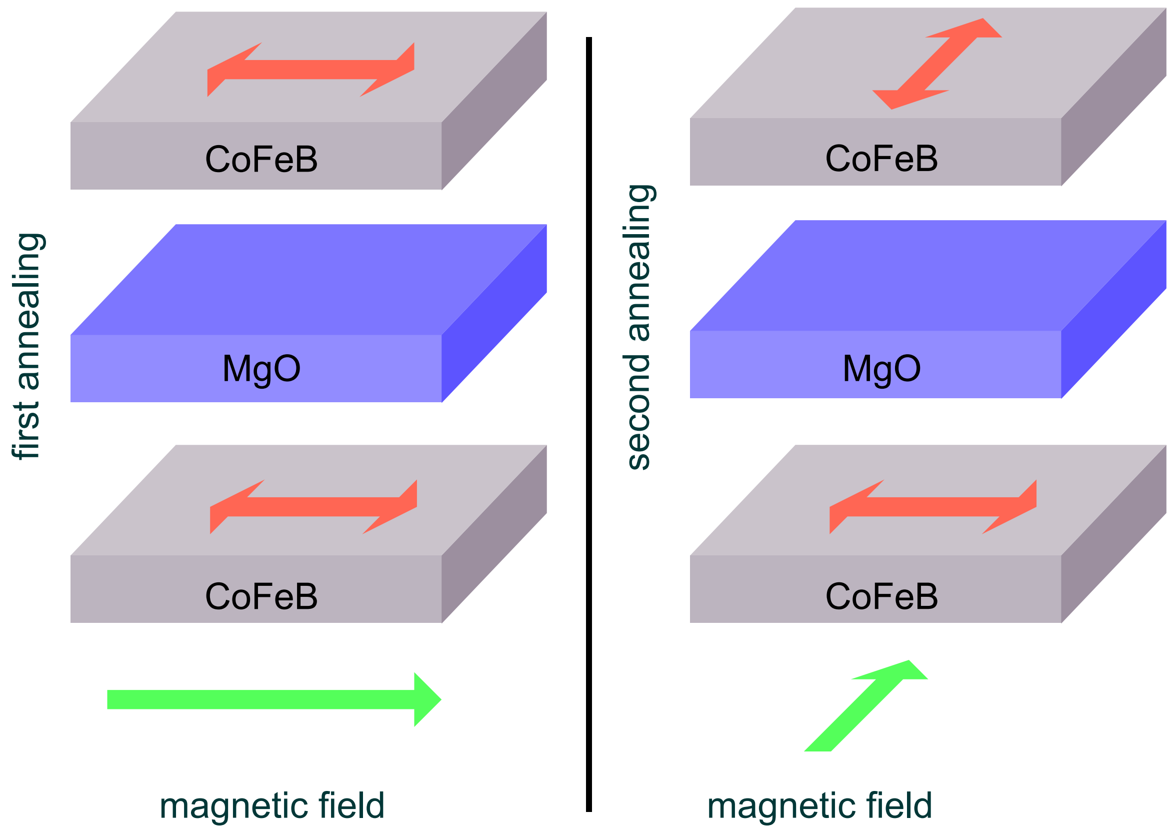

Figure 2.17 – CoFeB/MgO/CoFeB tunnel junction of the TMR stack used as a stress sensor. Green arrows indicate the direction of the magnetic field during an annealing process. Red arrows show the direction of the pinning induced by a natural or artificial antiferromagnet. After the first annealing step, both magnetizations point along the same axis. In the second annealing step, one of the magnetizations is rotated in a perpendicular direction. The result is a non collinear magnetic ground state.

Magnetization directions in double pinned TMR stacks

The two configurations of the used double pinned TMR are shown in Fig. 2.12. At first the magnetization directions of the electrodes in the system with a natural and an artificial antiferromagnet will be discussed.

As discussed in Chap. 1.3 the unidirectional anisotropy induced via exchange bias is antiparallel with respect to the field direction during the field cooling process. The interlayer exchange coupling constant in the artificial antiferromagnet is negative. As a result, the magnetizations of the two electrodes are collinear but antiparallel, as shown in Fig. 2.18a.

For the next annealing step the magnetic field is rotated by 90 ° counterclockwise in the sample plane. The magnetization of the upper $\mathrm{Co_{40}Fe_{40}B_{20}}$ layer again aligns with the external magnetic field. The rotation of the pinning of the bottom electrode is clockwise since it aligns antiparallel with an external magnetic field. Because of the higher blocking temperature the angular change is small. The final magnetic ground state is shown in Fig. 2.18b.

The second design has different magnetization directions. Artificial antiferromagnets are used for the pinning of both electrodes. As described in Chap. 1.4 the magnitude of the coupling constant and its sign is a function of the thickness of the ruthenium interlayer . The reference layer has to be as magnetically hard as possible. This is why a thickness of 0.9 nm is chosen, leading to an antiferromagnetic coupling at the first extremum [90]. The ruthenium interlayer of the artificial antiferromagnet of the sensing layer is chosen to result in a weak pinning. The sign of the coupling constant of the interlayer exchange coupling can be set by the interlayer thickness. Below the case of a negative coupling constant is discussed.

After the first annealing steps both magnetizations align with the magnetic field in direction A. After the second annealing the magnetization direction of the weakly pinned sense layer will align with the magnetic field (direction B) again. The resulting angles α and θ as seen in Fig. depend of the blocking temperature of the two antiferromagnetic layers, as seen in Fig. 2.18

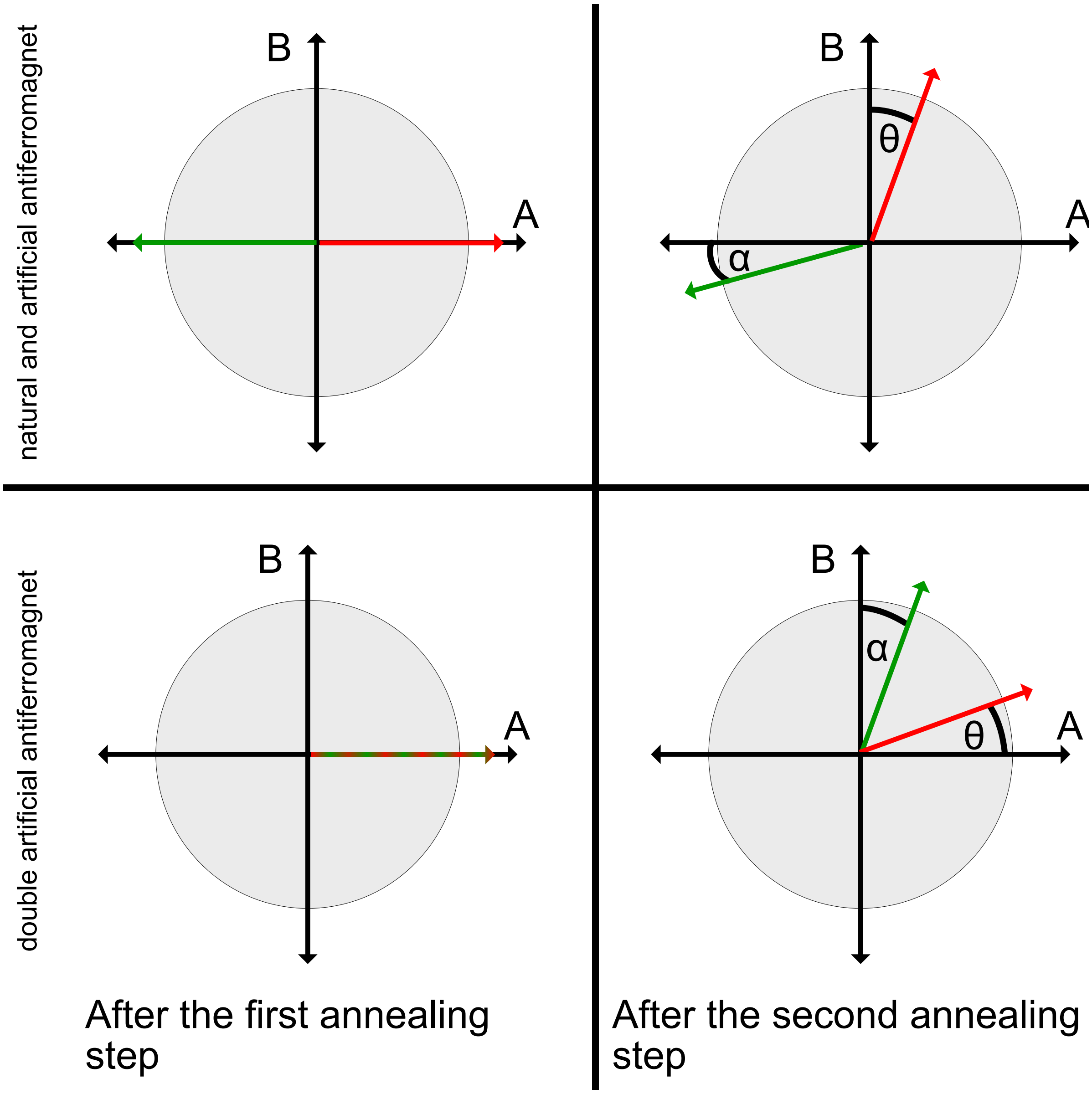

Figure 2.18 – Directions of the magnetizations of the two the electrodes after the first and second annealing. After the first annealing step both of the magnetizations align collinear with the A axis. If it aligns parallel or antiparallel depends on the sign of the coupling constant of the pinning system. The angles α and θ are functions of the temperatures of the second annealing step with respect to the blocking temperature of the corresponding antiferromagnets. In green is shown sense layer in the final system, the reference layer is displayed in red.

Chapter 3

Results and discussion

The first part of this chapter focusses on the investigation of the exchange bias and blocking temperature of the natural antiferromagnet $Mn_{83}Ir_{17}$.

$Mn_{83}Ir_{17}$ is used either for pinning an electrode of the tunnel junction or part as an artificial antiferromagnet.

The top electrode cannot be directly pinned by a $Mn_{83}Ir_{17}$-layer since the antiferromagnet does not grow in the required crystalline order for exchange bias. This is why artificial antiferromagnets are used for pinning of the top electrode.

Two different variants are prepared: The bottom ($Mn_{83}Ir_{17}$/$Co_{70}Fe_{30}$/Ru/$Co_{40}Fe_{40}B_{20}$) and top configuration ($Co_{40}Fe_{40}B_{20}$/Ru/$Co_{70}Fe_{30}$/$Mn_{83}Ir_{17}$), depending which electrode of the tunnel junction is pinned. The pinning strength on the artificial antiferromagnet in the top and bottom configuration differ by a factor of 5 at the first coupling extremum.

In the second part, the origin of these differences is explored by analyzing the crystal structure of different ferromagnetic layers via transmission electron microscopy of FIB lamellas.

In the last part, two different double pinned systems are examined. The first one has a natural antiferromagnet pinning at the bottom and and an artificial antiferromagnet for the top electrode. In this layout the bottom layer serves as a sensing- and the top electrode as a reference layer. Consecutive annealing steps and magnetoresistive measurements are performed at increasing temperature. The samples with the highest sensitivity to an external magnetic field are used for inverse magnetostrictive measurements.

In an alternative design for increased sensitivity both electrodes are pinned by an artificial antiferromagnet. The interlayer exchange coupling of the bottom electrode is tuned for a strong coupling, whereas the bias on the top electrode is adjusted to a weak coupling. The sense- and reference layer are changed in this variant. After the same thermal treatment, inverse magnetostrictive measurements are performed on these optimized sensors.

3.1 The natural antiferromagnet $Mn_{83}Ir_{17}$

In a spin valve structure one electrode of the tunnel junction is pinned. This pinning can be realized by a natural or artificial antiferromagnet. For an artificial antiferromagnet, a natural antiferromagnet is required. This is why it is of special interest to investigate the pinning strength and blocking temperature of the natural antiferromagnet used.

3.1.1 Exchange bias through $Mn_{83}Ir_{17}$

In this work the natural antiferromagnet $Mn_{83}Ir_{17}$ is pinning either $Co_{70}Fe_{30}$ or $Co_{40}Fe_{40}B_{20}$ ferromagnetic layers. In the first case the natural antiferromagnet $Mn_{83}Ir_{17}$ is used as a part of an artificial antiferromagnet (AAFM) [37]. While being part of an AAFM the exact exchange bias does not influence the bias on the electrode of the tunnel junction because the electrode is pinned via interlayer exchange coupling.

When pinning the electrode directly by a natural antiferromagnet, the thickness and crystal structure of the antiferromagnet are crucial for the exchange bias [3]. A series of samples is prepared for investigations on the exchange bias. The layer sequence is (thicknesses given in nanometer):

$$\mathrm{Sub}\,/\mathrm{Buffer}\,/MnIr\,(X)/CoFeB\,(5)\,/\mathrm{Capping}$$

The buffer below the $Mn_{83}Ir_{17}$ layer is the same as used in the final tunnel junction to provide the same conditions for the antiferromagnet as in the final system.

The relationship between the thickness (X) of the $Mn_{83}Ir_{17}$-layer and the induced exchange bias is shown in Fig. 3.1. The thicknesses of the $Mn_{83}Ir_{17}$-layeres prepared for this purpose range from 2 nm to 20 nm. The variation of the exchange bias with respect to the thickness of the antiferromagnetic layer is stronger for thin layers (around 4 nm [57]), this is why the density of data points in higher in this thickness regime.

The corresponding exchange bias induced by a 2 nm $Mn_{83}Ir_{17}$-layer is 30 Oe, which is suitable as a pinning of a sensing layer in a MTJ based sensor, however there are arguments from which this is not favorable.

First, the pinning strength is directly related to the sensitivity of the sensor and a small variation would have a huge impact on the exchange bias applied to the reference layer. In the thin regime of the antiferromagnet around three nanometers, a variation of thickness has the highest impact on the exchange bias (see Fig. 3.1).

Second, the coercivity of the $Co_{40}Fe_{40}B_{20}$ layer is increased due to the antiferromagnet and the exchange bias is lower than the coercivity. In this case the direction of the magnetization

in zero field is not well defined. In general an increased coercivity is not favorable for sensing electrodes. Making a sensing layer magnetically harder reduces the sensitivity.
The third argument is is based on the blocking temperature (T_B). The blocking temperature depends on the antiferromagnetic layer thickness. A $Mn_{83}Ir_{17}$ layer thickness of two nanometers results in a low blocking temperature ($T_B < 100\,°C$). At the blocking temperature the exchange bias vanishes, this process starts at even lower temperatures (see Fig. 3.3). This is why the final sensor could not operate reliably at temperatures above room temperature.

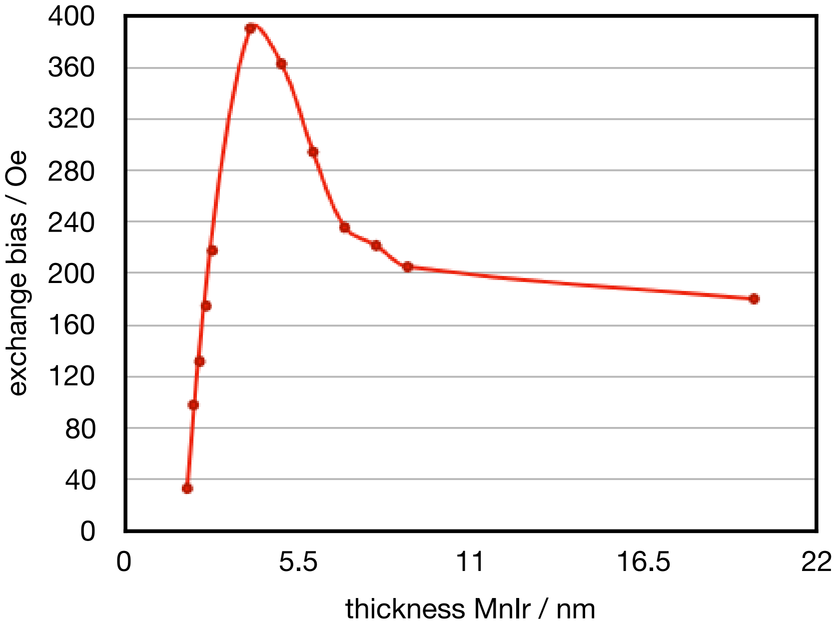

Figure 3.1 – Exchange bias induced to a 5 nm $Co_{40}Fe_{40}B_{20}$ layer by the natural antiferromagnet $Mn_{83}Ir_{17}$ for different thicknesses. The connecting line is only a guide for the eye. Data extracted from MOKE measurements.

3.1.2 Blocking temperature of $Mn_{83}Ir_{17}$

The standard method to determine the blocking temperature distribution of an antiferromagnet is to perform a field cooling process at a temperature below the blocking temperature ($T < T_B$) with a magnetic field aligned antiparallel to the initial pinning direction and measuring the remaining exchange bias. The blocking temperature is reached when the exchange bias vanishes [31].

For this purpose a series of samples with different $Mn_{83}Ir_{17}$ thickness are prepared. The layers (all thicknesses given in nm) of these samples are:

$$\text{Sub}\,/\text{Buffer}\,/Mn_{83}Ir_{17}\,(X)/Co_{70}Fe_{30}\,(3)/\text{Capping}$$

For the determination of the blocking temperature five different thicknesses of $Mn_{83}Ir_{17}$ are chosen: 4 nm, 8 nm, 12 nm, 16 nm and 20 nm.

All samples are annealed at a temperature of 360 °C in an external magnetic field of 5500 Oe. Afterwards a series of annealing steps with an antiparallel external magnetic field with respect to the initial direction are performed. The series starts from 120 °C to 360 °C in steps of 20 °C. After each field cooling process, MOKE measurements are performed to determine the remaining exchange bias.

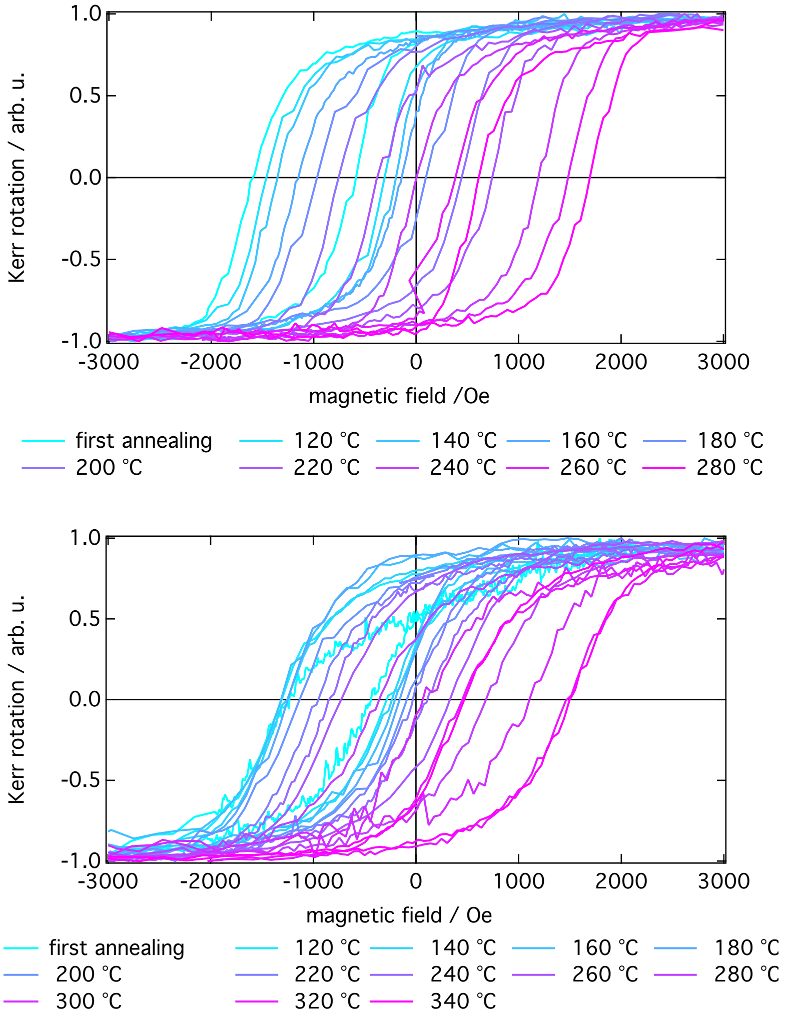

Figure 3.2 – MOKE measurements of a sample with 8 nm (top) and 20 nm (bottom) $Mn_{83}Ir_{17}$ at different annealing temperatures. With increasing temperature the pinning reversal can be observed.

Two of the series of MOKE measurements are shown in Fig. 3.2. The curves in cyan display the measurements after the first annealing step. With increasing temperature the color changes to magenta.

The top graph of Fig. 3.2 represent the sample with a thin $Mn_{83}Ir_{17}$ layer of 8 nm, on the bottom side the results of the measurements of the 20 nm $Mn_{83}Ir_{17}$-specimen measurements are shown. For both samples it can be observed, that the exchange bias starts at approximately 1000 Oe and decreases with increasing temperature. The annealing steps are repeated with increasing temperature until the initial exchange bias (with a reversed sign) is reached. A further increment of the temperature has no impact on the exchange bias. This is why the sequence is stopped at this temperature. As seen in Fig. 3.2 for a thickness of 8 nm this is the case for approximately 280 °C and 340 °C for 20 nm. This reversal temperature is correlated with the blocking temperature. Since the goal of this work is the pinning in certain direction, the reversal temperature is of higher importance.

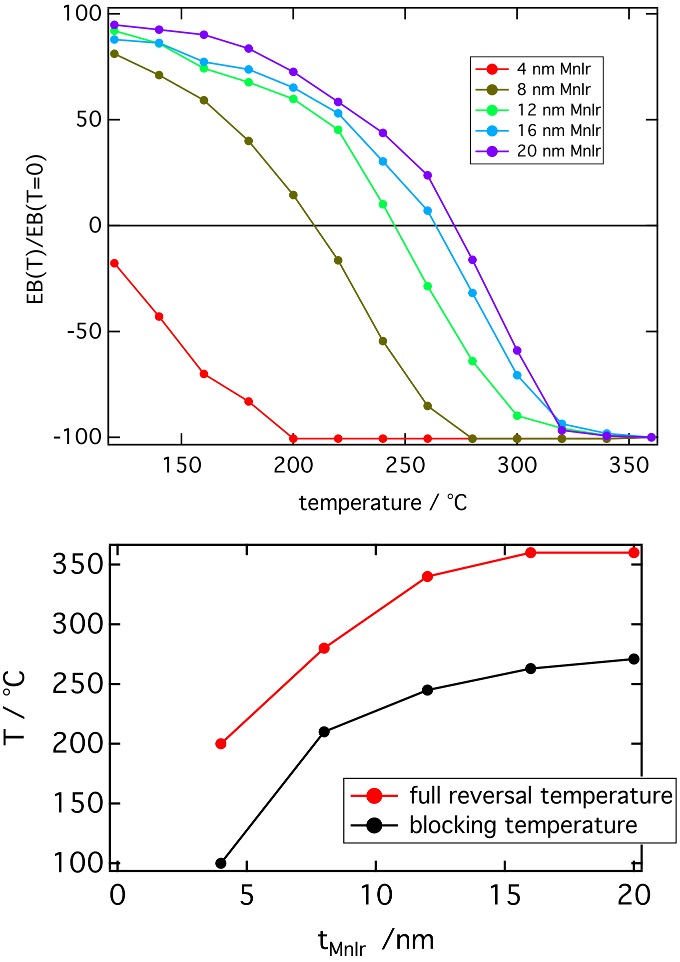

Figure 3.3 – **Top:** Remaining exchange bias with respect to the initial exchange bias after different annealing steps in a reverse field for different $Mn_{83}Ir_{17}$ thicknesses. **Bottom:** Blocking temperature and temperature for a full exchange bias reversal with respect to $Mn_{83}Ir_{17}$ thickness.

The collected results of all measurements are plotted in Fig. 3.3a. A dependence of the blocking temperature of the $Mn_{83}Ir_{17}$ thickness can be easily constituted. The starting treatment with a temperature of 120°C already changed at the 4 nm sample. The realignment of the exchange bias is completed at a temperature of 200 °C. In Fig. 3.3b the temperature required to reach zero exchange bias and for a complete exchange bias reversal is display with respect to the $Mn_{83}Ir_{17}$ thickness. These results are in agreement with results presented in literature [57]. Based on these results a choice for a pair of $Mn_{83}Ir_{17}$-layers (7.5 nm/20 nm) of the double pinned TMR stack is made. A thickness of 20 nm results in a high blocking temperature while a small variation of the thickness has almost no impact. For the second antiferromagnetic layer a thickness of 7.5 nm is chosen for a high thermal stability and enough difference in blocking temperature to rotating the pinning direction.

In an artificial antiferromagnet the results of the blocking temperature may differ because of a different crystal structure. This is why crystal structure of an antiferromagnet is important for exchange bias [18]. As a consequence these experiments are performed with a top pinning artificial antiferromagnet. The layers of the stack are:

$$\text{Sub}/MgO\,(1.7)/Co_{40}Fe_{40}B_{20}\,(3)/Ru\,(0.9)/Co_{70}Fe_{30}\,(3)/Mn_{83}Ir_{17}\,(7.5)/\text{Capping}$$

Fig. 3.4 shows the remaining exchange bias of the top pinning configuration with respect to the bias after the first annealing step with increasing temperature of the second annealing. The pinning of the $Co_{70}Fe_{30}$ and $Co_{40}Fe_{40}B_{20}$ layers are shown separately. The relative remaining exchange bias of the two different ferromagnets of the artificial antiferromagnet have the same temperature dependency. This indicates that the natural antiferromagnet defines the direction of the bias for a fixed interlayer exchange coupling. The blocking temperature of a top pinned artificial antiferromagnet is comparable with the natural antiferromagnet.
This is an important result because a difference in the blocking temperature can be caused by the crystal quality of the antiferromagnet (see Chap. 1.3) [18, 57].

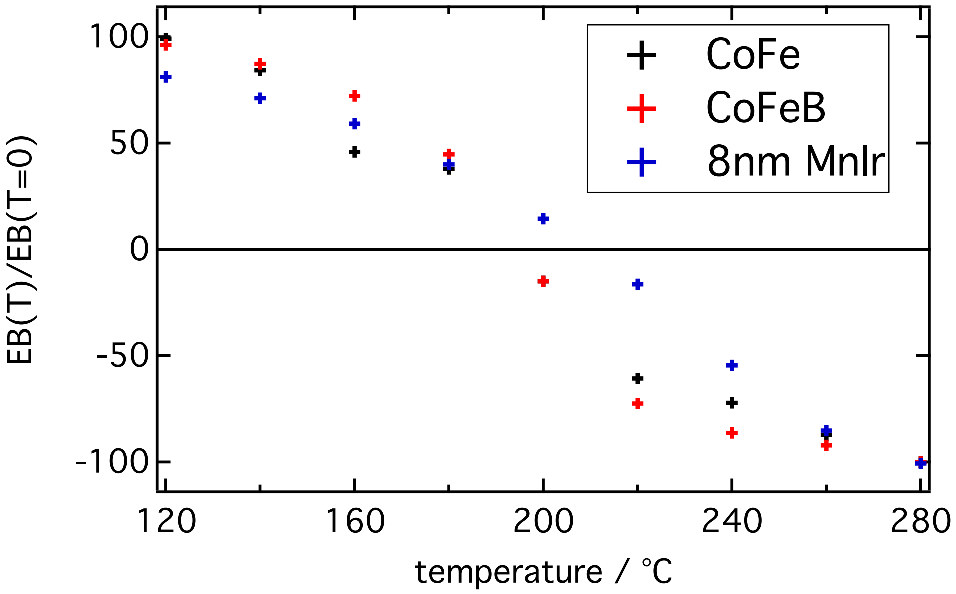

Figure 3.4 – Unblocking of a top pinning artificial antiferromagnet due to reverse field cooling processes. The remaining exchange bias with respect to the initial bias for the $Co_{70}Fe_{30}$ and $Co_{40}Fe_{40}B_{20}$ layer are shown. The data from a pinning of 8 nm $Mn_{83}Ir_{17}$ to a $Co_{70}Fe_{30}$ layer are shown for comparison.

3.2 Artificial Antiferromagnets

In this chapter the results of the investigation on *interlayer exchange coupling* (IEC) of top and bottom pinning artificial antiferromagnet configurations are shown and discussed.

In general an artificial antiferromagnet is composed of a natural antiferromagnet ($Mn_{83}Ir_{17}$), pinning a ferromagnet ($Co_{70}Fe_{30}$). This ferromagnetic layer is coupled to a second ferromagnet ($Co_{40}Fe_{40}B_{20}$) by a thin interlayer (Ru) via IEC [9].
Samples with a fixed $Mn_{83}Ir_{17}$ thickness and different ruthenium interlayer thicknesses are deposited. After a field cooling process the attainable pinning strengths of this pinning method are examined via MOKE.

Huge differences of the top- and bottom configuration, in terms of pinning strengths, are observed. A possible reason of these differences is investigated in Chap. 3.3.

Top artificial antiferromagnet

For investigation a top configuration the following layer order is used:

$$\begin{aligned}\text{SuB}\,/MgO\,(1.7)/Co_{40}Fe_{40}B_{20}\,(3)/Ru\,(X)/\\ Co_{70}Fe_{30}\,(3)/Mn_{83}Ir_{17}\,(7.5)/\text{Capping}\end{aligned}$$

The ruthenium interlayer is sputtered in a range from 0.7 nm to 2.3 nm in steps of 0.1 nm. As described in Chap. 3.2 a lower sputtering rate (30 W, sputtering rate 0.0076 nm/s) is used to reduce a variation of the ruthenium thickness.
In this configuration the $Co_{70}Fe_{30}$ layer is pinned by the natural antiferromagnet $Mn_{83}Ir_{17}$. From earlier measurements (see Chap. 3.1.2) an exchange bias of approximately 1000 Oe induced to the $Co_{70}Fe_{30}$-layer is expected. The interlayer exchange coupling between the two ferromagnetic layers ($Co_{70}Fe_{30}$/ $Co_{40}Fe_{40}B_{20}$) influences both magnetization reversals of these layers. Consequently, a variation of the ruthenium interlayer thickness, does not only change the magnetic shift of the $Co_{40}Fe_{40}B_{20}$ layer, but influences also the $Co_{70}Fe_{30}$-layer.
The bias of the $Co_{70}Fe_{30}$ layer ranges from −1300 Oe to −600 Oe while the $Co_{40}Fe_{40}B_{20}$ has a range of −350 Oe to 250 Oe as seen in Fig. 3.5. The magnetization reversals of the two different layers are shown in Fig. 3.6.

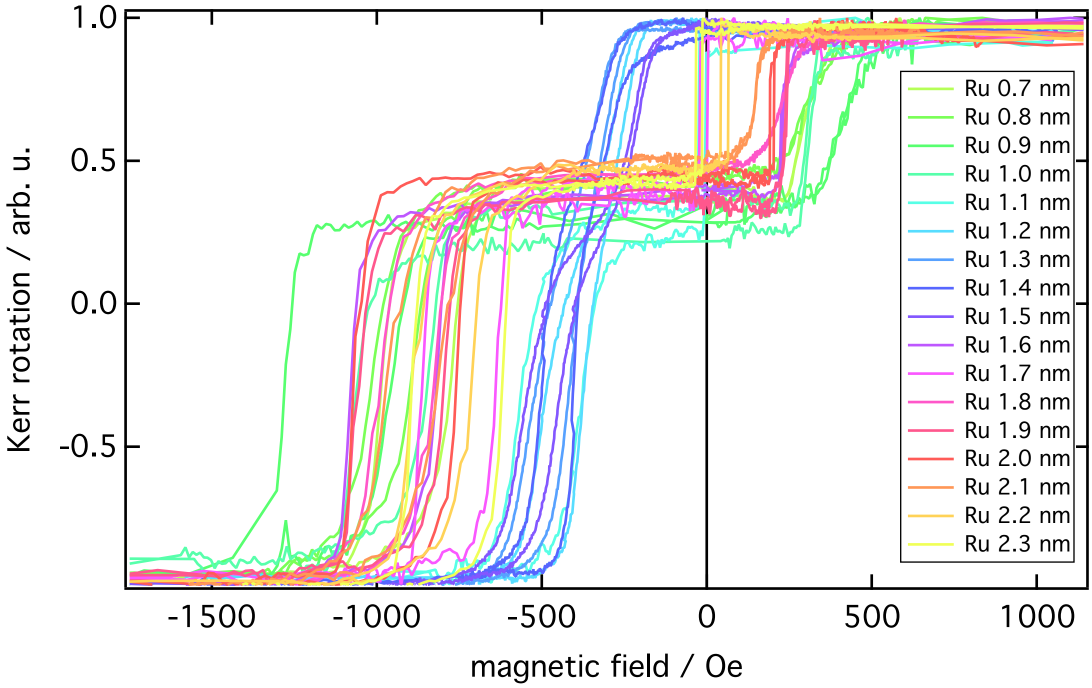

Figure 3.5 – Series of MOKE measurements of the top pinning configuration of the artificial antiferromagnet. The thickness of the two ferromagnetic layers is held constant. The ruthenium thicknesses of the interlayer are varied from 0.7 nm to 2.3 nm in steps of 0.1 nm. The switching of the $Co_{70}Fe_{30}$ layer is shifted to the negative field direction whereas the magnetization reversal of the $Co_{40}Fe_{40}B_{20}$ can be shifted in either directions based on the ruthenium thickness.

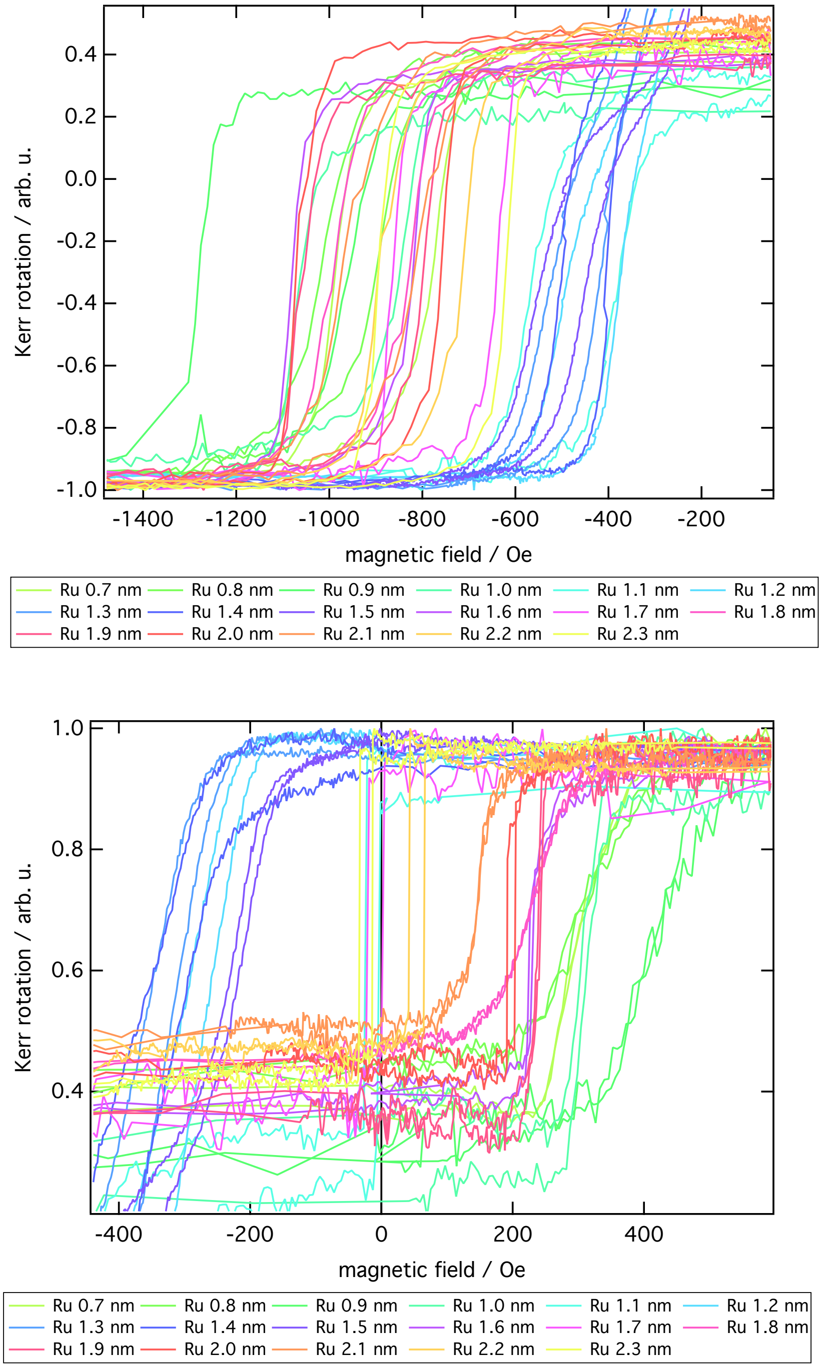

Figure 3.6 – Magnified areas of Fig. 3.5 **Top**: $Co_{70}Fe_{30}$ layer pinned by the natural antiferromagnet $Mn_{83}Ir_{17}$ and the IEC to the $Co_{40}Fe_{40}B_{20}$ layer. **Bottom**: $Co_{40}Fe_{40}B_{20}$ layer coupled via IEC to the $Co_{70}Fe_{30}$ layer.

The bias induced to the $Co_{40}Fe_{40}B_{20}$ layer is displayed in Fig. 3.7. The highest coupling strength is correlated to an interlayer thickness of 0.9 nm as expected [90]. The periodicity of the oscillation is approximately 1 nm.

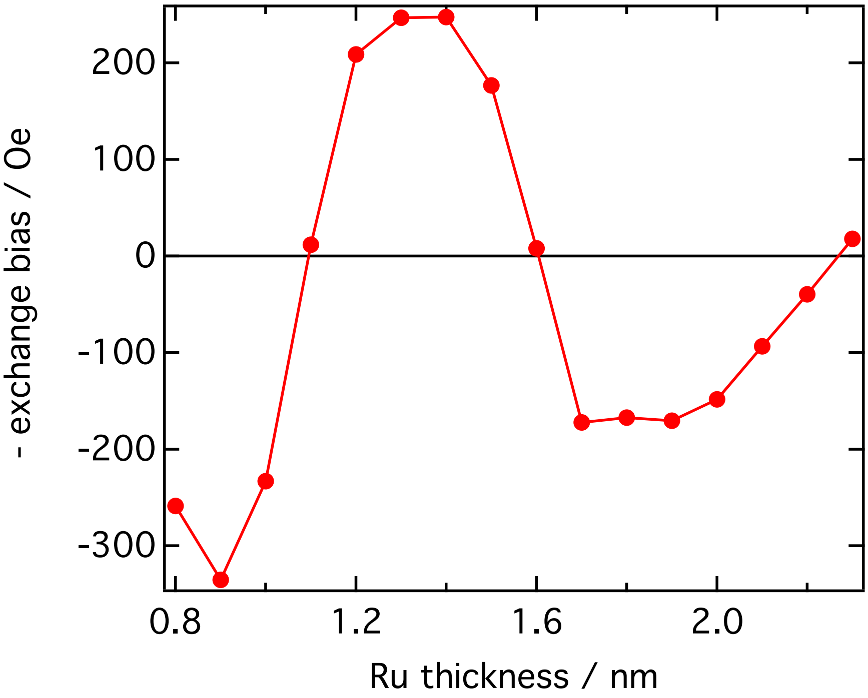

Figure 3.7 – Magnetic bias caused by the interlayer exchange coupling to a 3 nm $Co_{40}Fe_{40}B_{20}$ thin film in the top configuration of an artificial antiferromagnet with respect to the interlayer thickness. The connecting lines are only a guide to the eye.

Bottom artificial antiferromagnet

The samples for the bottom configuration of the artificial antiferromagnet are similar to the lower part of a TMR stack with MgO on top and a capping layer (all thicknesses given in nm):

$$\begin{aligned} &\text{Sub}\,/\text{Buffer}/Mn_{83}Ir_{17}\,(20)/Co_{70}Fe_{30}\,(3)/\\ &\qquad Ru\,(X)/Co_{40}Fe_{40}B_{20}\,(3)/MgO\,(1.7)/\text{Capping}\end{aligned}$$

The result of a complete set of measurements of the magnetization reversal of the $Co_{40}Fe_{40}B_{20}$ layer is shown in Fig. 3.8.

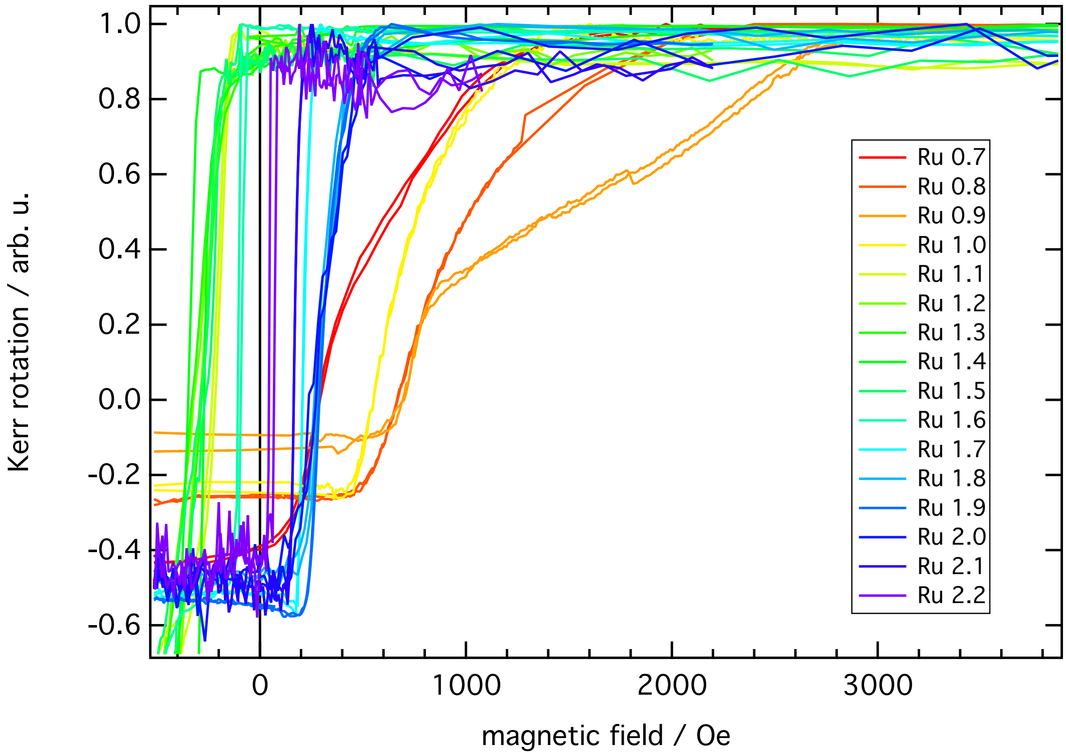

Figure 3.8 – Magnetization reversal of the $Co_{40}Fe_{40}B_{20}$ layer of the bottom pinning configuration of an artificial antiferromagnet. The ruthenium interlayer thickness has been varied from 0.7 to 2.2 nm in steps of 0.1 nm demonstrating the high impact on the interlayer exchange bias when pinning from the bottom.

A huge difference compared to the measurements of the top pinning (see Fig. 3.5) in terms of magnitude of exchange bias can be observed. The maximum in pinning strength differs by a factor of up to five for an interlayer thickness around the coupling extremum of 0.9 nm of ruthenium. The shape of the magnetization reversal is dependent on the coupling strength. As an example the orange curve (0.9 nm ruthenium) starts at 600 Oe at a slope of $2.13 \cdot 10^{-3}\,{}^{1}/_{Oe}$ (on the ± 1 normalized Kerr rotation axis). The saturation of the magnetization starts at magnetic field of 2800 Oe. Until this external field strength, the slope is reduced up to $4.04 \cdot 10^{-4}\,{}^{1}/_{Oe}$.

For the application as stress sensors the particular shape of the magnetization of the reference layer is less important. The reference layer is only required not to change its magnetization direction under mechanical stress. The influence of the stress induced anisotropy is too weak, compared with such a strong pinning.

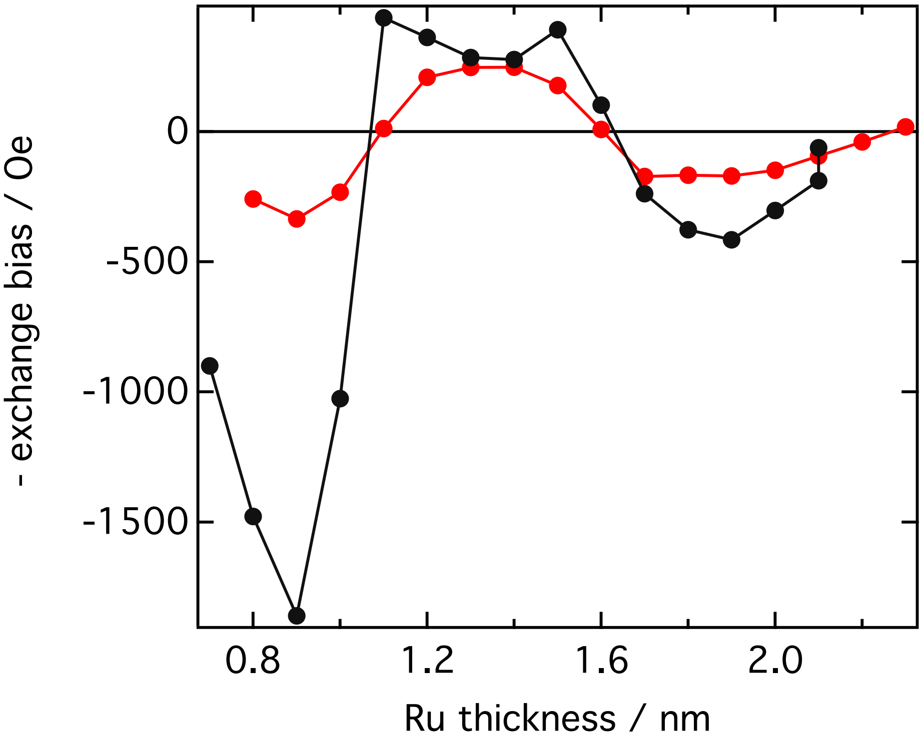

Figure 3.9 – Comparison of the bias induced by top (red) and bottom (black) pinning by an artificial antiferromagnet. A big difference in the magnitude of the coupling is shown while the periodicity remains the same. The connecting lines are only a guide to the eye.

Fig. 3.9 illustrates a comparison between the pinning strength of an artificial antiferromagnet in the top and bottom configuration. A huge difference in the amplitude is to be noticed. At an interlayer thickness of 0.9 nm this difference can be seen very clearly. Between an interlayer thickness of 1.1 nm to 1.5 nm the coupling of the bottom configuration takes a non expected curvature. The coupling is ferromagnetic in this interval and the interlayer coupling strength is exceeding the exchange bias of the artificial antiferromagnet.

This is why the $Co_{70}Fe_{30}$ and $Co_{40}Fe_{40}B_{20}$ layers of the artificial antiferromagnet are switching like one ferromagnetic layer which is pinned by the $Mn_{83}Ir_{17}$ antiferromagnetic layer. Information about the interlayer exchange coupling can not be extracted.

Reproducibility of interlayer exchange coupling

The reproducibility of the ruthenium interlayer thickness in an artificial antiferromagnet goes along with the exchange coupling constant. It is an important factor in the sensor production since it has a direct impact on sensitivity of the sensor. Therefore this aspect has to be taken into account as well.

The focus of this investigation lies on the top configuration of the artificial antiferromagnet. The sensor that is equipped with a natural and an artificial antiferromagnet uses the top electrode as a reference layer. So a small variation in the coupling constant does not influence the performance of the sensor as much as the pinning strength of the sense layer. In contrast to that the double artificial antiferromagnet configuration utilizes the top electrode as a sense layer and therefore the pinning strength is a crucial parameter. Fig. 3.10 illustrates the aforementioned issue.

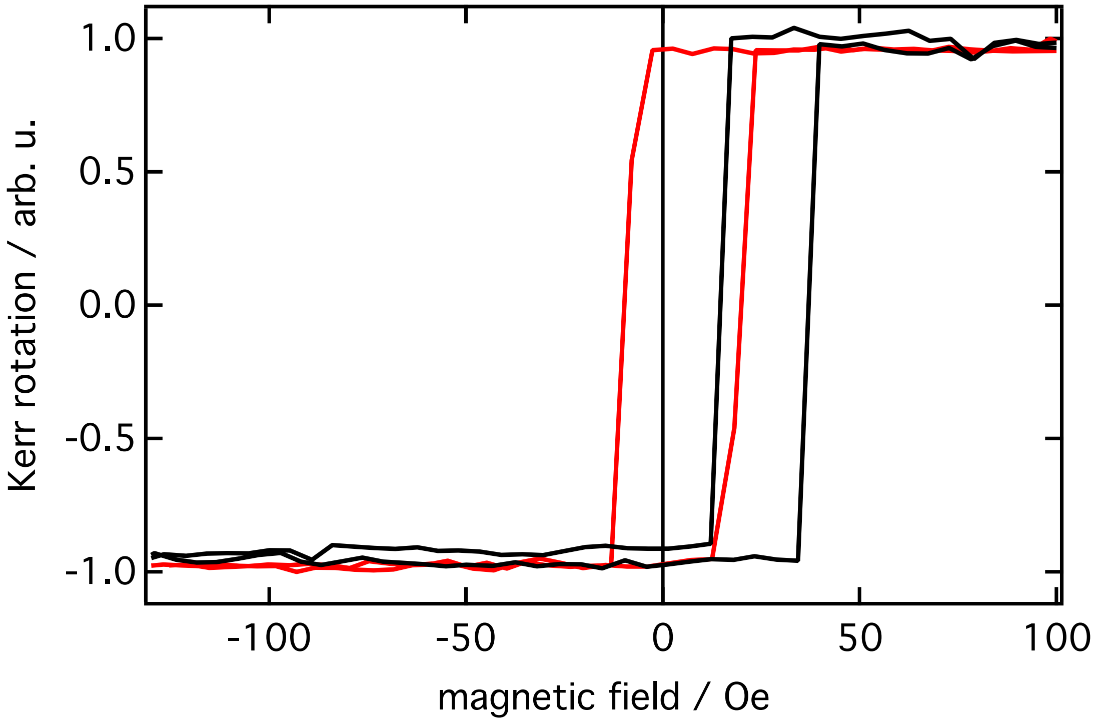

Figure 3.10 – Switching of the reference layer in a double artificial antiferromagnet structure. Two consecutive samples sputtered under exactly the same conditions. The thickness of the interlayer of the artificial antiferromagnet has a expected thickness of 1.05 nm.

The graph shows a cutout of a MOKE measurement of a complete TMR junction in the double artificial antiferromagnet configuration. The pinning of the reference layer is tuned to a maximum pinning strength whereas the sensing electrode has a bias which is slightly stronger than the coercive field. Only the switching of the top electrode is shown. The chosen ruthenium thickness of the top artificial antiferromagnet is 1.05 nm.

Two consecutive samples have been prepared at the same sputtering conditions and investigated on. A considerable difference in the bias can be observed. The coupling constant in the first sample (red curve) is zero, resulting in no bias. The ruthenium of the artificial antiferromagnet is slightly thicker in the sample corresponding to the black curve. It results in a bias of approximately 25 Oe. Such a strong variation is not acceptable.

Fig. 3.11 shows two series of the interlayer exchange coupling strength with respect to the interlayer thickness. These two series have been sputtered six month apart from different ruthenium targets. The two curves are in a good agreement and with some differences in the low thickness regime. This is a indicator that thicker interlayers will result in a higher reproducibility.

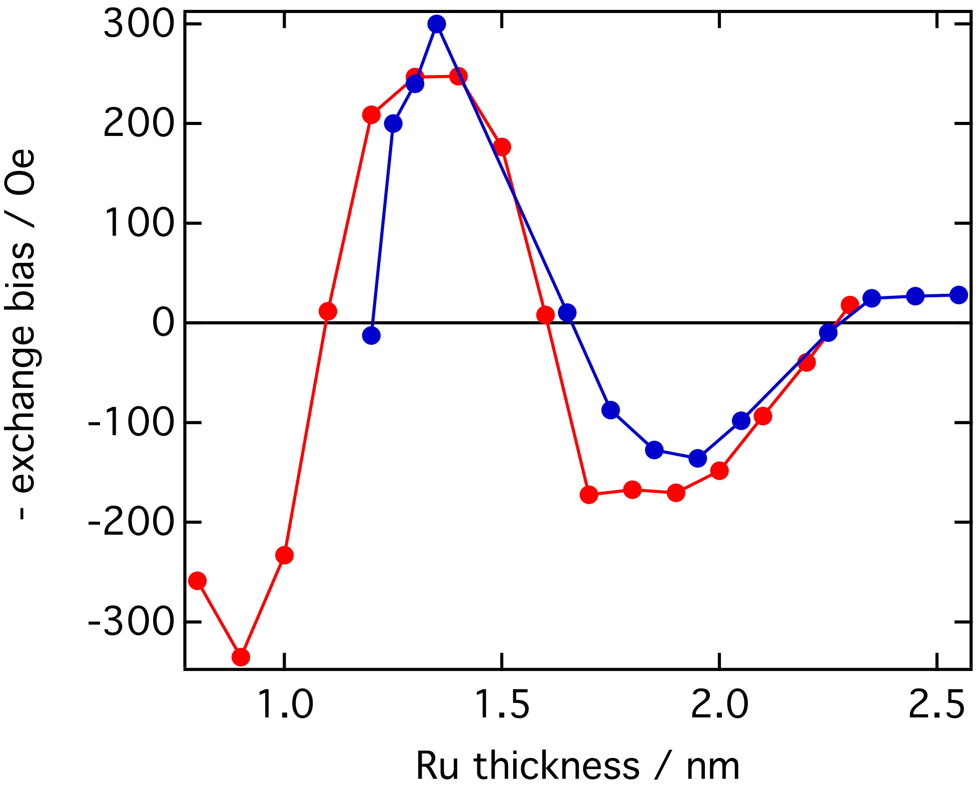

Figure 3.11 – Two series presenting the interlayer exchange coupling dependence of the interlayer thickness. The samples corresponding to the blue curve have been made in January 2017, the ones for the red in July of the same year.

Consecutive samples with a 2 nm ruthenium interlayer thickness are prepared and investigated by MOKE. The results of this measurement are shown in Fig. 3.12.

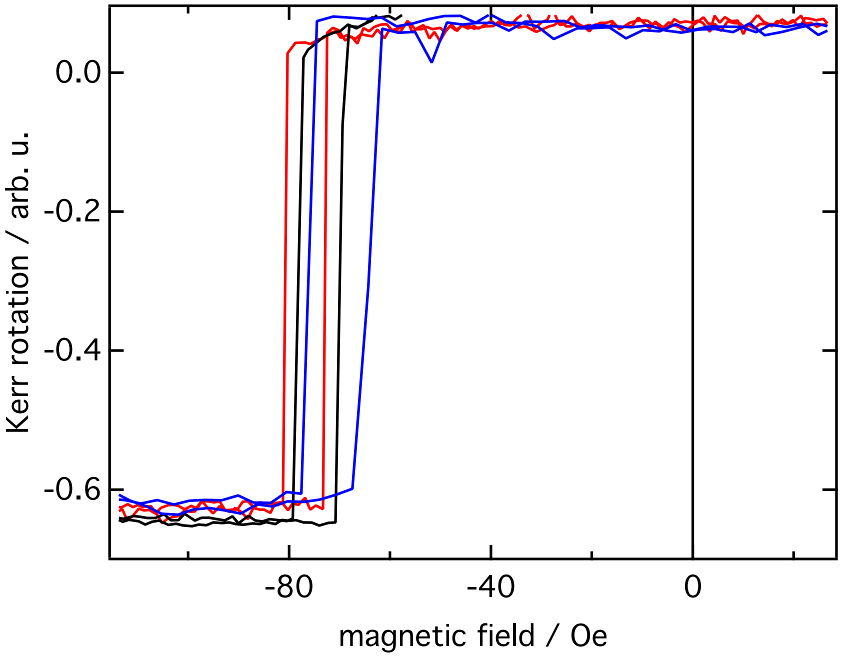

Figure 3.12 – MOKE measurements of three consecutively sputtered samples displaying the switching of the weak pinned $Co_{40}Fe_{40}B_{20}$ layer by an artificial antiferromagnet with a ruthenium interlayer thickness of 2 nm. The maximum difference in coupling strength is 7 Oe.

A complete double pinned tunnel junction is investigated on but only the switching of the top electrode is shown. Three consecutive samples are prepared and measured. In contrast to earlier made samples (see Fig. 3.10), the reproducibility is much better with a maximum exchange bias difference of 7 Oe. It is less error-prone to produce thicker interlayer. Due to the lower sputtering rate, the deposition time is increased. A small variation in the process has a reduced influence on the thickness of the interlayer. At thicker ruthenium interlayers, the same change of the absolute thickness leads to a smaller bias variation.

Ruthenium homogeneity on a 4”-wafer

The bias induced to the sensing layer is directly related to the sensitivity of the final sensor. For a future mass production of these sensors, effective measuring techniques of the interlayer thickness, on wafer scale, have to be found. Measuring the exchange bias by Kerr microscopy is a possibility. MOKE measurements at different positions on the wafer are performed to map the homogeneity of the ruthenium deposition in the used sputtering system.

With the results from Chap. 3.2 it is possible to calculate of the ruthenium interlayer thickness from the value of the interlayer exchange coupling.

This assumption is true under the condition of a constant $Co_{40}Fe_{40}B_{20}$ layer thickness because the coupling strength is also a function of the ferromagnetic layer thickness. Without monitoring the $Co_{40}Fe_{40}B_{20}$ layer thickness, the ruthenium interlayer mapping would not be possible. Fortunately, the amplitude in a MOKE measurement depends on the ferromagnetic layer thickness.

In order to investigate the homogeneity of ruthenium, the top configuration was deposited on a 4”-wafer. This wafer is cut into different pieces and MOKE measurements are performed on each of them after a field cooling process.

Fig. 3.13 displays a picture of the wafer directly after the deposition process. The markers indicate the MOKE measuring positions except for the white one. The measurement at this position is not shown, because no MOKE signal can be measured.

Several structures can be observed in the picture. The top and bottom lines are only a reflection of the ceiling when the picture was taken. The sickle-shaped structure on the right side of the wafer is generated during the sputtering process. It is caused by a problem with the shutter in the Leybold sputtering tool during the deposition. This is why not all layers are deposited on the wafer and no MOKE signal can be observed.

Most of the MOKE measurements match well, except three, corresponding to the curves drawn in the orange, blue and purple.
The orange one does not only differ in the bias induced but also in the amplitude of the MOKE signal. The average MOKE amplitude (in arbitrary units) is 0.97 arb. u. in contrast to that the signal of the $Co_{40}Fe_{40}B_{20}$ layer of the orange curve is only 0.49 arb. u. When taking into account that the value of the bias has a linear relation to ferromagnetic thickness, the adjusted exchange bias would be around 400 Oe. This does not lead to a complete accordance with the other measurements but demonstrates which information can be gathered from MOKE measurements. It is possible that the optical analysis of the wafer was not sufficient to identify the area on the wafer that were not processed correctly.

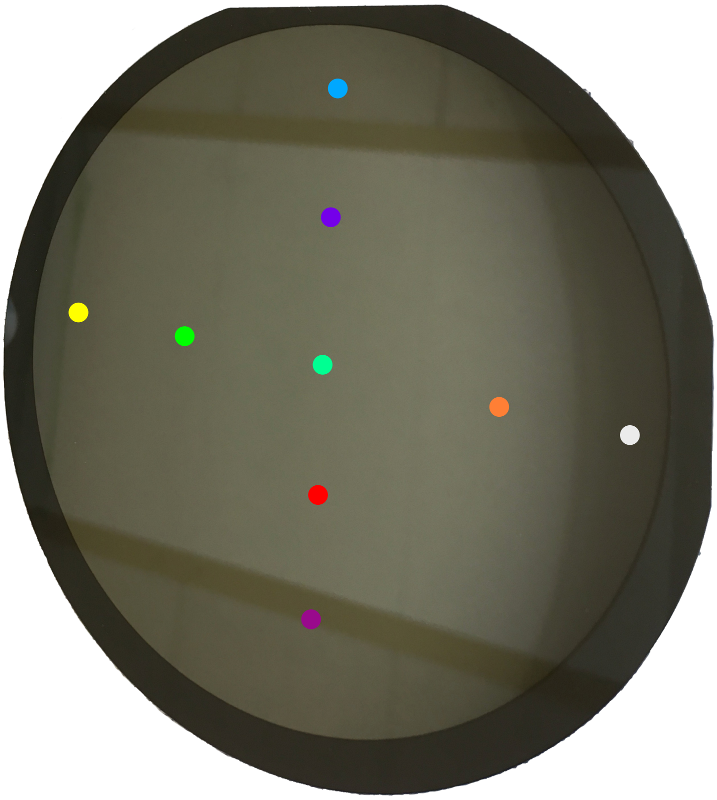

Figure 3.13 – Digital picture of a 4” wafer with an artificial antiferromagnet in the top configuration. The bars at top and bottom are reflections. The sickle-shaped area on the right side is on the wafer and a consequence of a shadowing during the deposition. The markers represent the MOKE measuring positions. The color of the markers match the measured curves displayed in Fig. 3.14.

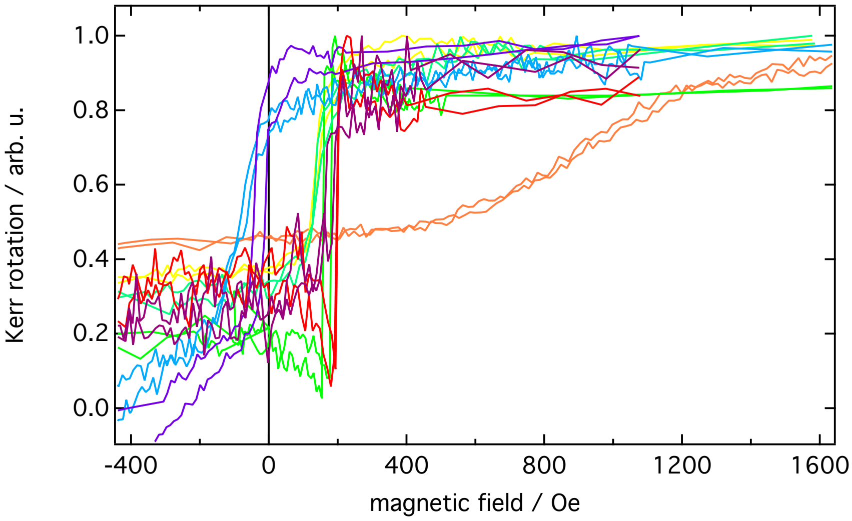

Figure 3.14 – MOKE measurements on different positions of a 4” wafer. A top artificial antiferromagnet has been prepared to compare the ruthenium homogeneity. Only the magnetization reversal of the $Co_{40}Fe_{40}B_{20}$ layer is shown.

3.3 Interlayer exchange coupling strength

The difference in coupling strength between the top and bottom pinning configuration of the artificial antiferromagnet is investigated.

The shape of the magnetization reversal of the bottom configuration differs when tuned to a strong coupling. As seen in Fig. 3.8 the orange curve with an interlayer thickness of 0.9 nm does not have a single slope but can be divided into two different parts. At an external magnetic field of 400 Oe a sharp switching can be observed. Up to 3100 Oe a comparably flat magnetization reversal is shown.

Micromagnetic simulations are performed with the *object oriented micromagnetic framework* (OOMMF). A very simple model is used for these simulations. It consists of two ferromagnetic layers with thicknesses of 3 nm. The saturation magnetization are assumed as $1320\,{}^{emu}\!/_{cm^3}$ for $Co_{70}Fe_{30}$ and $1060\,{}^{emu}\!/_{cm^3}$ for $Co_{40}Fe_{40}B_{20}$ [44]. The modeling of the exchange bias is a constant magnetic field of 1000 Oe, applied to the $Co_{70}Fe_{30}$ layer. This value is taken from the measurements of the blocking temperature (See Chap. 3.1.2). The increased coercivity due to the exchange bias is not taken into consideration. Different coupling constants are chosen to simulate different interlayer thicknesses. The results for the ferromagnetic layer pinned via IEC are shown in Fig. 3.15.

As seen from these results a difference in the coupling strength can lead to the same magnetization reversal shape as observed in the MOKE measurements. A MOKE measurements of the magnetization reversal of the strongest IEC (bottom pinning, 0.9 nm) is displayed together with a corresponding OOMMF simulation. In consideration of the simplicity of the model, measurement and simulation are in good agreement. The two-part magnetization reversal can be achieved with two homogenous ferromagnetic layers and a single coupling.

Differences between the measurements and simulations are caused by the simplicity of the model. The exchange bias is replaced by a constant magnetic field, temperature is not part of the model and the size is limited to 20 by 20 cells in lateral expansion (each being $25 \times 25\,\mathrm{nm}^2$).

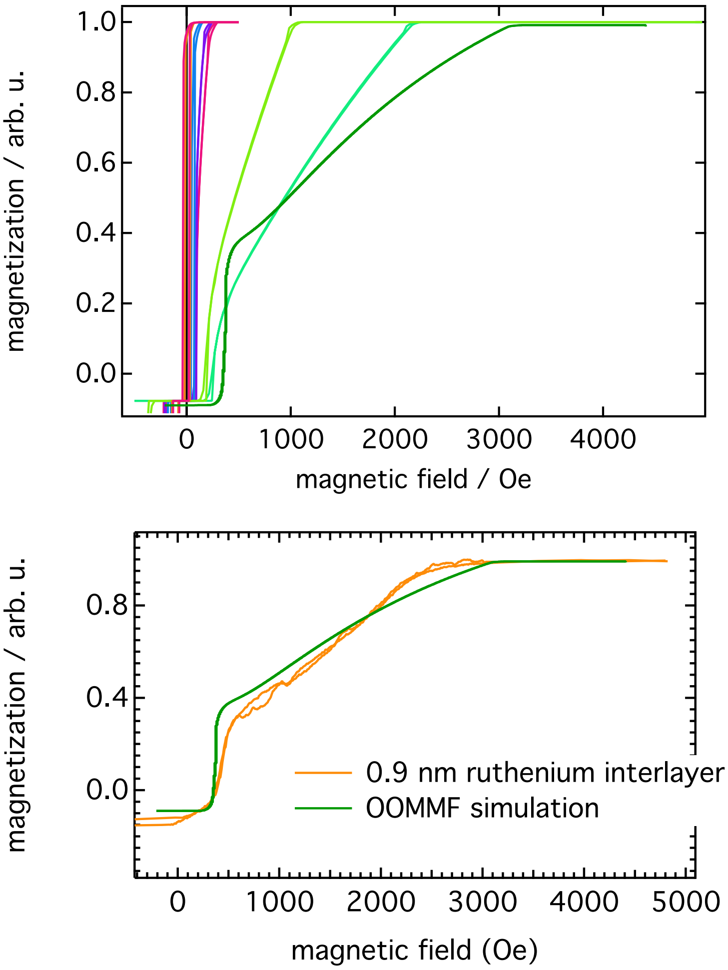

Figure 3.15 – Top: Calculated magnetization reversal of an artificial antiferromagnet. Only the switching of the ferromagnetic layer pinned by the interlayer exchange bias is shown. Bottom: Comparison of an OOMMF simulation with a MOKE measurements of a bottom artificial antiferromagnet with a 0.9 nm ruthenium interlayer.

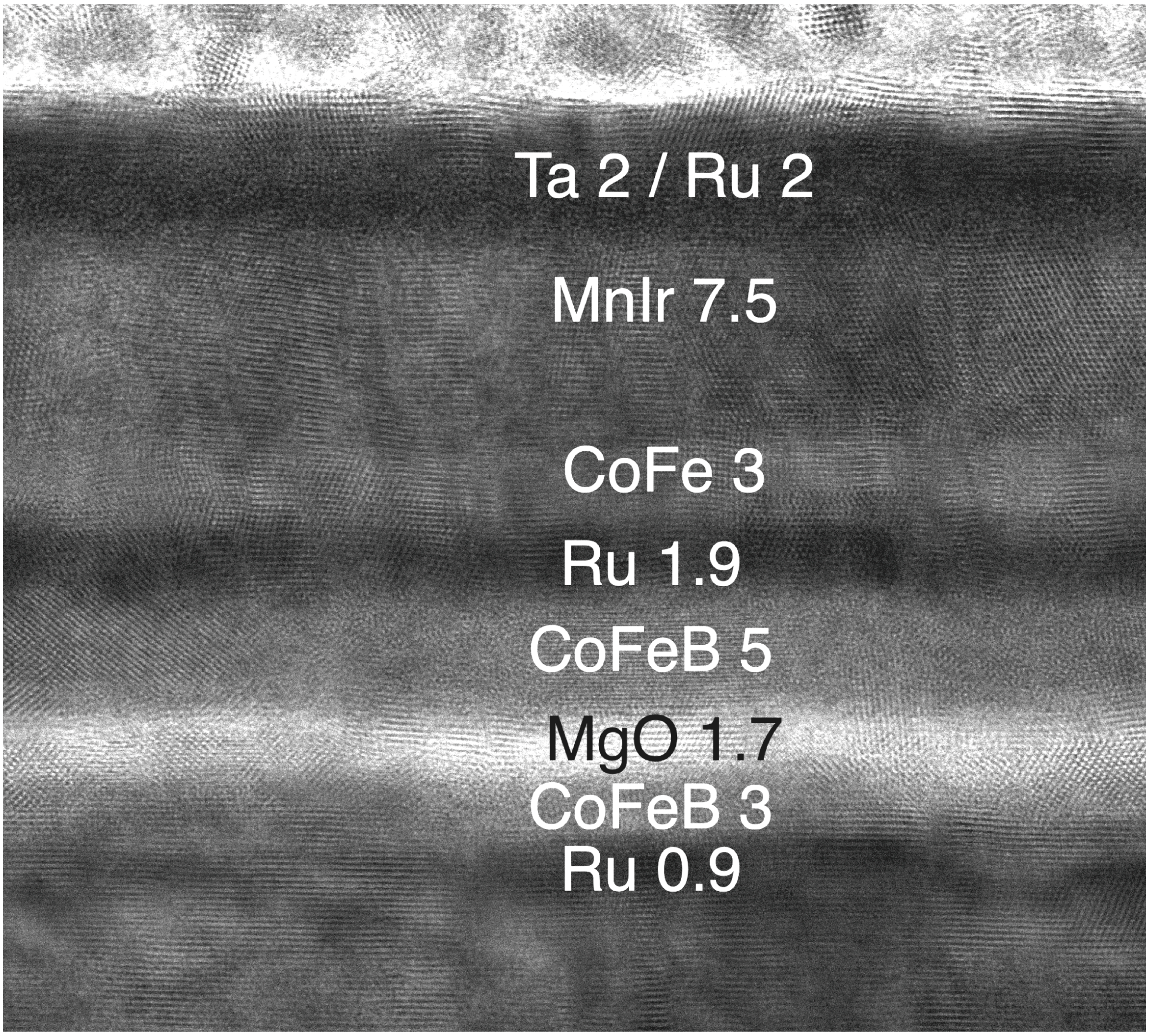

Figure 3.16 – Transmission electron microscopy picture of a lamella with a thickness of 20 nm produced by focussed ion beams. The upper part of a double pinned tunnel junction is shown.

Fig. 3.16 illustrates the direct image of an approximately 20 nm thin lamella of a double pinned TMR junction. Both electrodes are pinned by an artificial antiferromagnet. The bottom artificial antiferromagnet has a ruthenium interlayer with a thickness of 0.9 nm (a maximum of the coupling strength) and the top one 1.9 nm, resulting in a weak pinning of the sensing layer with a high reproducibility. A contrast among the different elements can be observed. The thicknesses of the different layers is given in nm in the picture. The ruthenium interlayer of the AAFM pinning the bottom electrode with a nominal thickness of 0.9 nm does not form a flat layer. In theory the value of the interlayer exchange bias should be quantized based on the number of ruthenium layers. The tuning should be only possible within the borders of these distinct layers. In reality this is not the case, because in TMR and MOKE measurement an averaging on the investigated area is performed. This is why it is possible to set the bias for a TMR sensor to any desired value.

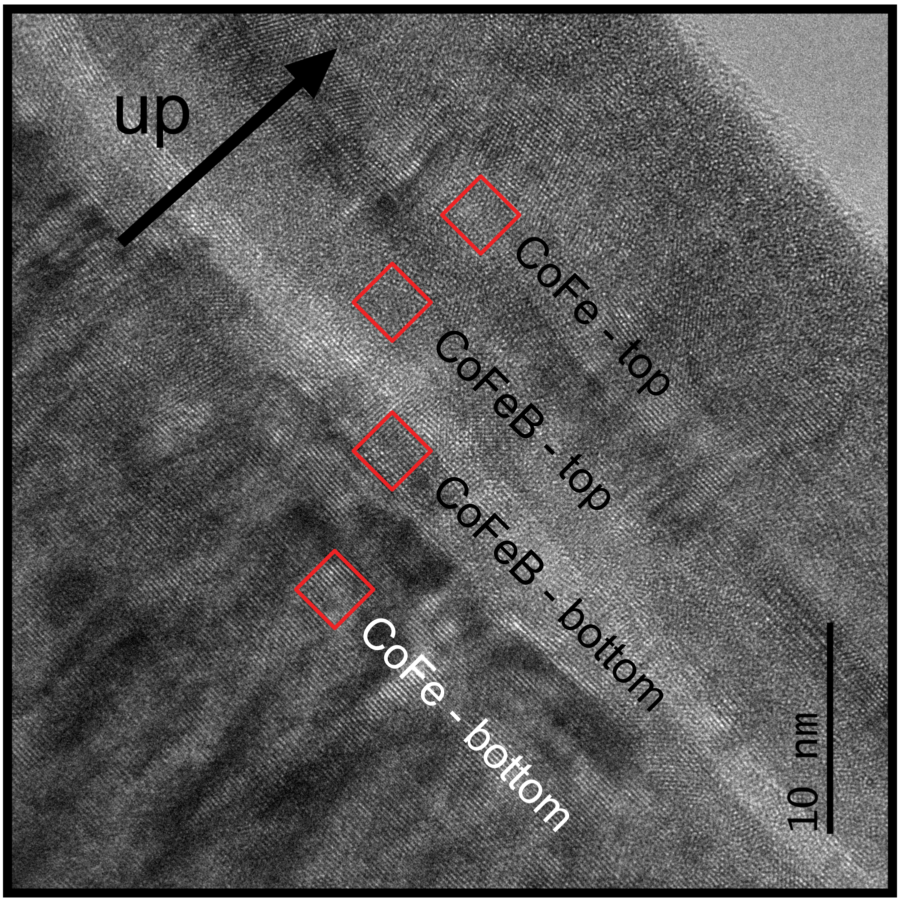

Figure 3.17 – TEM picture of a FIB lamella that was used for the crystal structure determination. The picture is tilted by 45 °. The squares indicate the areas which were taken into account for the FT.

For every investigated layer, an area of approximately 20 nm^2 is taken into account for the Fourier transformation based analysis.

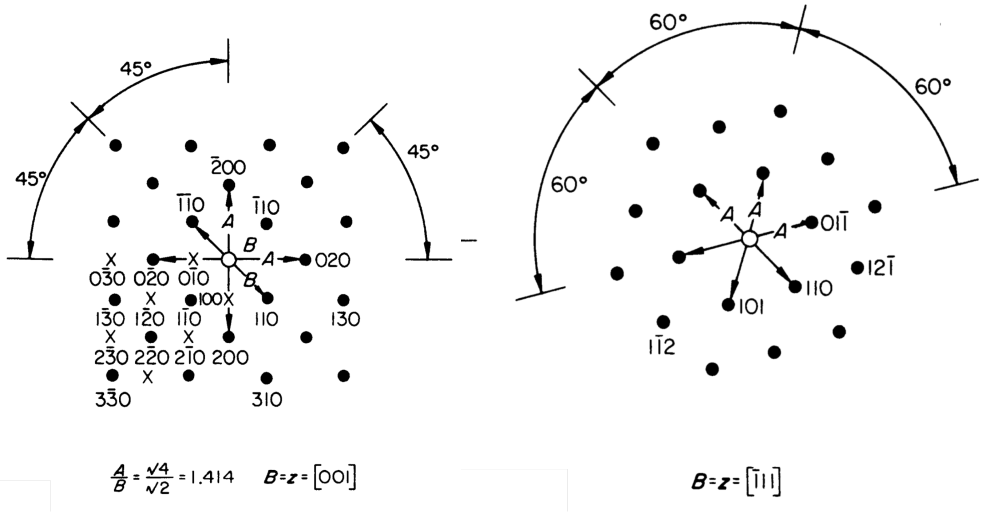

Figure 3.18 – Single-crystal spot diffraction pattern for the bcc crystal structure. Two crystal orientations (Left: [001], Right:$[-111]$) are shown. Taken from [32].

Bottom artificial antiferromagnet

The bottom configuration of the artificial antiferromagnet has a maximum bias up to 1800Oe. The buffer below the $Mn_{83}Ir_{17}$ layer is designed to induce a good crystal quality in the antiferromagnetic layer (see Chap. 2.9). The $Co_{70}Fe_{30}$ layer grows mostly in the $[-111]$ phase. This is caused by the $Mn_{83}Ir_{17}$ layer below. The buffer is build to induce this crystal structure in the antiferromagnetic layer and the $Co_{70}Fe_{30}$ layer directly above grows in the same direction.

The bottom electrode has a different structure. Two different crystal structures can be found: $[-111]$ and $[001]$. The $Co_{40}Fe_{40}B_{20}$ layer is deposited as an amorphous layer and crystallizes during the annealing. During its crystallization process, the bottom electrode is influenced by the MgO tunneling barrier and the Ru/$Co_{70}Fe_{30}$ layer below. Kanak et al. did show that the crystallization of the CoFeB electrode in bcc CoFe in an exchange biased magnetic tunnel junction is different, depending on the layer below the CoFeB layer [64].

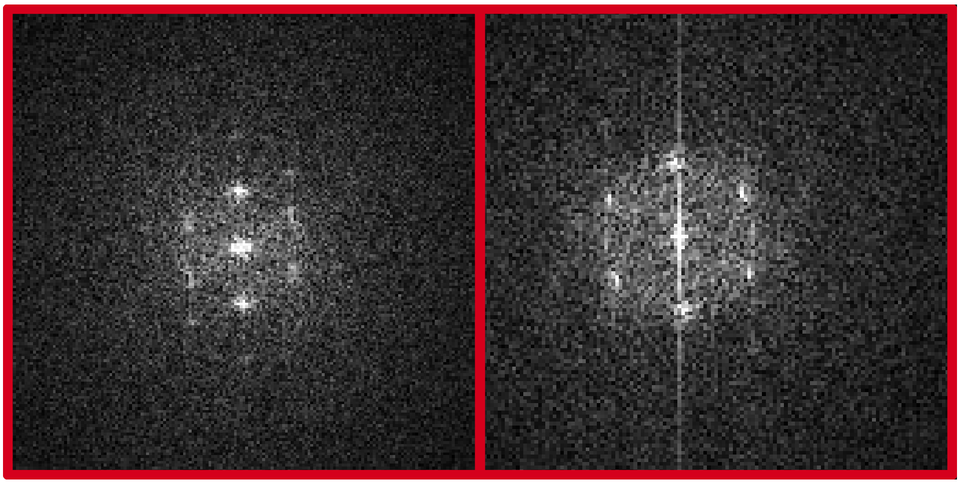

Figure 3.19 – Examples of the Fourier transform of the two ferromagnetic layers of the bottom artificial antiferromagnet and electrode. The positions used for the FT are shown in Fig 3.17 **Left**: $Co_{70}Fe_{30}$ **Right**: $Co_{40}Fe_{40}B_{20}$.

An example of the determination of the crystal structure is performed for the $Co_{70}Fe_{30}$ of the bottom artificial antiferromagnet. The direct TEM image is shown in Fig. 3.17, the Fourier transformed in Fig. 3.19. This pattern is compared to standard spot patterns [32]. Part of this comparison are the ratio of different axis and the angle between them (see Fig. 3.18). Line scans of the diffraction patters are performed to measure the lengths of the axis (Fig. 3.20). The ratio of A (17 pixel) and B (12 pixel) is approximately 1.42. The angle is 45°. This matches the parameters of the bcc $[001]$ direction (ratio: $\sqrt{2} \approx 1.41$, angle: 45°). In this way the crystallographic direction of all four ferromagnetic layers is determined at different positions.

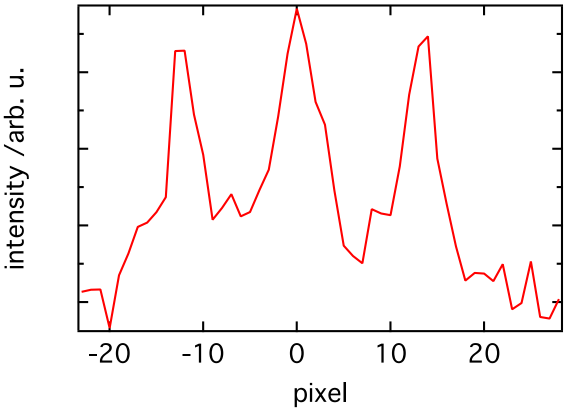

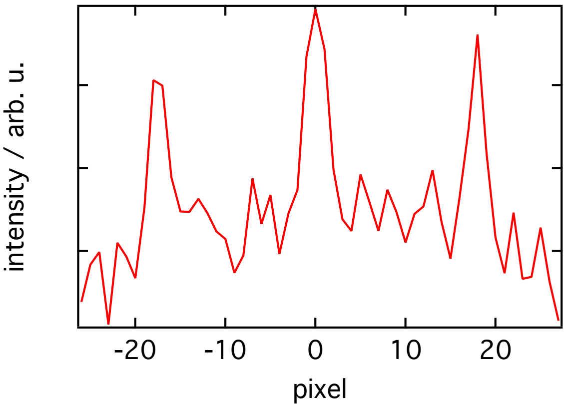

Figure 3.20 – Line scan of the diffraction pattern of the bottom $Co_{70}Fe_{30}$ layer. Top (Bottom): Scan along the A (B) axis of Fig. 3.18.

Top artificial antiferromagnet

The top configuration has a different pinning strength maximum of approximately 350 Oe. The top electrode has a lower degree of crystallinity in comparison to the bottom electrode. In several areas it was not possible to determine a crystal structure. In some areas it was possible to discover [001] phases which are induced by the same structure from the MgO tunneling barrier. The $Co_{70}Fe_{30}$ again grows in a $[-111]$ phase.

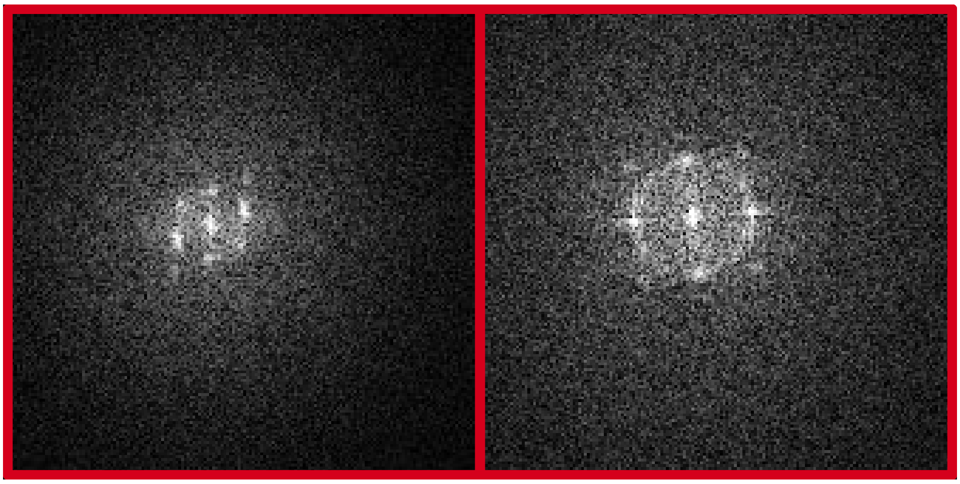

Figure 3.21 – Examples of the Fourier transform of the two ferromagnetic layers of the top artificial antiferromagnet and electrode. The positions used for the FT are shown in Fig 3.17 **Left**: $Co_{70}Fe_{30}$ **Right**: $Co_{40}Fe_{40}B_{20}$.

This is a possible explanation for the difference in pinning strength of the two configurations. The spin dependent reflection coefficient is the defining parameter of the coupling strength of the artificial antiferromagnet (ferromagnet/ruthenium/ferromagnet). The bottom electrode has a high crystal quality with good matching crystallographic directions ($[-111]$ and $[001]$). In contrast to that the top electrode seems to be the reason of the small coupling strength. The degree of crystallinity is smaller. (This leads to a reduced reflection coefficient and overall weaker pinning.

The two ruthenium layers of the two artificial antiferromagnet are expected to be in same crystal structure as well, because the interlayer exchange coupling in both configurations oscillates with the same period.

3.4 Top pinned TMR stacks

Before the double pinned tunnel junctions can be realized, it has to be mentioned that the pinning of the electrode above the tunneling barrier is possible.

The TMR stack which was used before has a free layer above the tunneling barrier and the bottom electrode is pinned with an artificial antiferromagnet. A measurement of a TMR major loop[1] of this system is shown in Fig. 3.22. The magnetization directions of the three ferromagnetic layers are shown with green arrows. The two electrodes are displayed in grey, the $Co_{70}Fe_{30}$ of the artificial antiferromagnet in red and the tunneling barrier is presented in

---

[1] TMR major loop: The external magnetic field can align the pinned and free electrode. TMR minor loop: The magnetic field is not sufficient to switch the pinned-, but the free electrode

blue. For more clarity the thin ruthenium interlayer is neglected in this picture. In positive field direction the attainable magnetic field is too small, to fully saturate the bottom electrode. Going to negative fields a sharp drop of the resistance around zero magnetic field is observed correlated to the switching of the free layer with a TMR amplitude of approximately 170 %. At high negative fields there is a slight rise in the TMR value. This is correlated to the magnetization reversal of the $Co_{70}Fe_{30}$ of the artificial antiferromagnet. The reversal is a so called "scissoring switching", influencing the bottom electrode via interlayer exchange coupling [60].

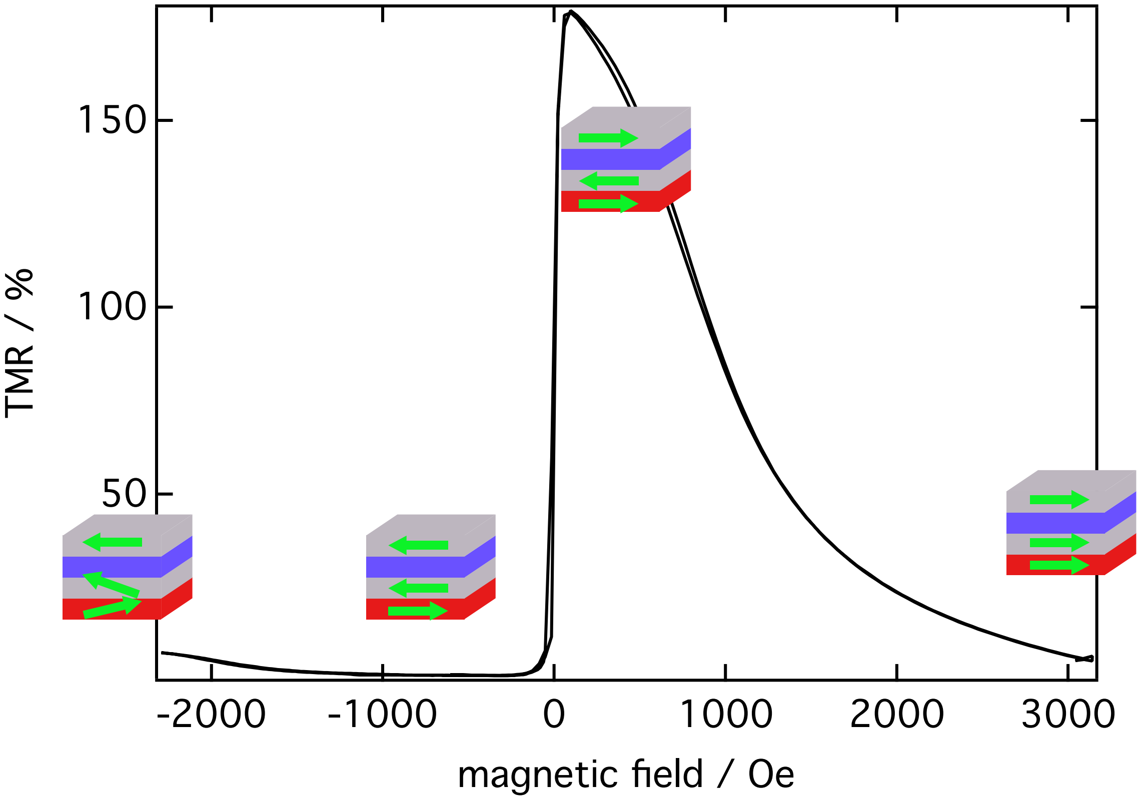

Figure 3.22 – TMR curve of a bottom pinned magnetic tunnel junction. The top electrode is a free layer and bottom pinned by an artificial antiferromagnet. The magnetic field in positive direction cannot fully saturate the bottom layer. At high negative fields a small scissoring effect can be observed [60]. The directions of the electrodes (grey) and $Co_{70}Fe_{30}$ (red) are indicated by green arrows. The tunneling barrier is shown in blue, the thin ruthenium interlayer is not displayed.

The most simple approach to perform a top pinning with $Mn_{83}Ir_{17}$ on $Co_{40}Fe_{40}B_{20}$ is not possible. The reason is that $Mn_{83}Ir_{17}$ will not grow with the desired [111] texture which is beneficial for the exchange bias effect [18]. As an opposite to that $Co_{70}Fe_{30}$ is a suitable underlayer for $Mn_{83}Ir_{17}$. This is why mirroring the existing artificial antiferromagnet is chosen to accomplish the top pinning. A deeper investigation of this pinning method with respect to the bias values is discussed in Chap. 3.2.

The layers of the top pinned TMR stack are (all thicknesses given in nm):

$$\text{Sub}\,/\text{Buffer}/Co_{40}Fe_{40}B_{20}\,(3)/MgO\,(1.7)/$$
$$Co_{40}Fe_{40}B_{20}\,(3)/Ru\,(0.8)/Co_{70}Fe_{30}\,(3)/MnIr\,(7.5)/\text{Capping}$$

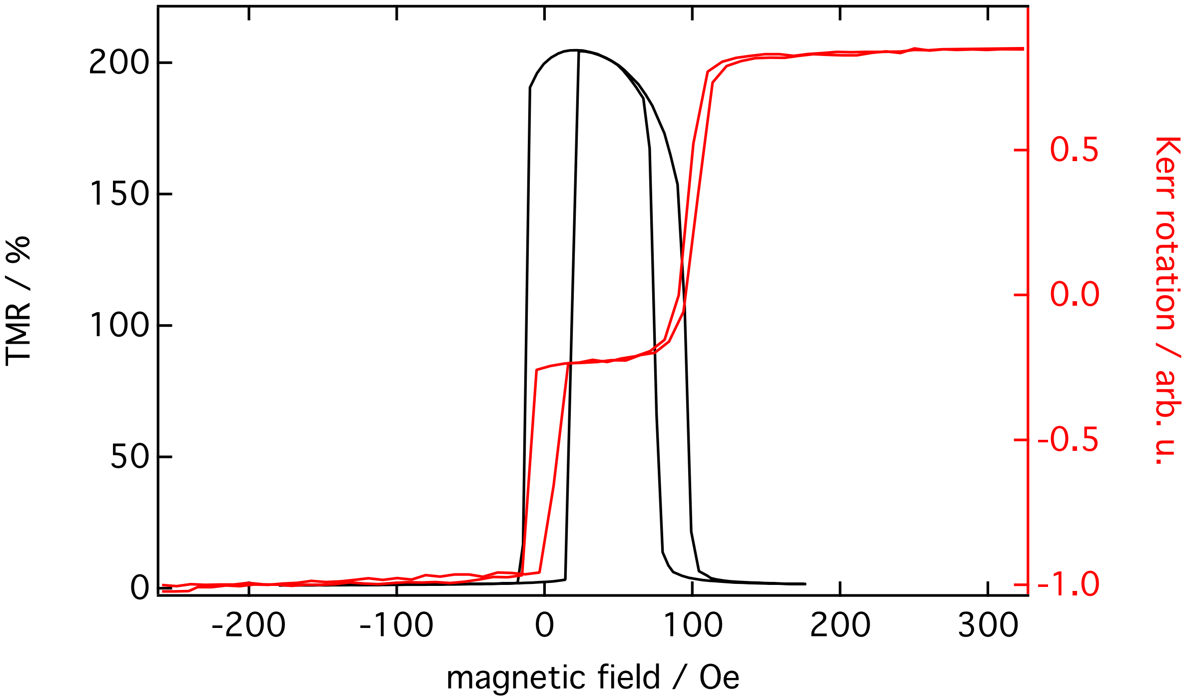

Figure 3.23 – TMR (black) MOKE (red) measurement of the top pinned TMR junction. Only the switching of the two $Co_{40}Fe_{40}B_{20}$ layers are shown. The top electrode has a bias of approximately 100 Oe, the TMR amplitude is 200 %.

Fig. 3.23 shows MOKE and TMR measurements of a top pinned stack. The range of the magnetic field is limited to ±300 Oe which results in only showing the switching of the two $Co_{40}Fe_{40}B_{20}$ electrodes of the TMR junction in order point out this important part more clearly. At bigger negative magnetic fields a third switching which corresponds to the $Co_{70}Fe_{30}$ layer of the artificial antiferromagnet can be observed in the MOKE measurement.

The TMR amplitude is slightly larger than 200 %. One layer is free and switching with zero exchange bias whereas the second switching event is shifted. An apparent difference is the magnitude of the shift. In the bottom configuration the bias at the first coupling maximum is approximately by a factor of 5 larger.

An artificial antiferromagnet seems to be a satisfying possibility pin the top electrode of a magnetic tunnel junction. In a next step the bottom electrode can be pinned as well in order to accomplish the double pinning. The bottom electrode can be pinned with the natural antiferromagnet $Mn_{83}Ir_{17}$ if deposited on a suitable buffer.

3.5 Natural and artificial antiferromagnet

A first system with a double pinning investigated in this work is shown in Fig. 2.12a. The bottom electrode is pinned with the natural antiferromagnet $Mn_{83}Ir_{17}$ and the top electrode with an artificial antiferromagnet. The bias on the top electrode is correlated with the ruthenium interlayer thickness. The blocking temperature of the artificial antiferromagnet depends on the thickness of the $Mn_{83}Ir_{17}$-layer. These two parameters can be controlled independently of each other.

As an opposite to that the blocking temperature and coupling constant are given by the thickness of the $Mn_{83}Ir_{17}$-layer. Investigations on the blocking temperature of $Mn_{83}Ir_{17}$ can be found in Chap. 3.1.2. From these results a pair of $Mn_{83}Ir_{17}$ thicknesses (7.5 nm/20 nm) is chosen with the goal to have different blocking temperatures while providing a high thermal stability.

Annealing series TMR

The two curves in Fig. 3.24 illustrate TMR measurements after the first annealing step. A typical TMR curve (green) is displayed with the difference that both electrodes are biased.

The thickness of the ruthenium interlayer in the AAFM is 0.9 nm, resulting in a negative interlayer exchange coupling constant. As a result the switching field of the upper electrode is shifted towards positive fields. The coercive field (indicated by H_C) of the bottom $Co_{40}Fe_{40}B_{20}$-layer is increased by the exchange interaction.

The exchange bias of the upper electrode is 230 Oe and 140 Oe of the bottom electrode. A TMR measurement of the same sample with a respectively perpendicular magnetic field (direction B) is shown additionally (black). This curve is symmetric with respect to the zero field axis. The external magnetic field “pulls” the magnetization of the two layers along the hard (B) axis. No clear switching can be observed. The TMR amplitude in both directions is comparable, outlining that the same parallel and antiparallel states are reached. The annealing steps are performed as described in Chap. 2.10 with a starting temperature of 120 °C in steps of 20 °C up to 340 °C.

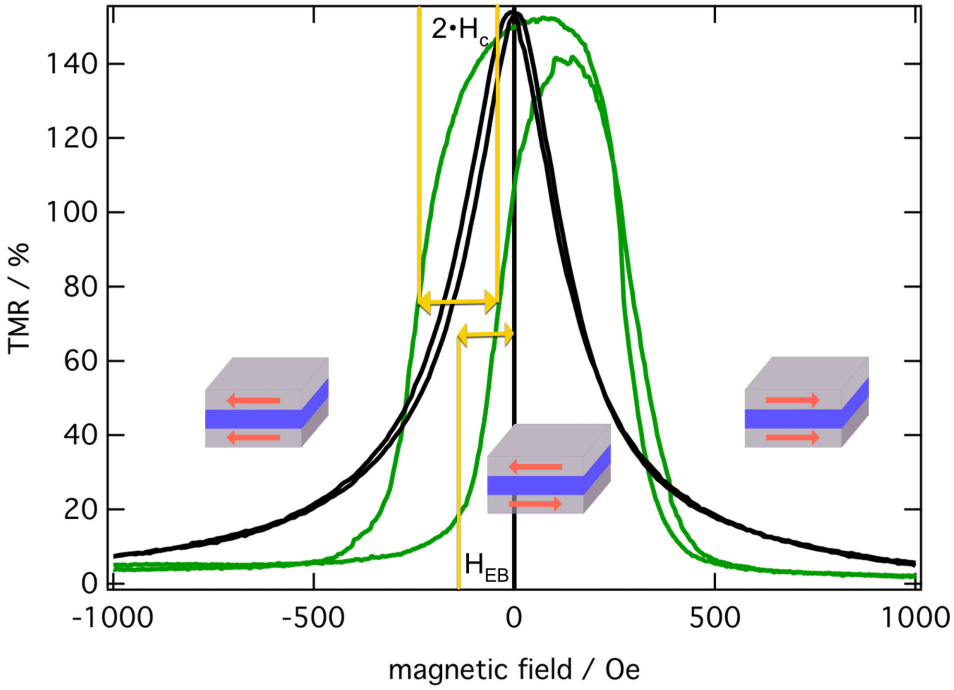

Figure 3.24 – TMR major loops of the samples described in Fig. 2.12a with the magnetic field sweeping in different directions after the first annealing for 60 min at 360 ° C. The green curve shows a measurement in direction A and the black one in direction B. In the green curve the influence on both of the $Co_{40}Fe_{40}B_{20}$ layers can be observed due to the exchange bias. The black curve shows a measurement in the hard direction of both $Co_{40}Fe_{40}B_{20}$ layers. The increased coercive field H_C and exchange bias H_{EB} which occur by pinning with a natural antiferromagnet like $Mn_{83}Ir_{17}$ are highlighted in yellow.

After each annealing step TMR measurements in the A and B direction are performed. Fig. 3.25 and display a selection of these measurements. These measurements reflect the sensitivity with respect to an external magnetic field. A high field sensitivity is expected to translate in a high strain sensitivity.

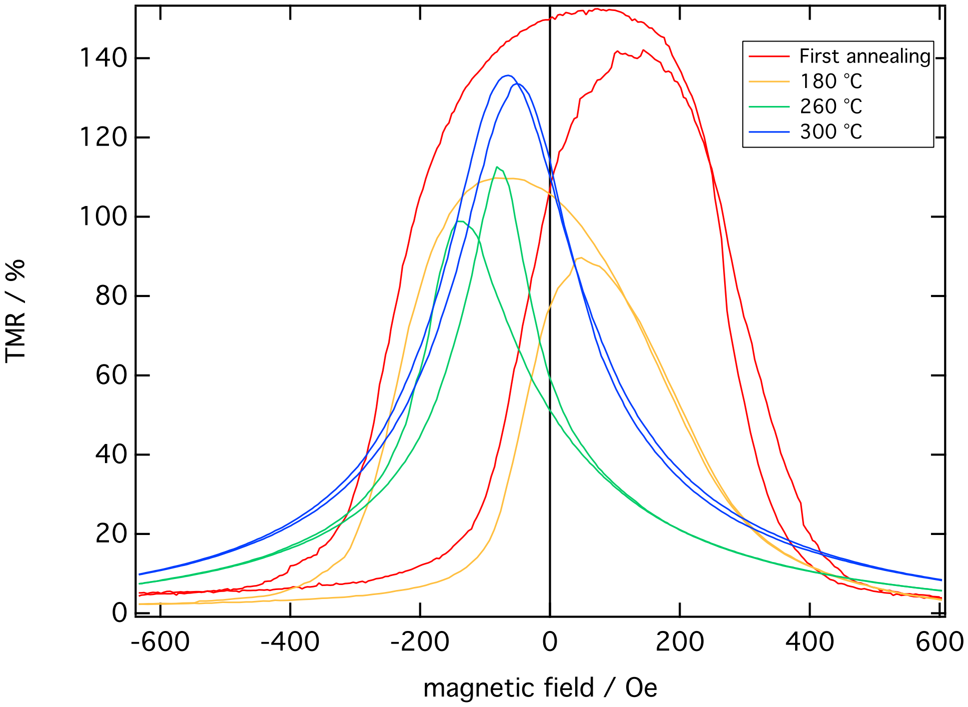

Figure 3.25 – TMR major loops after the first annealing step and after three different temperatures of the second annealing. Only the temperatures 180 °C, 260 °C and 300 °C are shown. The field is sweeping in direction A. A difference of the influence of increasing temperature on the the two magnetization reversal events can be observed.

The TMR measurement after the first annealing step in Fig. 3.25 is the same as the green drawn in Fig. 3.24. The two switching events of the two electrodes have a small overlap.

After a second annealing step at 180 °C (displayed in yellow) a reduction in TMR amplitude can be observed. The reason is that the antiparallel state can not be reached. A decreased bias of the top electrode indicates a started rotation of the pinning direction. When looking at the magnetization reversal of the bottom electrode a completely different observation can be made. There is almost no change in the bias of the bottom electrode in terms of exchange bias and coercivity. When increasing the temperature of the second annealing step to 260 °C (green) the bottom electrode seems to be fully rotated. On the positive flank of the TMR curve the magnetization of the upper electrode is slowly forced to align with the magnetic field, indicating that a perpendicular ground state of the top and bottom electrode is achieved. The shape of the magnetization reversal of the bottom electrode has changed as well, but mostly remains in its initial direction.

The TMR amplitude is lowered to approximately 110 %. This is in agreement with the investigation on the blocking temperature in Chap. 3.1.2. The sample with a $Mn_{83}Ir_{17}$ thickness of 8 nm changes its exchange bias direction at a temperature of approximately 270 °C. This result is compatible with the TMR measurements. Further increasing the temperature leads to an alignment of the pinning direction of the bottom electrode with the external magnetic field.

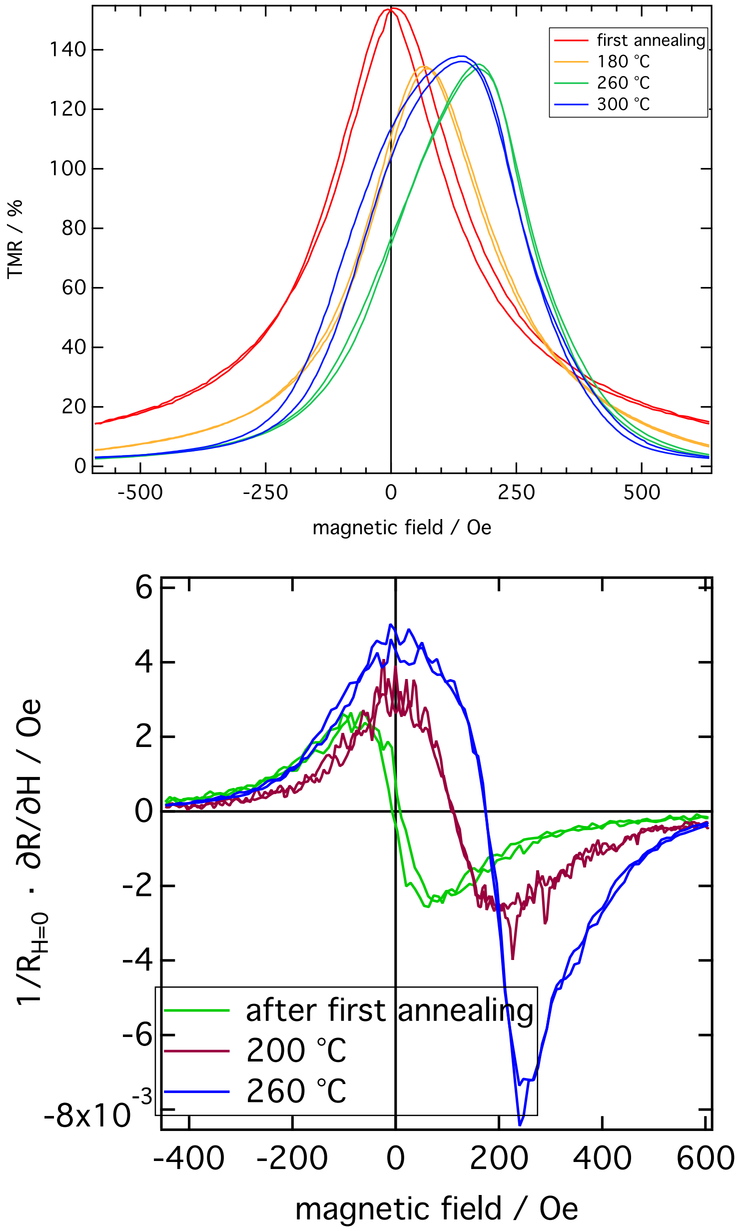

Figure 3.26 – **Top**: TMR major loops comparable to Fig. 3.25. The direction of the external magnetic field is B. **Bottom**: Derivative of the resistance with respect to the external magnetic field divided by the resistance at zero field. Field sweeping in direction B.

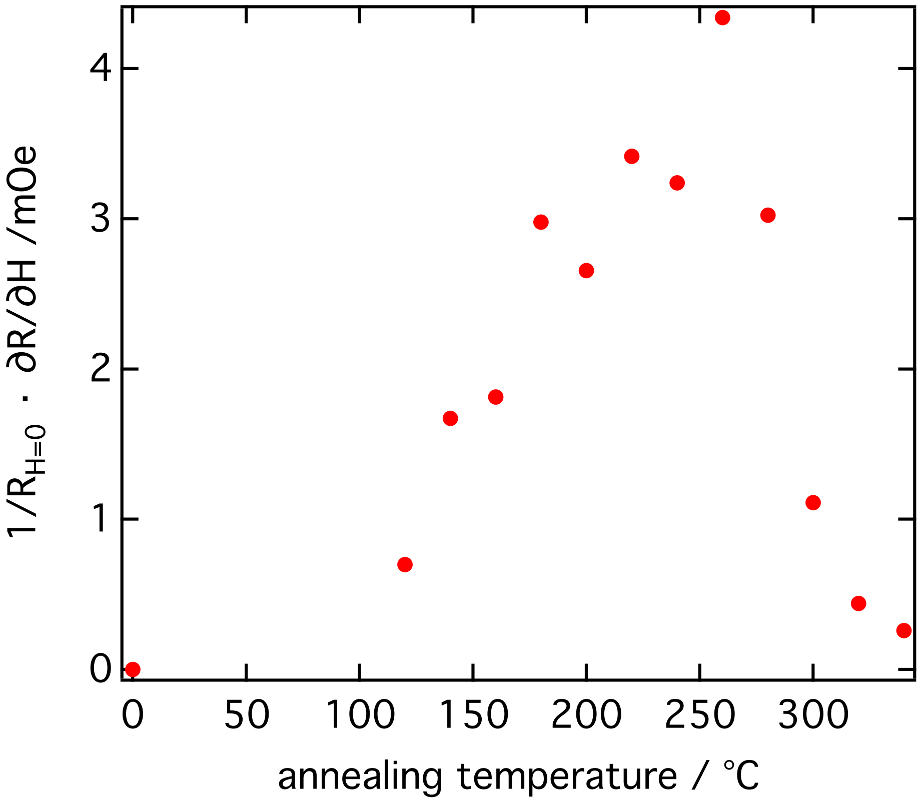

Figure 3.27 – Derivative of the resistance at zero field with respect to temperature of the second annealing process, normalized to the resistance at zero field. The data is comparable to Fig. 3.26. These values are the sensitivity to an external magnetic field. The highest sensitivity is reached at a temperature of 260 °C.

Inverse magnetostriction

The ability of these sensors to measure and distinguish tensile and compressive stress is performed in the bending apparatus which is described in Chap. 2.8. The goal is to measure the influence of compressive and tensile stress in the absence of an external magnetic field.

The sample is prepared as described in Chap. 3.5, the temperature of the second annealing step is 260 °C . Several TMR major loops are performed (magnetic field direction: B). During each measurement a constant mechanical stress of different sign and magnitudes is applied.

The results of these measurements are shown in Fig. 3.29. The influence of tensile stress is displayed in orange and compressive stress in blue. The magnetization and stress directions after the second annealing step are illustrated in Fig. 3.28.

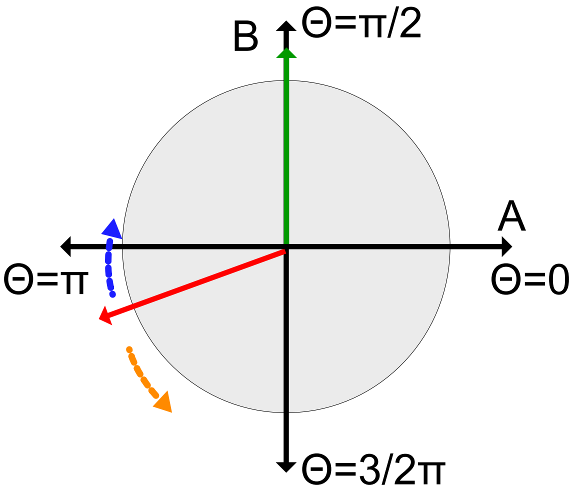

Figure 3.28 – Magnetic configuration of the sample with a natural and artificial antiferromagnet pinning. The angle ϑ is given with respect to the direction of the magnetization after the first annealing step. The magnetization of the reference layer is shown in green and the sense layer is displayed in red. The stress axis is along direction B. The influence on the magnetization direction on the sense layer is indicated by the orange and blue arrows.

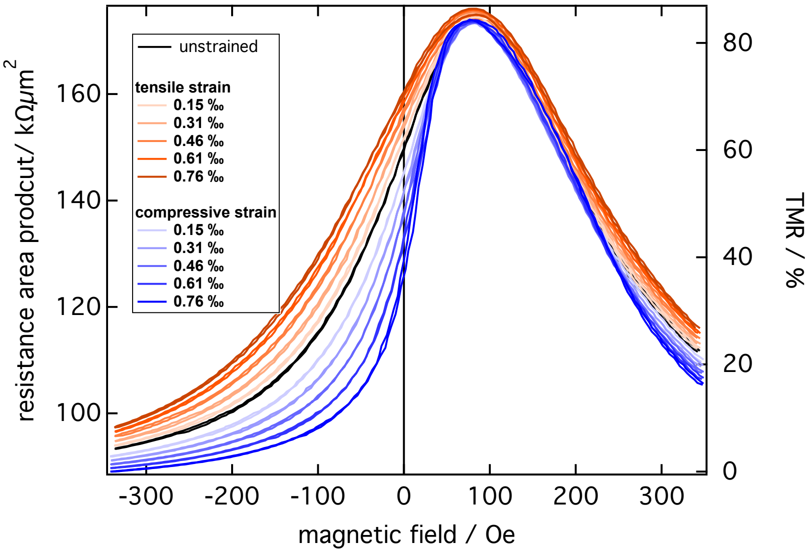

Figure 3.29 – TMR major loops of a natural/artificial antiferromagnet cross pinned after a second annealing step of 260 °C. A constant tensile or compressive stress of different magnitudes is applied during the field loop. The field direction is B.

A clear impact of the stress on the TMR curve can be observed. Starting from a strainless (black) measurement tensile stress increases the resistance during the complete TMR loop. Fig. 2.18a depicts that tensile stress forces the magnetization of the sense layer along the

B axis, resulting in a larger angle between the two magnetizations. At an external magnetic field of 80 Oe the angle between the two magnetizations is closer to 180 ° compared with the unstrained state.

Compressive stress along the B axis induces an anisotropy parallel to the A axis. With respect to the angle notation of Fig. 2.18a the magnetization of the sense layer is rotated counterclockwise. This reduces the angle between the two magnetizations, resulting in a lower electric resistance. The application of compressive stress leads to a higher magnitude of resistance change compared to tensile stress.

The final measurement on this sample is the application of tensile and compressive stress without any external magnetic field.

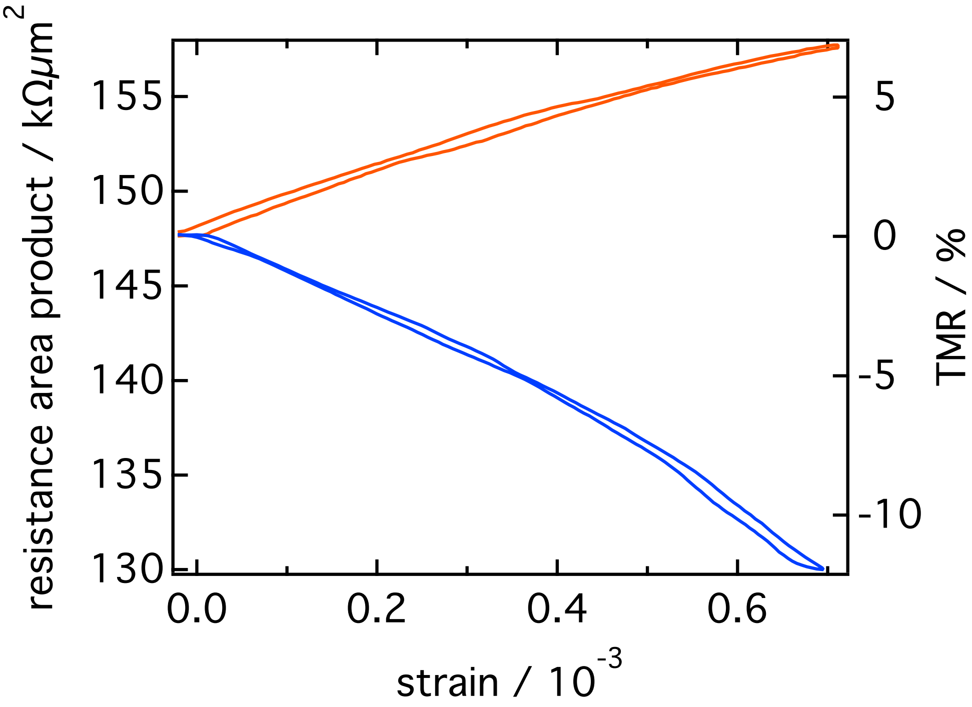

Figure 3.30 – Resistance measurements taken while applying stress with different signs. The red curve shows the influence of tensile stress and the black one of compressive stress.

A hysteresis free inverse magnetostrictive measurement (Fig. 3.30) can be observed with a linear relation between strain and resistance. The maximum relative change in resistance is approximately 10 %. This correlates to an equivalent magnetic field of about 20 Oe. This is comparable to the coercive field of a 3 nm $Co_{40}Fe_{40}B_{20}$-layer. A linear fit (strain: $0-0.3\times 10^{-3}$) gives the follow gauge factors:

$$GF_{comp} = -132\pm3$$

$$GF_{tensile} = 115 \pm 4$$

These values are in the same order of magnitude, but with different signs, which is anticipated. These values show that the basic concept of cross pinned TMR junctions as sensors for mechanical stress works out. The magnitude of the gauge factors has to be increased for a practical application.

3.6 Double artificial antiferromagnet

A different approach is made in order to achieve higher sensitivities. Up to now the bottom electrode serves as the sensing layer. It is pinned by a natural antiferromagnet. Separating the control of the exchange bias and of the blocking temperature is highly beneficial. A second artificial antiferromagnet is the solution to this task.

The blocking temperature can be adjusted by the thickness of the antiferromagnet while the exchange bias is defined via the interlayer thickness. The sense- and the reference electrodes are changed in comparison to the prior layout. The reason is the different magnitude of top and bottom pinning artificial antiferromagnets (see Chap. 3.2). The bottom pinned artificial antiferromagnets are more appropriate as a reference electrode, because in the first coupling maximum, the induced interlayer exchange coupling is approximately a factor of five stronger.

The first goal is different blocking temperatures. This is realized by the different $Mn_{83}Ir_{17}$ thicknesses of the two artificial antiferromagnets. Following from the results of Chap. 3.5, the same 7.5 nm / 20 nm $Mn_{83}Ir_{17}$ combination is used.

The second goal is a weakly pinned sensing layer, leading to higher gauge factors. The ruthenium interlayer thickness of the bottom AAFM is 0.9 nm. This represents a maximum in coupling strength.

The target bias for the top electrode is 80 Oe (in comparison to the external magnetic field used before, see Ref. [110]). Different interlayer thicknesses can be chosen to achieve this coupling (see Fig. 3.11). As seen in Fig. 3.12, a thicker interlayer leads to a better reproducibility. A thickness of 2 nm is chosen, leading to a bias of approximately 80 Oe.

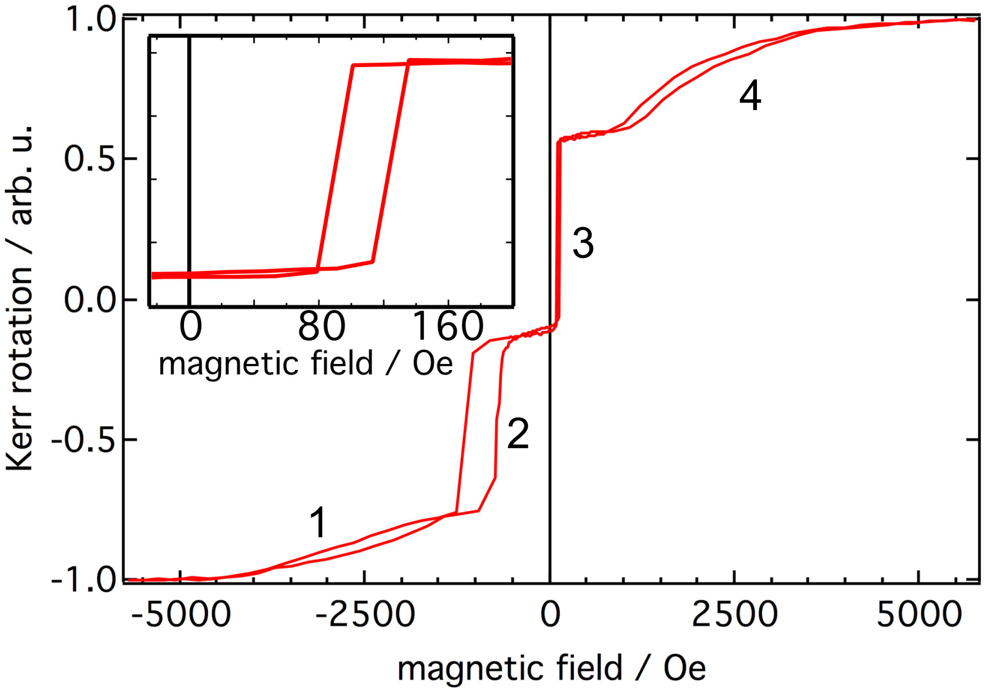

Figure 3.31 – MOKE measurement of the DAAFM system after the first annealing step. Field sweeping in pinning direction (A). The magnetization reversal of the different ferromagnetic layers can be observed. 1: $Co_{70}Fe_{30}$ of bottom AAFM 2: $Co_{70}Fe_{30}$ of upper AAFM 3: $Co_{40}Fe_{40}B_{20}$ above barrier 4: $Co_{40}Fe_{40}B_{20}$ below barrier. The inset shows the switching of the upper $Co_{40}Fe_{40}B_{20}$ layer.

The graph in Fig. 3.31 displays a MOKE measurement of a sample as shown in Fig. 2.12b after the first annealing step. Four distinct magnetization reversals can be observed. The two $Co_{70}Fe_{30}$-layers of the artificial antiferromagnets are pinned via $Mn_{83}Ir_{17}$, therefore the magnetization curve in negative field direction. The interlayer exchange coupling of both artificial antiferromagnets is set to a negative coupling constant. As a result the magnetization of the $Co_{40}Fe_{40}B_{20}$-layers is shifted in positive field direction.

The sensing layer (top) has an exchange bias of 80 Oe, compared to a bias of the reference electrode of 1800 Oe, resulting a difference of a factor of approximately 23. These are good perquisites for a sensor with a higher sensitivity.

TMR measurements

With the results of Chap. 3.5, the same two annealing steps have been performed. The first annealing at a temperature of 360 °C (field direction A) and a second at 260 °C (field direction B).

The red curve in Fig. 3.32 illustrates a minor loop after the first annealing step with the magnetic field sweeping along the A axis. Only the switching of the top (sensing) $Co_{40}Fe_{40}B_{20}$-layer can be observed because the setup cannot provide a field strength higher than 3300 Oe. This is not enough to overcome the pinning of the bottom (reference) electrode. The sharp switching of the reference electrode at 80 Oe and the 160 % of TMR amplitude are best conditions for an increased sensitivity. The TMR measurement after the second annealing step at 260 °C is shown in black. The TMR amplitude is lowered to 115 %. In comparison to Chap. 3.5 the state of two antiparallel magnetizations cannot be obtained anymore. Repeating the first annealing step at 360 °C in direction A restores the initial TMR curve. The derivative (blue) of the resistance after the second annealing step shows a sharp peak at zero magnetic field.

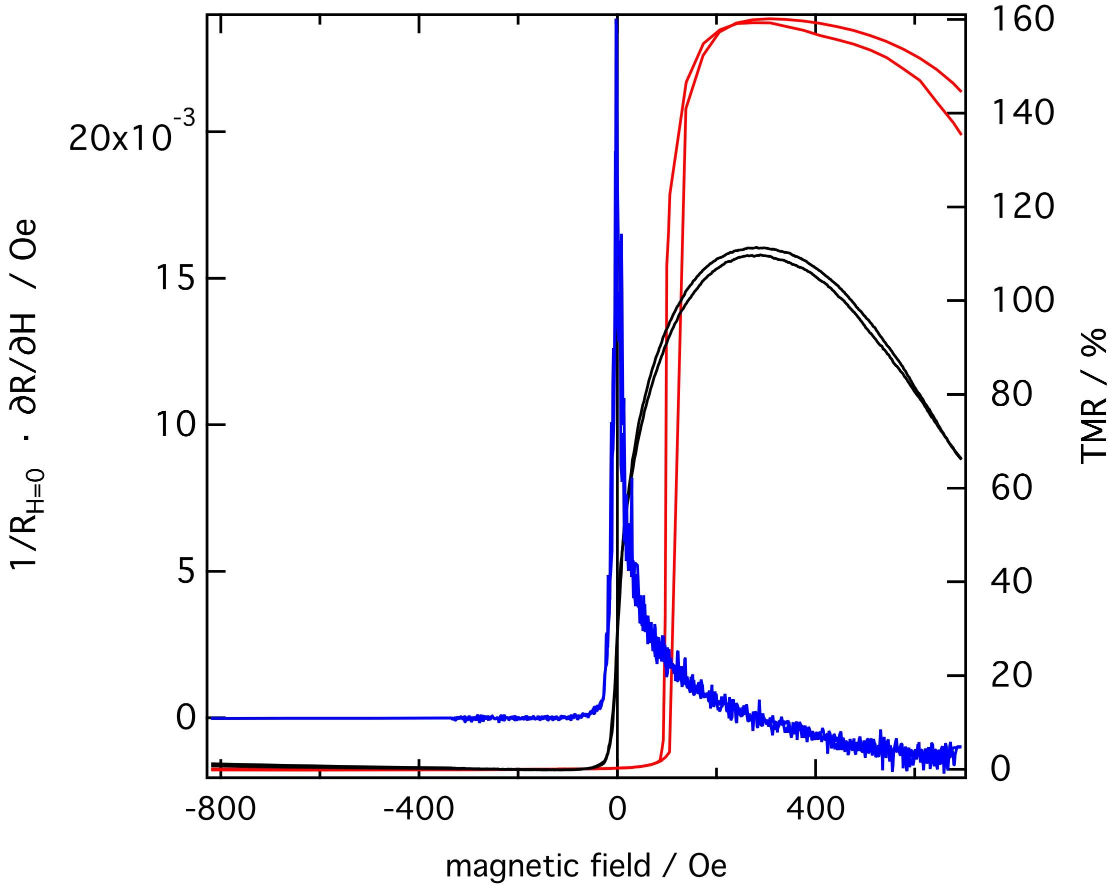

Figure 3.32 – **Red**: TMR minor curve of a double pinned TMR junction with two artificial antiferromagnets after the first annealing step. The pinning is tuned to a bias of 80 Oe. The magnetic field is sweeping in the exchange bias direction. **Blue**: Derivative of the resistance after the first annealing step (red) with respect to the resistance at zero field after a second annealing step at 260 °C. **Black**: TMR minor curve after the second annealing step at 260 °C with a reduced TMR amplitude to 110 %.

The difference in the magnetization reversal characteristics between the electrodes pinned by a natural and a soft tuned artificial antiferromagnet are illustrated in Fig. 3.33. The derivatives of the resistance, normalized to the resistance at zero field, after a second annealing step at 260 °C are shown for the natural/artificial (red) and the double artificial antiferromagnet (blue) TMR stacks. The optimized sensor (double artificial antiferromagnet) has a five times higher sensitivity to an external magnetic field.

The drawback is an earlier saturation of the sensor. This is not expected to be a problem for application in an atomic force microscope. The advantage of controlling the exchange bias separated from the blocking temperature in an artificial antiferromagnet opens up the opportunity to tailor the exact specifications of the sensor for the requirements in its application.

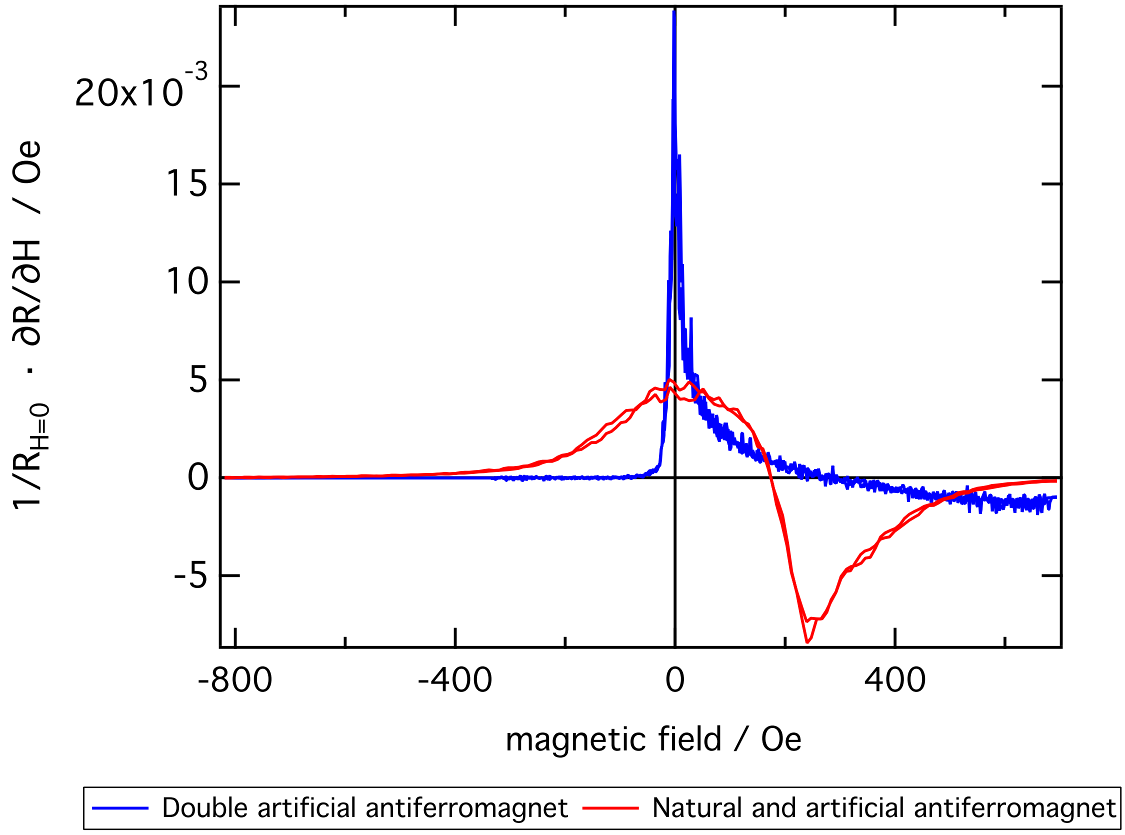

Figure 3.33 – Comparison of the two double pinned TMR sensors after a second annealing step at 260 °C, pointing out the differences in sensitivity and saturation. **Red**: Pinning via artificial and natural antiferromagnet. **Blue**: Double artificial antiferromagnet pinning.

As mentioned in Chap. 1.3 the exchange bias induced by an antiferromagnet may underly a training effect. Since both electrodes are pinned by an artificial antiferromagnet, a change in the bias for the electrodes is not expected, since a slight change in the exchange bias of the natural antiferromagnet does not change the amplitude of the interlayer exchange coupling.

A series of 28 consecutive TMR loops is performed with the goal to investigate a possible change in bias or TMR amplitude. For this might affect the sensitivity of the final sensor. Only a minor change of the TMR amplitude of 2 % after the first 14 repeats can be observed (see Fig. 3.34). The bias of the top (sensing) electrode remains unchanged. A possible explanation for this behavior is a heating of the specimen during the measuring process. The created phonons reduce the TMR amplitude during the measurement.

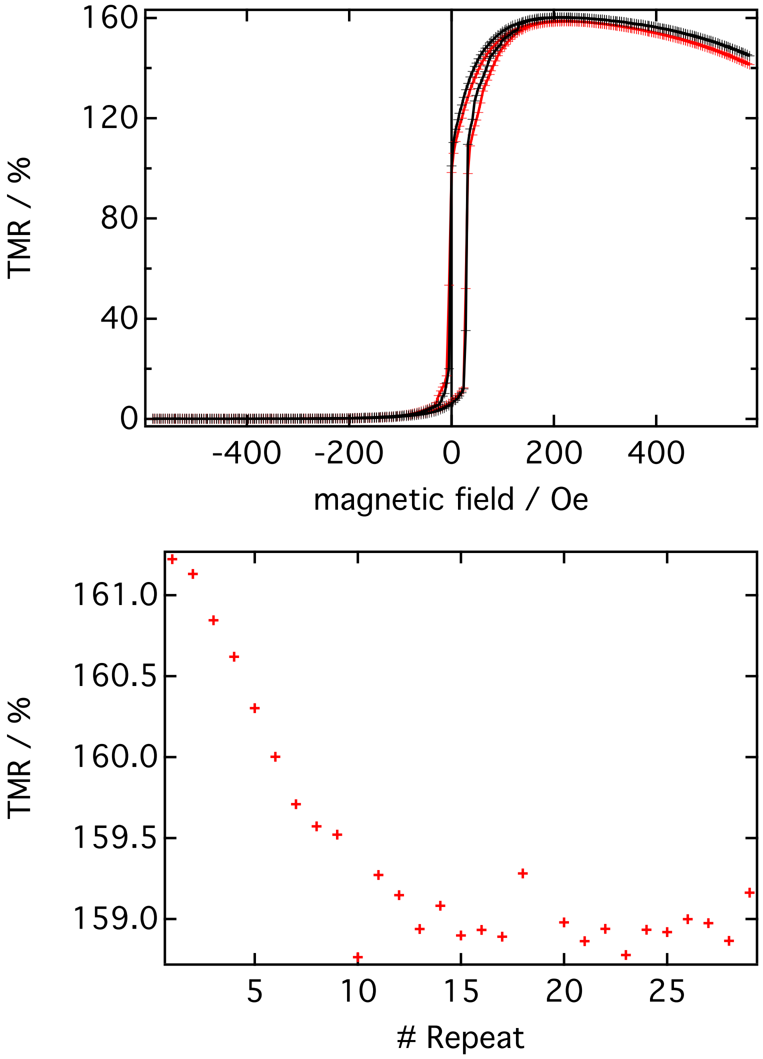

Figure 3.34 – Top: Two TMR minor loops of a double artificial antiferromagnet sample after the first annealing step. The first and ninth measurement are displayed Bottom: TMR amplitude of the same sample for 28 consecutive measurements. After 14 repeats the decline of the TMR amplitude is saturated.

Inverse magnetostriction double artificial antiferromagnet

The final magnetostrictive measurements are taken on samples as described in Fig. 3.32. The bias after the first annealing step is 80 Oe with a second annealing step at 260 °C. Without an external magnetic field, tensile and compressive stress are applied. The directions of the magnetizations and the stress are shown in Fig. 3.35.

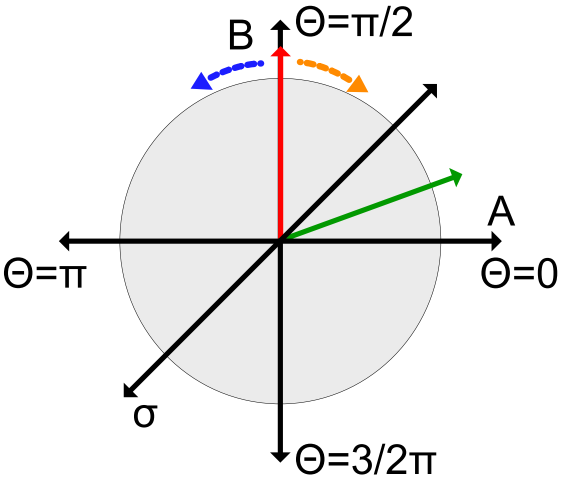

Figure 3.35 – Magnetic configurations of the double artificial antiferromagnet sample. The angle ϑ is given with respect to the direction of the magnetic field during the first annealing step. The magnetization of the reference layer is shown in green while the sense layer is displayed in red. The stress axis σ is at a $\pi/4$ angle between directions A and B. The influence on the magnetization direction on the sense layer is indicated by the orange (compressive) and blue (tensile) arrows.

The results of these measurements are shown in Fig. 3.36.

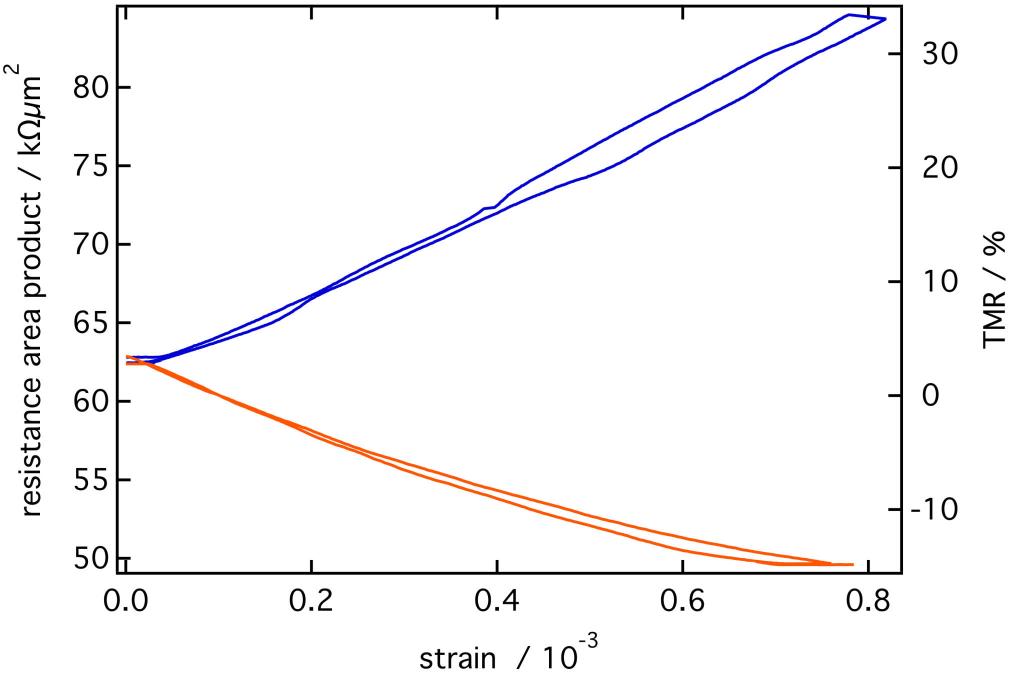

Figure 3.36 – Magnetostrictive measurements of a TMR sample with two artificial antiferromagnets after a second annealing step of 260 °C. Compressive stress leads to decreased electric resistance, whereas it is increased by tensile stress as delineated in Fig. 3.35.

A linear fit in the low strain region ($0 - 0.3 \times 10^{-3}$) results in the following gauge factors ($GF = \frac{\Delta R/R}{\varepsilon}$):

$$GF_{tensile} = -280 \pm 4$$

$$GF_{comp} = 390 \pm 3$$

In comparison to the results of Chap. 3.5, the signs of the gauge factors are exchanged. This change can be explained by taking into account the magnetization directions of the two different sensors after the second annealing step. The magnetization directions of both sensors after the second annealing step are shown in Fig. 3.37.

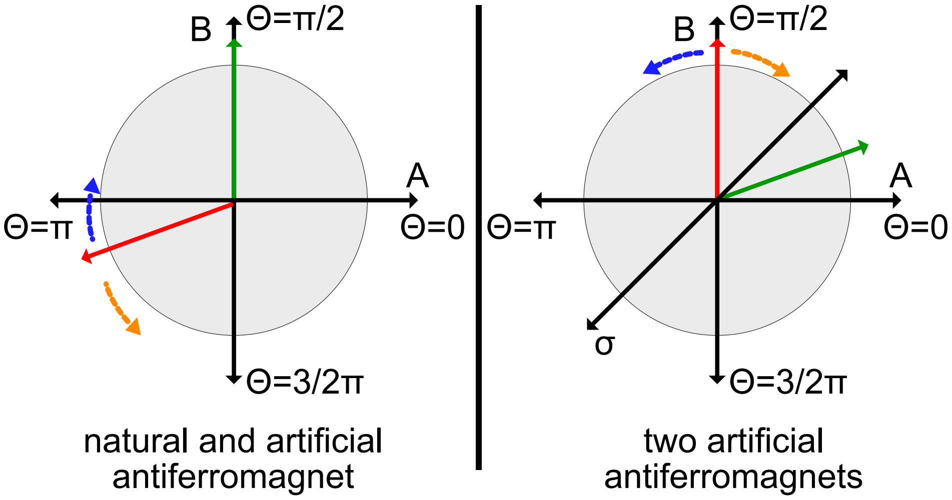

Figure 3.37 – Magnetic configuration of both sensor types. Left: Natural and artificial antiferromagnet. Right: Double artificial antiferromagnet. The influence on the magnetization direction on the sense layer is indicated by the orange and blue arrows.

The stress direction after the second annealing step for the natural/artificial antiferromagnet sample is along direction B ($\theta = \pi/2$), for the double artificial antiferromagnet sample between direction A and B ($\theta = \pi/4$). The induced magnetic anisotropies by the inverse magnetostriction are drawn in blue (compressive) and orange (tensile). The change of the angle between the two electrodes magnetizations has a different sign, resulting in a different sign of the gauge factors.

The second difference that stands out is the higher amplitude. The reason is that the pinning of the sense layer is weaker for the double artificial antiferromagnet than for the natural and artificial antiferromagnet. At full strain applied a change of up to 33 % of the resistance is achieved. Further decreasing of the pinning of the sensing electrode and optimized angles could increase these values even further.

These results open up the possibility for an integration of these sensors in application.

Chapter 4

Conclusion and outlook

New inverse magnetostrictive sensors which are independent of an external magnetic field are developed. These sensors are based on CoFeB/MgO/CoFeB tunnel junctions. These TMR systems need a non collinear magnetic ground state in order to be able to distinguish between compressive and tensile stress. To reach this goal the characteristics of different pinning methods of the two electrodes have been investigated. The pinning is always based on the exchange bias which is induced by the natural antiferromagnet $Mn_{83}Ir_{17}$. By choosing different thicknesses of the antiferromagnetic layers it is possible to achieve different blocking temperatures.

It is not possible to achieve the desired $[111]$ crystal direction of the MnIr layer for exchange bias when deposited on CoFeB without an in-situ annealing process. This is why the pinning of the top electrode has to be realized by an artificial antiferromagnet. The pinning strength of this system can be set by the thickness of the ruthenium interlayer. The top and bottom configuration show the same blocking temperature which is a result of the same crystal quality of the antiferromagnetic layer.

The coupling strength differs a lot if the top or bottom pinning configuration is used. A possible origin is determined by transmission electron microscopy of thin lamellas. To achieve a high TMR amplitude of CoFeB/MgO/CoFeB tunnel junction requires a post annealing process after the sputtering deposition. In this process the CoFeB layer crystallizes into cubic CoFe which results in a high TMR amplitude. Depending on the neighboring layers the CoFe layer will crystallize in different phases. Below the tunneling barrier (deposited on ruthenium) the $[-111]$ and $[001]$ phases, whereas on top of the MgO tunneling barrier the crystal quality was much worse with some $[001]$ crystallites. The different degrees of crystal quality result in different reflection parameters in the quantum well of the artificial antiferromagnet. The influence of different crystallographic directions ($[-111]$ and $[001]$) have to be investigated in the future.

Starting from these results double pinned TMR junctions are prepared. The bottom pinning is realized by a 20 nm thick MnIr layer. As a result the blocking temperature is high (T_B~270 °C). The top pinning includes 7.5 nm of $Mn_{83}Ir_{17}$ leading to a low blocking temperature (T_B~200 °C). After a series of consecutive annealing steps the thermal treatment for the highest sensitivity with respect to an external magnetic field is found to be 260 °C. In a four point bending apparatus inverse magnetostrictive measurements are performed on circular shaped tunnel junctions. These system has the gauge factors: $GF_{comp} = -132 \pm 3$ and $GF_{tens} = 115 \pm 4$ without an external magnetic field.

The improved sensor has a pinning with an artificial antiferromagnet on both electrodes. Because the pinning of the artificial antiferromagnet on the top electrode is about 5 times weaker it is chosen to be the sensing layer. Via the interlayer exchange coupling it can be easily tuned to a lower value than the 80 Oe used in this work.. This separation of magnetic bias and blocking temperature is very powerful. It allows to create sensors with any desired pinning strength in any direction. By weakening the bias of the sensing layer, the gauge factors increase to $GF_{comp} = 390 \pm 3$ and $GF_{tens} = -280 \pm 4$.

There are several ways to achieve an increased sensitivity of this kind of sensors. As seen in prior measurements decreasing the magnetic bias from 200 Oe to 80 Oe increase the sensitivity by a factor of almost 3. A further decrease is easily possible by adjusting the interlayer exchange coupling. The environment in which the sensor will operate has to be taken into account. A magnetic field will influence the magnetization direction of the sense layer leading to incorrect measurements. The bias has to be chosen with the application in mind. A second parameter which can enhance the performance is the angle between the magnetizations. The angle of the best performance is $105 - 110°$ [109]. Angle dependent magnetization measurements might lead to better blocking temperature / field cooling combinations to fulfill this specification. With further increased sensitivity the TMR based sensors are a viable alternative to the current optical readout system. An integration into other applications like nano 3D printing, bio sensing applications or as integrated field sensors is also possible.

After increasing the sensitivity and implementing these sensors in new kinds of atomic force microscopes, the perfect sensor for several new applications can be designed.

Publications

- Niklas Dohmeier, Ali Tavassolizadeh, Karsten Rott, Eckhard Quandt, Dirk Meyners, and Günter Reiss “Inverse magnetostrictive stress sensors based on crossed pinned CoFeB/MgO/CoFeB tunnel junctions” Journal of Applied Physics, 124 (6):064501, 2018
- Alessia Niesen, Niclas Teichert, Tristan Matalla-Wagner, Jan Balluf, Niklas Dohmeier, Manuel Glas, Christoph Klewe, Elke Arenholz, Jan-Michael Schmalhorst, and Günter Reiss “Structural, magnetic, and electrical properties of perpendicularly magnetized $Mn_{4-X}Fe_XGe$ thin films”, Journal of Applied Physics, 123(11):113901 (2018)

Conferences

- Niklas Dohmeier, Günter Reiss, Karsten Rott, Ali Tavassolizadeh, Dirk Meyners and Eckhard Quandt “Investigation on new TMR stacks for inverse magnetrostrictive sensors”, DPG Spring meeting 2016, Regensburg
- Niklas Dohmeier, Günter Reiss, Karsten Rott, Ali Tavassolizadeh and Dirk Meyners “Inverse magnetostrictive stress sensors based on CoFeB/MgO/CoFeB tunnel junctions”, DPG Spring meeting 2017 Dresden

References

[1] M Ali and R Watts. Measurement of saturation magnetostriction using novel strained substrate techniques and the control of the magnetic anisotropy. *Journal of Magnetism and Magnetic Materials*, 202(1):85 – 94, 1999. ISSN 0304-8853.

[2] M. Ali, C. H. Marrows, M. Al-Jawad, and B. J. Hickey. Antiferromagnetic layer thickness dependence of the irmn/co exchange bias system. *Physical review. B*, 2003.

[3] T. Ambrose and C. L. Chien. Dependence of exchange coupling on antiferromagnetic layer thickness in nife/coo bilayers. *Journal of Applied Physics*, 83(11):6822–6824, 1998. doi: 10.1063/1.367863.

[4] Geoff Anderson, Yiming Huai, and Lena Miloslawsky. Cofe/irmn exchange biased top, bottom, and dual spin valves. *Journal of Applied Physics*, 87(9):6989–6991, 2000. doi: 10.1063/1.372907.

[5] M. N. Baibich, J. M. Broto, A. Fert, F. Nguyen Van Dau, F. Petroff, P. Etienne, G. Creuzet, A. Friederich, and J. Chazelas. Giant magnetoresistance of (001)fe/(001)cr magnetic superlattices. *Phys. Rev. Lett.*, 61(21):2472–2475, 1988.

[6] V. Baltz, J. Sort, S. Landis, B. Rodmacq, and B. Dieny. Tailoring Size Effects on the Exchange Bias in Ferromagnetic-Antiferromagnetic < 100 nm Nanostructures. *Phys. Rev. Lett.*, 94(11):117201, 2005.

[7] Lydia Baril, Bruce Gurney, Dennis Wilhoit, and V. Speriosu. Magnetostriction in spin valves. *Journal of Applied Physics*, 85(8):5139–5141, 1999. doi: 10.1063/1.369103.

[8] Robert S. Beach, Mustafa Pinarbasi, and Matthew J. Carey. Ap-pinned spin valve gmr and magnetization. *Journal of Applied Physics*, 87(9):5723–5725, 2000.

[9] G. Binasch, P. Grünberg, F. Saurenbach, and W. Zinn. Enhanced magnetoresistance in layered magnetic structures with antiferromagnetic interlayer exchange. *Phys. Rev. B*, 39:4828–4830, Mar 1989. doi: 10.1103/PhysRevB.39.4828.

[10] W. F. Brinkman, R. C. Dynes, and J. M. Rowell. Tunneling conductance of asymmetrical barriers. *Journal of Applied Physics*, 41(5):1915–1921, 1970.

[11] P. Bruno. Oscillations of interlayer exchange coupling vs. ferromagnetic-layers thickness. *EPL (Europhysics Letters)*, 23(8):615, 1993.

[12] P. Bruno. Theory of interlayer exchange interactions in magnetic multilayers. *J. Phys.: Condens. Matter*, 11:9403–9419, 1999.

[13] P. Bruno and C. Chappert. Ruderman-kittel theory of oscillatory interlayer exchange coupling. *Phys. Rev. B*, 46:261–270, Jul 1992.

[14] W. H. Butler, X.-G. Zhang, T. C. Schulthess, and J. M. MacLaren. Spin-dependent tunneling conductance of fe|mgo|fe sandwiches. *Phys. Rev. B*, 63:054416, Jan 2001. doi: 10.1103/PhysRevB.63.054416.

[15] William H. Butler. Tunneling magnetoresistance from a symmetry filtering effect. *Sci. Technol. Adv. Mater.*, 9(1), 2008.

[16] B. Cappella and G. Dietler. Force-distance curves by atomic force microscopy. *Surface Science Reports*, 34(1):1 – 104, 1999. ISSN 0167-5729.

[17] C. Carbone, E. Vescovo, O. Rader, W. Gudat, and W. Eberhardt. Exchange split quantum well states of a noble metal film on a magnetic substrate. *Phys. Rev. Lett.*, 71: 2805–2808, Oct 1993.

[18] I. L. Castro, V. P. Nascimento, E. C. Passamani, A. Y. Takeuchi, C. Larica, M. Tafur, and F. Pelegrini. The role of the (111) texture on the exchange bias and interlayer coupling effects observed in sputtered nife/irmn/co trilayers. *Journal of Applied Physics*, 113 (20):203903, 2013.

[19] C. Chappert and J. P. Renard. Long-period oscillating interactions between ferromagnetic layers separated by a nonmagnetic metal: a simple physical picture. *EPL (Europhysics Letters)*, 15(5):553, 1991.

[20] V. Chaudhary and R. V. Ramanujan. Magnetocaloric properties of fe-ni-cr nanoparticles for active cooling. *Scientific Reports*, 6:35156 EP –, 10 2016.

[21] A. E. Clark, K. B. Hathaway, M. Wun-Fogle, T.A. Restorff, V.M. Keppens, G. Petculescu, and R.A. Taylor. Extraordinary magnetoelasticity and lattice softening in bcc fe-ga alloys. *J. Appl. Phys.*, 93(10):8621, 2003.

[22] J . M. D. Coey. *Magnetism and Magnetic Materials*. CAMBRIDGE UNIVERSITY PRESS, 2010.

[23] M.D. Cooke, L.C. Wang, R. Watts, R. Zuberek, G. Heydon, W. M. Rainforth, and G. A. Gehring. The effect of thermal treatment, composition and substrate on the texture and magnetic properties of feco thin films. *J. Phys. D Appl. Phys*, 3(12):1450, 2000.

[24] B. D. Cullity and C. D. Graham. *Introduction to Magnetic Materials*, volume 2. Wiley, 2009.

[25] B. D. Cullity and C. D. Graham. *Introduction to magnetic materials*. second edition. WILEY, New Jersey, 2009.

[26] A. J. Devasahayam and M. H. Kryder. The dependence of the antiferromagnet/ferromagnet blocking temperature on antiferromagnet thickness and deposition conditions. *J. Appl. Phys*, 85(8):5519–5521, 1999.

[27] Z. Diao, D. Apalkov, M. Pakala, Y. Ding, Al. Panchula, and Y. Huai. Spin transfer switching and spin polarization in magnetic tunnel junctions with MgO and AlO_x barriers. *Applied Physics Letters*, 87(23):232502, 2005.

[28] David D. Djayaprawira, Koji Tsunekawa, Motonobu Nagai, Hiroki Maehara, Shinji Yamagata, Naoki Watanabe, Shinji Yuasa, Yoshishige Suzuki, and Koji Ando. 230tunnel junctionsmagnetic tunnel junctions. *Applied Physics Letters*, 86(9):092502, 2005.

[29] Volker Drewello. Untersuchung der spinpolarisation von 3d-ferromagneten in mgo tunnelsystemen. Master's thesis, University of Bielefeld, Department of Physics, 2006.

[30] A. Duluard, B. Negulescu, C. Bellouard, M. Hehn, D. Lacour, Y. Lu, G. Lengaigne, F. Montaigne, S. Robert, S. Suire, and C. Tiusan. Fe/mgo/fe (100) textured tunnel junctions exhibiting spin polarization features of single crystal junctions. *Applied Physics Letters*, 100(7):072408, 2012.

[31] M. Dunz, J. Schmalhorst, and M. Meinert. Enhanced exchange bias in mnn/cofe bilayers after high-temperature annealing. *AIP Advances*, 8(5):056304, 2018.

[32] J. W. Edington. *Typical Electron Microscope Investigations*, volume 1. Palgrave, London, 1976.

[33] D. M. Edwards, J. Mathon, R. B. Muniz, and M. S. Phan. Oscillations of the exchange in magnetic multilayers as an analog of de haas–van alphen effect. *Phys. Rev. Lett.*, 67: 493–496, Jul 1991.

[34] T. Egami, C. Graham, W. Dmowski, P. Zhou, P. Flanders, E. Marinero, H. Notarys, and C. Robinson. Anisotropy and coercivity of amorphous re-tm films. *IEEE Transactions on Magnetics*, 23(5):2269–2271, 1987.

[35] T. Eimüller, T. Kato, T. Mizuno, S. Tsunashima, C. Quitmann, T. Ramsvik, S. Iwata, and G. Schütz. Uncompensated spins in a micro-patterned cofeb/mnir exchangebias system. *Applied Physics Letters*, 85(12):2310–2312, 2004.

[36] Hiromi N. Fuke, Kazuhiro Saito, Masatoshi Yoshikawa, Hitoshi Iwasaki, and Masashi Sahashi. Influence of crystal structure and oxygen content on exchange-coupling properties of irmn/cofe spin-valve films. *Applied Physics Letters*, 75(23):3680–3682, 1999.

[37] Hiromi Niu Fuke, Kazuhiro Saito, Yuzo Kamiguchi, Hitoshi Iwasaki, and Masashi Sahashi. Spin-valve giant magnetoresistive films with antiferromagnetic ir-mn layers. *Journal of Applied Physics*, 81(8):4004–4006, 1997.

[38] X. Gao, J. Li, J. Zhu, and M. Zhang. Effect of b and cr on mechanical properties and magnetostriction of iron-gallium ally. *Mater. Trans.*, 50:1959, 2009.

[39] M. González-Guerrero, J. L. Prieto, D. Ciudad, P. Sánchez, and C. Aroca. Engineering the magnetic properties of amorphous (fe80co20)80b20 with multilayers of variable anisotropy direction. *Applied Physics Letters*, 90(16):162501, 2007.

[40] Martin Gottschalk. *Anwendung der Ionen- und Elektronenmikroskopie im Grenzgebiet zwischen Nanostrukturphysik und Biologie*. PhD thesis, University of Bielefeld, 2017.

[41] R Grössinger, R Sato Turtelli, and N Mehmood. Materials with high magnetostriction. *IOP Conference Series: Materials Science and Engineering*, 60(1):012002, 2014.

[42] P. Grünberg, R. Schreiber, Y. Pang, M. B. Brodsky, and H. Sowers. Layered magnetic structures: Evidence for antiferromagnetic coupling of fe layers across cr interlayers. *Phys. Rev. Lett.*, 57:2442–2445, Nov 1986.

[43] P. Grünberg, R. Schreiber, Y. Pang, M. B. Brodsky, and H. Sowers. Layered magnetic structures: Evidence for antiferromagnetic coupling of fe layers across cr interlayers. *Phys. Rev. Lett.*, 57(19):2442–2445, Nov 1986.

[44] Z.B. Guo, B.Y. Zong, J.J. Qiu, P. Luo, L.H. An, H. Meng, G.C. Han, and H.K. Hui. Tuning exchange coupling by replacing cofe with amorphous cofeb in the cofe/ru/cofe synthetic antiferromagnetic structure. *Solid State Communications*, 150(1):45 – 48, 2010.

[45] Xi Haiwen, M. Robert, and M. White. Antiferromagnetic thickness dependence of blocking temperature in exchange coupled polycrystalline ferromagnet/antiferromagnet bilayers. *Journal of Applied Physics*, 92(8), 2002.

[46] J. Hayakawa, S. Ikeda, Y. M. Lee, F. Matsukura, and H. Ohno. Effect of high annealing temperature on giant tunnel magnetoresistance ratio of CoFeB/MgO/CoFeB magnetic tunnel junctions. *Applied Physics Letters*, 89(23):232510, 2006.

[47] Jun Hayakawa, Shoji Ikeda, Fumihiro Matsukura, Hiromasa Takahashi, and Hideo Ohno. Dependence of giant tunnel magnetoresistance of sputtered cofeb/mgo/cofeb magnetic tunnel junctions on mgo barrier thickness and annealing temperature. *Japanese Journal of Applied Physics*, 44(4L):L587, 2005.

[48] David E. Heim and Stuart S. P. Parin. Magnetoresistive spin valve sensor with improved pinned ferromagnetic layer and magnetic recording system using the sensor. US Patent US5465185A, 1995.

[49] B. Heinrich. *Ultrathin Magnetic Structures II*. Springer-Verlag, 1994.

[50] Ulrich Hilleringmann. *Silizium-Halbleitertechnologie: Grundlagen mikroelektronischer Integrationstechnik*, volume 6. Springer Vieweg, 2014.

[51] A. T. Hindmarch, A. W. Rushforth, R. P. Campion, C. H. Marrows, and B. L Gallagher. Origin of in-plane uniaxial magnetic anisotropy in cofeb amorphous ferromagnetic thin films. *Physical review. B*, 83(21):212404, 2011.

[52] M Hosomi, H Yamagishi, T Yamamoto, K Bessho, Y Higo, Kazutaka Yamane, H Yamada, M Shoji, H Hachino, C Fukumoto, H Nagao, and H Kano. A novel nonvolatile memory with spin torque transfer magnetization switching: Spin-ram. volume 2005, pages 459 – 462, 01 2006.

[53] Y. Huai, J. Zhang, G. W. Anderson, P. Rana, S. Funada, C.-Y. Hung, M. Zhao, and S. Tran. Spin-valve heads with synthetic antiferromagnet cofe/ru/cofe/irmn. *Journal of Applied Physics*, 85(8):5528–5530, 1999. doi: 10.1063/1.369883.

[54] Dwight Hunter, Will Osborn, Ke Wang, Nataliya Kazantseva, Jason Hattrick-Simpers, Richard Suchoski, Ryota Takahashi, Marcus L. Young, Apurva Mehta, Leonid A. Bendersky, Sam E. Lofland, Manfred Wuttig, and Ichiro Takeuchi. Giant magnetostriction in annealed $co_{1-x}fe_x$ thin-films. *Nature Communications*, 2:518 EP –, 2011.

[55] S. Ikeda, J. Hayakawa, Y. Ashizawa, Y. M. Lee, K. Miura, H. Hasegawa, M. Tsunoda, F. Matsukura, and H. Ohno. Tunnel magnetoresistance of 604% at 300k by suppression of ta diffusion in CoFeB/MgO/CoFeB pseudo-spin-valves annealed at high temperature. *Applied Physics Letters*, 93(8):082508, 2008.

[56] Shoji Ikeda, Jun Hayakawa, Young Min Lee, Ryutaro Sasaki, Toshiyasu Meguro, Fumihiro Matsukura, and Hideo Ohno. Dependence of tunnel magnetoresistance in mgo based magnetic tunnel junctions on ar pressure during mgo sputtering. *Japanese Journal of Applied Physics*, 44(11L):L1442, 2005.

[57] F. R. J. van Driel, K.-M. H. Lenssen de Boer, and R. Coehoorn. Exchange biasing by $Ir_{19}Mn_{81}$: Dependence on temperature, microstructure and antiferromagnetic layer thickness. *Journal of Applied Physics*, 88(2), 2000.

[58] H. Jaffrès, D. Lacour, F. Nguyen Van Dau, J. Briatico, F. Petroff, and A. Vaurès. Angular dependence of the tunnel magnetoresistance in transition-metal-based junctions. *Phys. Rev. B*, 64:064427, Jul 2001.

[59] S. U. Jena and Y. D. Yao. Magnetic and electrical properties of amorphous cofeb films. *Journal of Applied Physics*, 99(053701), 2006.

[60] Andrew Johnson. *Spin Valve Systems for Angle Sensor Applications*. PhD thesis, Technische Universität Darmstadt, 2004.

[61] J. P. Joule. On a new class of magnetic forces. *Ann. Electr. Magn. Chem.*, 8(219), 1842.

[62] M. Julliere. Tunneling between ferromagnetic films. *Phys. Lett.*, 54A(3):225, 1975.

[63] R. Jungblut, R. Coehoorn, M. T. Johnson, J. aan de Stegge, and A. Reinders. Orientational dependence of the exchange biasing in molecular-beam-epitaxy-grown $Ni_{80}Fe_{20}/Fe_{50}Mn_{50}$ bilayers. *Journal of Applied Physics*, 75(10):6659–6664, 1994.

[64] J. Kanak, P. Wiśniowski, T. Stobiecki, A. Zaleski, W. Powroźnik, S. Cardoso, and P. P. Freitas. X-ray diffraction analysis and monte carlo simulations of cofeb-mgo based magnetic tunnel junctions. *Journal of Applied Physics*, 113(2):023915, 2013.

[65] R. K. Kawakami, E. Rotenberg, Ernesto J. Escorcia-Aparicio, Hyuk J. Choi, T. R. Cummins, J. G. Tobin, N. V. Smith, and Z. Q. Qiu. Observation of the quantum well interference in magnetic nanostructures by photoemission. *Phys. Rev. Lett.*, 80:1754–1757, Feb 1998.

[66] Xeniya Kozina, Siham Ouardi, Benjamin Balke, Gregory Stryganyuk, Gerhard H. Fecher, Claudia Felser, Shoji Ikeda, Hideo Ohno, and Eiji Ikenaga. A nondestructive analysis of the b diffusion in ta–cofeb–mgo–cofeb–ta magnetic tunnel junctions by hard x-ray photoemission. *Applied Physics Letters*, 96(7):072105, 2010.

[67] Hitoshi Kubota, Akio Fukushima, Yuichi Ootani, Shinji Yuasa, Koji Ando, Hiroki Maehara, Koji Tsunekawa, David D. Djayaprawira, Naoki Watanabe, and Yoshishige Suzuki. Evaluation of spin-transfer switching in CoFeB/MgO/CoFeB magnetic tunnel junctions. *Japanese Journal of Applied Physics*, 44(No. 40):L1237–L1240, sep 2005.

[68] Hitoshi Kubota, Akio Fukushima, Kay Yakushiji, Taro Nagahama, Shinji Yuasa, Koji Ando, Hiroki Maehara, Yoshinori Nagamine, Koji Tsunekawa, David D. Djayaprawira, Naoki Watanabe, and Yoshishige Suzuki. Quantitative measurement of voltage dependence of spin-transfer torque in mgo-based magnetic tunnel junctions. *Nature Physics*, 4, 2007.

[69] H. Kurt, K. Rode, K. Oguz, M. Boese, C. C. Faulkner, and J. M. D. Coey. Boron diffusion in magnetic tunnel junctions with MgO (001) barriers and cofeb electrodes. *Applied Physics Letters*, 96(26):262501, 2010.

[70] X. Y. Lang, W. T. Zheng, and Q. Jiang. Dependence of the blocking temperature in exchange biased ferromagnetic/antiferromagnetic bilayers on the thickness of the antiferromagnetic layer. *Nanotechnology*, 18, 2007.

[71] D.J. Larson, E.A. Marquis, P.M. Rice, T.J. Prosa, B.P. Geiser, S.-H. Yang, and S.S.P. Parkin. Manganese diffusion in annealed magnetic tunnel junctions with mgo tunnel barriers. *Scripta Materialia*, 64(7):673 – 676, 2011.

[72] J. L. Leal and M. H. Kryder. Spin valves exchange biased by Co/Ru/Co synthetic antiferromagnets. *Journal of Applied Physics*, 83:3720–3723, 1998.

[73] G.A. Lebedev, B. Viala, T. Lafont, and D.I. Zakharov. Converse magnetoelectric effect dependence with cofeb composition in ferromagnetic/piezoelectric composites. *J. Appl. Phys.*, 111(7):07C725, 2012.

[74] E. W. Lee. Magnetostriction and magnetomechanical effects. *Rep. Prog. Phys*, 18(184), 2002.

[75] M. Löhndorf, T. Duenas, M. Tewes, E. Quandt, M. Rührig, and J. Wecker. Highly sensitive strain sensors based on magnetic tunneling junctions. *Applied Physics Letters*, 81(2):313–315, 2002.

[76] R M. Bozorth, Elizabeth F. Tilden, and Albert J. Williams. Anisotropy and magnetostriction of some ferrites. *Physical Review - PHYS REV X*, 99:1788–1798, 09 1955. doi: 10.1103/PhysRev.99.1788.

[77] N.H. March, Ph. Lambin, and F. Herman. Cooperative magnetic properties in single- and two-phase 3d metallic alloys relevant to exchange and magnetocrystalline anisotropy. *Journal of Magnetism and Magnetic Materials*, 44(1):1 – 19, 1984.

[78] W. H. Meiklejohn. Exchange anisotropy - a review. *Journal of Applied Physics*, 33 (1325), 1962.

[79] W. H. Meiklejohn and C. P. Bean. New magnetic anisotropy. *Phys. Rev.*, 105(3):904–913, 1957.

[80] R. Meservey and P. M. Tedrow. Spin-polarized electron tunneling. *Phys. Rep.*, 238(4): 173, 1994.

[81] D. Meyners, T. von Hofe, M. Vieth, M. Rührig, S. Schmitt, and E. Quandt. Pressure sensor based on magnetic tunnel junctions. *Journal of Applied Physics*, 105(7), 2009.

[82] T. Miyazaki and N. Tezuka. Giant magnetic tunneling effect in fe/al2o3/fe junction. *Journal of Magnetism and Magnetic Materials*, 139(3):L231 – L234, 1995. ISSN 0304-8853.

[83] J. S. Moodera, Lisa R. Kinder, Terrilyn M. Wong, and R. Meservey. Large magnetoresistance at room temperature in ferromagnetic thin film tunnel junctions. *Phys. Rev. Lett.*, 74:3273–3276, Apr 1995. doi: 10.1103/PhysRevLett.74.3273.

[84] V. B. Naik, H. Meng, R. S. Liu, P. Luo, S. Yap, and G. C. Han. Electric-field tunable magnetic-field-sensor based on cofeb/mgo magnetic tunnel junction. *Applied Physics Letters*, 104(23), 2014.

[85] T. Nakajima, T Takeuchi, I. Yuito, K. Kato, M. Saito, K Abe, T Sasaki, T. Sekiguck, and S. I. Yamaura. Effect of annealing on magnetostrictive properties of fe-co alloy thin films. *Mater. Trans.*, 55:556, 2014.

[86] L Néel. Anisotropie magnetique superficielle et surstructures dorientation. *J. Phys. Radium*, 15(4):225, 1954.

[87] K. Nioshioka, S. Gangopadhyay, H. Fujiwara, and M. Parker. Hysteresis and interaction between the magnetic layers in spin valves. *IEEE Transactions on Magnetics*, 31(5): 3949–3951, 1995.

[88] J Nogués and Ivan K Schuller. Exchange bias. *Journal of Magnetism and Magnetic Materials*, 192(2):203 – 232, 1999.

[89] S. S. P. Parkin. Systematic variation of the strength and oscillation period of indirect magnetic exchange coupling through the 3d, 4d, and 5d transition metals. *Phys. Rev. Lett.*, 67(25):3598–3601, 1991.

[90] S. S. P. Parkin and D. Mauri. Spin engineering: Direct determination of the ruderman-kittel-kasuya-yosida far-field range function in ruthenium. *Physical review. B*, 44(13), 1991.

[91] S. S. P. Parkin, N. More, and K. P. Roche. Oscillations in exchange coupling and magnetoresistance in metallic superlattice structures: Co/ru, co/cr, and fe/cr. *Phys. Rev. Lett.*, 64(19):2304–2307, 1990.

[92] L. G. Parratt. Surface studies of solids by total reflection of x-rays. *Phys. Rev.*, 95(2): 359–369, 1954.

[93] S. V. Pietambaram, J. Janesky, R. W. Dave, J. J. Sun, G. Steiner, and J. M. Slaughter. Exchange coupling control and thermal endurance of synthetic antiferromagnet structures for mram. *IEEE Transactions on Magnetics*, 40(4):2619–2621, 2004.

[94] M. Raju, S. Chaudhary, and D. K. Pandy. Effect of interface on magnetic properties of $co_{20}fe_{60}b_{20}$ in ion-beam sputtered $si/cofeb/mgo$ and $si/mgo/cofeb$ bilayers. *J. Magn. Magn. Mater.*, 332:109, 2013.

[95] C. R. Rarey, J. Stringer, and J. W. Edington. Typical electron microscope investigations. *Trans. A.I.M.E.*, 236(811), 1966.

[96] A. Schreyer, K. Bröhl, J. F. Ankner, C. F. Majkrzak, Th. Zeidler, P. Bödeker, N. Metoki, and H. Zabel. Oscillatory exchange coupling in co/cu(111) superlattices. *Phys. Rev. B*, 47:15334–15337, Jun 1993.

[97] Yongho Seo and Wonho Jhe. Atomic force microscopy and spectroscopy. *Reports on Progress in Physics*, 71(1):016101, dec 2007.

[98] Gagan Sharma, Ajay Gupta, Ranjeeta Gupta, Mukul Gupta, Pooja Gupta, and A K Sinha. Depth selective crystallization study of cofeb film on mgo. *Materials Research Express*, 4(10):106404, 2017.

[99] W. Shen, B. D. Schrag, M. J. Carter, and G. Xiao. Quantitative detection of dna labeled with magnetic nanoparticles using arrays of mgo-based magnetic tunnel junction sensors. *Applied Physics Letters*, 93(3):033903, 2008.

[100] Weifeng Shen, Dipanjan Mazumdar, Xiaojing Zou, Xiaoyong Liu, B. D. Schrag, and Gang Xiao. Effect of film roughness in mgo-based magnetic tunnel junctions. *Applied Physics Letters*, 88(18):182508, 2006. doi: 10.1063/1.2201547.

[101] Howard Siegerman and David Hinson. *The Thin FIlm Book of Basics*. Materials Research Corporation, 5 edition, 1988.

[102] J. C. Slonczewski. Conductance and exchange coupling of two ferromagnets separated by a tunneling barrier. *Phys. Rev. B*, 39(10):6995–7002, 1989.

[103] V. Soti. Tunneling magnetoresistance of feco/mgo/feco magnetic tunnel junctions. *Adv. Studies Theor. Phys*, 5(16):775–781, 2011.

[104] L. Spieß, G. Teichert, R. Schwarzer, H. Behnken, and C. Genzel. *Moderne Röntgenbeugung. Röntgendiffraktometrie für Materialwissenschaftler, Physiker und Chemiker*, volume 2. Vieweg + Teubner, 2009.

[105] Carmen-Gabriela Stefanita. *Magnetism - Basics and Applications*. Springer, 2012.

[106] Christian Sterwerf. *Magnetic compounds for improving spintronic applications*. PhD thesis, University of Bielefeld, Department of Physics, 2016.

[107] M. D. Stiles. *Ultrathin Magnetic Structures III*, volume 1. Springer-Verlag, New York, 2004.

[108] T. Takenaga, Y. Tsuzaki, C. Yoshida, Y. Yamazaki, A. Hatada, M. Nakabayashi, Y. Iba, A. Takahashi, H. Noshiro, K. Tsunoda, M. Aoki, T. Furukawa, H. Fukumoto, and T. Sugii. Magnetic tunnel junctions for magnetic field sensor by using CoFeB sensing layer capped with MgO film. *Journal of Applied Physics*, 115(17), 2014.

[109] Ali Tavassolizadeh. *Miniaturized Tunnel Magnetoresistance Sensors for Novel Applications of Atomic Force Microscopy*. PhD thesis, Christian-Albrechts-Universität zu Kiel, 2015.

[110] Ali Tavassolizadeh, Tobias Meier, Karsten Rott, Günter Reiss, Eckhard Quandt, Hendrik Hölscher, and Dirk Meyners. Self-sensing atomic force microscopy cantilevers based on tunnel magnetoresistance sensors. *Applied Physics Letters*, 102(15), 2013.

[111] Hiroyuki Tomita, Katuaki Konishi, Takayuki Nozaki, Hitoshi Kubota, Akio Fukushima, Kay Yakushiji, Shinji Yuasa, Yoshinobu Nakatani, Teruya Shinjo, Masashi Shiraishi, and Yoshishige Suzuki. Single-shot measurements of spin-transfer switching in CoFeB/MgO/CoFeB magnetic tunnel junctions. *Applied Physics Express*, 1:061303, may 2008.

[112] S. Toscano, B. Briner, H. Hopster, and M Landolt. *J. Magn. Magn. Matter*, 114(L6), 1992.

[113] H. Uchida, Y. Matsumura, and H. Kaneko. Progress in thin films of giant magnetostrictive alloys. *J. Magn. Magn. Mater.*, 239(1-3):540, 2002.

[114] P. J. van der Zaag, Y. Ijiri, J. A. Borchers, L. F. Feiner, R. M. Wolf, J. M. Gaines, R. W. Erwin, and M. A. Verheijen. Difference between blocking and néel temperatures in the exchange biased fe$_3O_4$/CoO system. *Phys. Rev. Lett.*, 84:6102–6105, Jun 2000. doi: 10.1103/PhysRevLett.84.6102.

[115] Anabela Veloso and Paulo P. Freitas. Spin valve sensors with synthetic free and pinned layers. *Journal of Applied Physics*, 87(9):5744–5746, 2000.

[116] E. Villari. Change of magnetization by tension and by electric current. *Ann. Phys.*, 126: 87, 1865.

[117] D. Wang, C. Nordman, J. M. Daughton, Z. Qian, and J. Fink. 70free and reference layers. *IEEE Trans. Magn.*, 40(4):2269, 2004.

[118] Dexin Wang, Cathy Nordman, Zhenghong Qian, James M. Daughton, and John Myers. Magnetostriction effect of amorphous cofeb thin films and application in spin-dependent tunnel junctions. *Journal of Applied Physics*, 97(10C906), 2005.

[119] Qianchang Wang, Xu Li, Cheng-Yen Liang, Anthony Barra, John Domann, Chris Lynch, Abdon Sepulveda, and Greg Carman. Strain-mediated 180° switching in cofeb and terfenol-d nanodots with perpendicular magnetic anisotropy. *Applied Physics Letters*, 110(10):102903, 2017.

[120] Y. Wang, P. M. Levy, and J. L. Fry. Interlayer magnetic coupling in fe/cr multilayered structures. *Phys. Rev. Lett.*, 65(21):2732–2735, 1990.

[121] Zhongchang Wang, Mitsuhiro Saito, Keith P. McKenna, Shunsuke Fukami, Hideo Sato, Shoji Ikeda, Hideo Ohno, and Yuichi Ikuhara. Atomic-scale structure and local chemistry of cofeb–mgo magnetic tunnel junctions. *Nano Letters*, 16(3):1530–1536, 2016.

[122] H. A. Wierenga, W. de Jong, M. W. J. Prins, Th. Rasing, R. Vollmer, A. Kirilyuk, H. Schwabe, and J. Kirschner. Interface magnetism and possible quantum well oscillations in ultrathin co/cu films observed by magnetization induced second harmonic generation. *Phys. Rev. Lett.*, 74:1462–1465, Feb 1995.

[123] D.B. Williams and C.B. Carter. *Transmission electron microscopy*. Springer-Verlag, 2009.

[124] Haiwen Xi and Robert M. White. Theory of the blocking temperature in polycrystalline exchange biased bilayers based on a thermal fluctuation model. *Journal of Applied Physics*, 94(9):5850–5853, 2003.

[125] Haiwen Xi, Robert M. White, Zheng Gao, and Sining Mao. Antiferromagnetic thickness dependence of blocking temperature in exchange coupled polycrystalline ferromagnet/antiferromagnet bilayers. *Journal of Applied Physics*, 92(8):4828–4830, 2002.

[126] S. Yuasa and D. D. Djayaprawira. Giant tunnel magnetoresistance in magnetic tunnel junctions with a crystalline $mgo(001)$ barrier. *J. Phys. D Appl. Phys*, 40(21):R337, 2007.

[127] Shinji Yuasa, Taro Nagahama, Akio Fukushima, Yoshishige Suzuki, and Koji Ando. Giant room-temperature magnetoresistance in single-crystal fe/mgo/fe magnetic tunnel junctions. *Nature Materials*, 3:868 EP –, 10 2004.

[128] Shinji Yuasa, Yoshishige Suzuki, Toshikazu Katayama, and Koji Ando. Characterization of growth and crystallization processes in CoFeB/MgO/CoFeB magnetic tunnel junction structure by reflective high-energy electron diffraction. *Applied Physics Letters*, 87(24):242503, 2005.